SCANNING TUNNELING MICROSCOPY AND SPECTROSCOPY OF TOPOLOGICAL MATERIALS WITH BROKEN SYMMETRY

BY

KANE SCIPIONI

DISSERTATION

Submitted in partial fulfillment of the requirements
for the degree of Doctor of Philosophy in Physics
in the Graduate College of the
University of Illinois at Urbana-Champaign, 2017

Urbana, Illinois

Doctoral Committee:

Professor James Eckstein, Chair
Professor Vidya Madhavan, Director of Research
Associate Professor Taylor Hughes
Assistant Professor Virginia Lorenz

Abstract

This dissertation focuses on the probing of physics governing the electronic and structural properties of topological materials. In three-dimensional topological insulators, the native substitutional defects result in a shift of the chemical potential into the conduction and valence bands. The added conduction channels obscure the physics of the topological surface states. Chemical tuning has been used previously to counteract this parasitic conductivity. However, many details of the process are not well understood and the conditions required to produce optimal samples are not yet well established. In the first project, scanning tunneling spectroscopy was used to observe Landau quantization in thin films of $(Bi_{1-x}Sb_x)_2Te_3$. By combining nanoscale imaging and spectroscopy, the sensitivity of the chemical potential to the chemical composition and thin film growth conditions was studied. The results demonstrate the multi-dimensional parameter space required to obtain an intrinsic topological insulator and provide knowledge to optimize the electronic properties of topological materials. Magnetic doping was then added to induce ferromagnetism, which creates an energy gap in the surface states of $(Bi_{1-x}Sb_x)_2Te_3$. Tunneling conductance spectroscopy was used to examine the correlation between the density of magnetic impurities and the size of the surface band gap. The results indicate that large concentrations of Cr create impurity states inside the gap that reduce the effective gap magnitude. Finally, Landau level spectroscopy was applied to the surface state of $Pb_{1-x}Sn_xSe$ where the signature of electron-phonon coupling was extracted from the surface state dispersion and was used to determine the mass enhancement factor.

Acknowledgments

Although I was the primary researcher on the projects documented in this dissertation, none of it would have been possible without the efforts by others. First, I thank the U.S. Department of Energy, the National Science Foundation, and the United States taxpayers for their continued financial support as well as the Fredrick Seitz Materials Research Laboratory for their facilities and equipment that I used for many of my measurements. There are several individuals that contributed to my success as well. I thank Ilija Zeljkovic and Daniel Walkup for their support and mentorship while I was at Boston College; Ferhat Katmis for his mentorship in thin film growth; Zhenyu Wang for his invaluable aid in performing these experiments; Yulia Maximenko for her contributions to sample characterization and film growth; and many others too numerous to list. I also thank my advisor Vidya Madhavan for giving me the opportunity to work on these projects. Lastly, I thank Caitlin Sawyer for her personal support all the way through.

Table of Contents

List of Tables

List of Figures

List of Abbreviations

AHE	Anomalous Hall Effect
ARPES	Angle-Resolved Photoemission Spectroscopy
BHF	Buffered Hydrofluoric Acid
BST	$(Bi_{1-x}Sb_x)_2Te_3$
BZ	Brillioun Zone
CBST	$Cr_y(Bi_{1-x}Sb_x)_{2-y}Te_3$
DOS	Density of States
FWHM	Full-Width Half Maximum
KDE	Kernel Density Estimation
LDOS	Local Density of States
LEED	Low-Energy Electron Diffraction
LL	Landau Level
MBE	Molecular Beam Epitaxy
MEM	Maximum Entropy Method
MOSFET	Metal Oxide Semiconductor Field Effect Transistor
NEG	Non-Evaporable Getter
PID	Proportional-Integral-Derivative
QAHE	Quantum Anomalous Hall Effect
QCM	Quartz Crystal Microbalance
QHE	Quantum Hall Effect

QL	Quintuple Layer
QSH	Quantum Spin Hall
RHEED	Reflection High-Energy Electron Diffraction
SOC	Spin-Orbit Coupling
STM	Scanning Tunneling Microscopy
STO	$SrTiO_3$
STS	Scanning Tunneling Spectroscopy
TCI	Topological Crystalline Insulator
TI	Topological Insulator
TKNN	Thouless-Kohmoto-Nightingale-den Nijs
TRS	Time Reversal Symmetry
UHV	Ultra-High Vacuum
VDW	van der Waals
XPS	X-Ray Photoemission Spectroscopy
XRD	X-Ray Diffraction
XRR	X-Ray Reflectivity

List of Symbols

m	mass
e	electron charge
E_F	Fermi Energy
k_F	Momentum wave vector where $\mathrm{E}(k_F) = \mathrm{E}_F$
$\Re\{\Sigma\}$	Real Component of Electron Self-Energy
$\Im\{\Sigma\}$	Imaginary Component of Electron Self-Energy
$\alpha^2F(\omega)$	Eliashberg Function
$m(\omega)$	Constraint Function for MEM Routine
$\frac{dI}{dV}$	Differential Tunneling Conductance

Chapter 1

Topological Materials

The discovery and understanding of new phases of matter have been a cornerstone of condensed matter physics for nearly a century, and continuously drive both theory and experiments. Phases of matter are distinguished from one another through symmetry breaking processes and quantified by a discontinuous change in some order parameter. In the liquid-gas phase transition, a well-known example, the density of matter in a thermodynamic system changes abruptly near the phase transition. In this scenario, the relative change in density is an order parameter that distinguishes these phases. In the disordered phase (gas), the relative density difference is zero. In the more highly ordered phase (liquid) it takes on the value of unity. As the system moves toward the phase boundary, the order parameter jumps discontinuously to unity. Identifying and understanding these symmetries and their connection to the order parameter is paramount to the fundamental understanding of a particular phase of matter.

For solid state matter, symmetries can further differentiate phases including those differentiated by structural and electronic order. Examples include lattice parameters (crystal phases) and magnetic susceptibility (superconducting phase). While these phases are focused on structural and electronic order, methods for distinguishing phases using characteristic integer quantities exist as well. Symmetries and interactions can produce band structures with a different topology than, for instance, the vacuum state. A solid phase defined this way is called a topological phase. The first very notable example of a topological phase is in the integer quantum Hall effect (QHE). The theoretical work resulting from the discovery of the QHE has now lead

to the predictions of several different topological classes. Many materials have been classified topologically using a characteristic integer geometric invariant, which is the quantity that distinguishes a topological phase. This chapter describes the initial concept of the topological invariant and the expansion of this idea to the topological insulator, which is the main focus of this work. Following that is a discussion of the current issues facing experiments that probe symmetry broken states in topological insulators.

1.1 Topological Phases

When a system of electrons is subjected to an external magnetic field, the electrons accumulate into degenerate quantum cyclotron orbits [1]. This is known as Landau quantization, and the energy levels are called Landau Levels (LL). When this system of electrons is constricted to a two-dimensional plane, the Hall conductance becomes exactly quantized at low temperatures and high magnetic fields [2]. In their landmark paper, von Klitzing *et al* measured the Hall conductance, σ_{xy}, of the Silicon Metal-Oxide-Semiconductor-Field-Effect Transistor (MOSFET) inversion layer subjected to an 18T magnetic field and determined the Hall conductance to be

$$\sigma_{xy} = -\frac{e^2 i}{h}, (i = 1, 2, 3, ...) \tag{1.1}$$

where e is the electron charge and h is Planck's constant. This occurs when the Fermi level lies in between two Landau levels. The measurement yields a very concise expression for the Hall resistance

$$R_H = \frac{\mu_0 c}{2i\alpha} \tag{1.2}$$

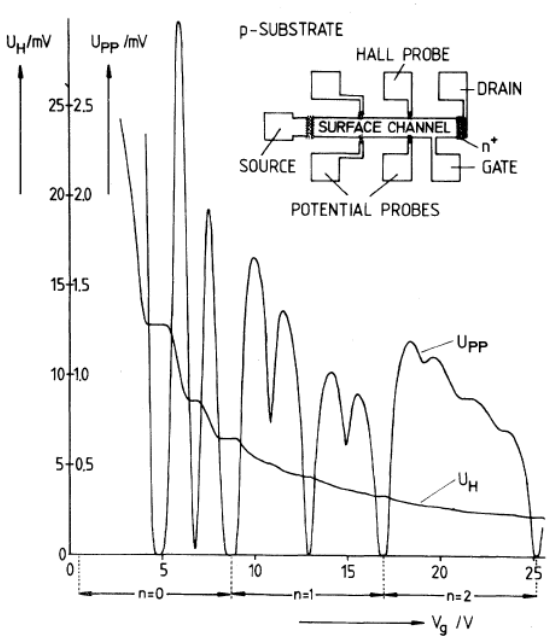

Figure 1.1: **Quantum Hall Effect.** Transverse (U_H) and logitudinal (U_{PP}) Hall voltage as a function of MOSFET gate voltage in a constant 18T magnetic field (von Klitzing *et al*).

where μ_0 is the permeability of space, c is the speed of light, and α is the fine structure constant. Shown in Fig. 1.1 are the results from this experiment. The most profound aspect of the result is the exactness of the conductance plateaus even in the presence of impurities and thermal broadening of the Landau levels.

This theoretical problem was initially addressed by Laughlin, whose argument is based on the constraint of the allowed gauge transformations imposed by periodic boundary conditions of the two dimensional electron gas [3]. For electrons in an extended state, the wave functions must obey $u(r) = u(r + L)$ for boundaries with a periodicity of length L. A gauge transformation of the form

$$\vec{A} \rightarrow \vec{A} + \nabla\Lambda$$

where $\vec{A}$ is the vector potential driving the magnetic field, and Λ is an arbitrary scalar field will affect the wave functions through a phase factor $e^{i\frac{e}{\hbar}\Lambda}$. This obviously can

only take on certain values, namely $e^{2\pi i}$. So, the valid phase factors arise from vector potential increases of the integer multiples of $\frac{hc}{eL}$. Laughlin's argument was that when the Fermi level lies in any gap, and excitation to the next Landau level does not occur, the increase in vector potential increases the total energy by shifting the Landau level states toward the transverse direction relative the applied electric field. Because the states can only be affected by integer multiples of the flux quantum, the shift in states that contributes to the Hall conductance is an integer multiple as well. This is clearly the case for an ideal free electron gas, but Laughlin further argued that, in disordered state, the only difference is that a gap exists between both electrons and holes. Excitations across the gap still cannot occur, and the states are shifted in the same way.

The argument above has the result that each energy elevel contributes a quanta to the Hall conductance. Now suppose a periodic potential is present, which is a likely scenario. The Landau levels will split into a number of subbands which, by similar logic, each contribute a quanta to the Hall conductance. However, the number of subbands can be arbitrarily large. This paradox was addressed in the famous Thouless-Kohmoto-Nightingale-den Nijs (TKNN) paper which explained how the subbands contribute to the Hall conductance [4]. They calculated the Hall conductance using a periodic potential and the Kubo formula for two dimensional conductors. It was found that the contributions to the Hall current from each subband would be given by either a positive or negative integer, $\pm i$, of $\frac{e^2}{h}$. Each integer is determined from the number of subbands, p and the flux quanta per unit cell of the potential, $\phi = p/q$, where q is also an integer (see Ref. [4] Eq. 9). The sum of these contributions, t, gives the Hall conductance

$$\sigma_H = \frac{e^2}{h}(t + N - 1)$$

The set of integers, t, are Chern numbers and thus a topological invariant [5].

The TKNN integers distingush a phase, in much the same way the genus distinguishes the topology of shapes. Naturally, it can be generalized. This realization lead to the idea that the QHE could be realized without Landau levels, and alternatively due to the spin-orbit coupling (SOC) effect in quasi-two dimensional systems [6]. From this, the quantum spin Hall (QSH) effect was theoretically developed, and is described by a $\mathbb{Z}_2$ invariant [7]. Instead of charge displacement occuring at the system's edges, as is the case with the QHE, the spins are displaced. The prediction and observation of the QSH effect in HgTe-CdTe quantum wells came shortly after [8, 9]. It was the first QSH insulator, which also became known as a topological insulator (TI).

1.2 Topological Insulators

The $\mathbb{Z}_2$ invariant, ν, distinguishes a time-reversal symmetry (TRS) protected topological phase. TRS cannot possibly exist with the QHE due to the presence of magnetic fields. In contrast to QHE, the sum of TKNN integers for opposite spin states gives zero quantum Hall conductance. However, the difference is non-zero and determines the spin current toward the system edges. To determine if a system contains a non-trivial band topology, ν must be determined. The original formulation of the $\mathbb{Z}_2$ invariant, by Kane & Mele, was in determining the $\mathbb{Z}_2$ index, I [7]. To describe the QSH phase of Graphene, the TRS constraint was enforced on the Bloch Hamiltonian, $\Theta H(k)\Theta^{-1} = H(k)$, where Θ is the time reversal operator. With the eigenstates, $|u(k)\rangle$, they then showed that the number of complex zeros of the Pfaffian of the overlap matrix, $w_{ij} = \langle u_i(k)|\Theta|u_j(k)\rangle$, indicates the $\mathbb{Z}_2$ invariant. Specifically, this is calculated by the contour integral

$$I = \frac{1}{2\pi\imath} \oint_C dk \nabla \log[\mathrm{Pf}[w_{ij}] + \imath\delta] \tag{1.3}$$

where C is the contour enclosing half of the Brillouin zone. For normal insulator states, I is even, and odd I corresponds to the QSH state. The invariant is given by $\nu = I \pmod 2 \in \{0, 1\}$, hence $\mathbb{Z}_2$. In addition to TRS, the SOC must be large enough to invert the bulk band gap. The states become topologically different from the vacuum state and results in $\nu = 1$. When the Graphene plane cuts off at the edges, the state above the gap must be reconnected across the Fermi level in much the same way the edge states in the QHE behave. These band crossings result in a degenerate state called the Dirac point. This degeneracy is protected by the TRS, and is the most profound observable effect of the band structure topology.

The $\mathbb{Z}_2$ formulation was then extended to describe the analogous topological phase for three dimensional systems, which categorized them into two types, weak topological insulators (WTI) and strong topological insulators (STI) [10]. Crystals with inversion symmetry can simplify the calculation of the $\mathbb{Z}_2$ invariant [11]. By using this simplification, it was predicted that $Bi_{1-x}Sb_x$ and Bi_2Te_3 are STIs. In the case of the 3D TIs, the edge states are now surface states. The inverted bulk bands must cross at the boundary with an uninverted band. The strikingly unique property of these surface states is the linear energy-momentum dispersion, which mimics the Dirac dispersion of a massless particle. Near the point of the band crossing at $\vec{k} = 0$, the Γ point in reciprocal lattice space, the dispersion is isotropic. These bands contain spin-split states. This is caused by the Rashba effect at the surface interface. The spins of each electron become locked in-plane at a right angle to the wave vector $\vec{k}$. This chirality of the spins in momentum space is called spin-momentum locking. Because the spin is now dependent on the electron's direction of propagation, it is possible to study and control natively spin-polarized currents. Furthermore, a direct back-scattering event is denied by Pauli exclusion, unless a spin rotating mechanism is also present. Other scattering channels are possible with their respective probabilities; however the scattering is generally reduced. An illustration of the 3D TI

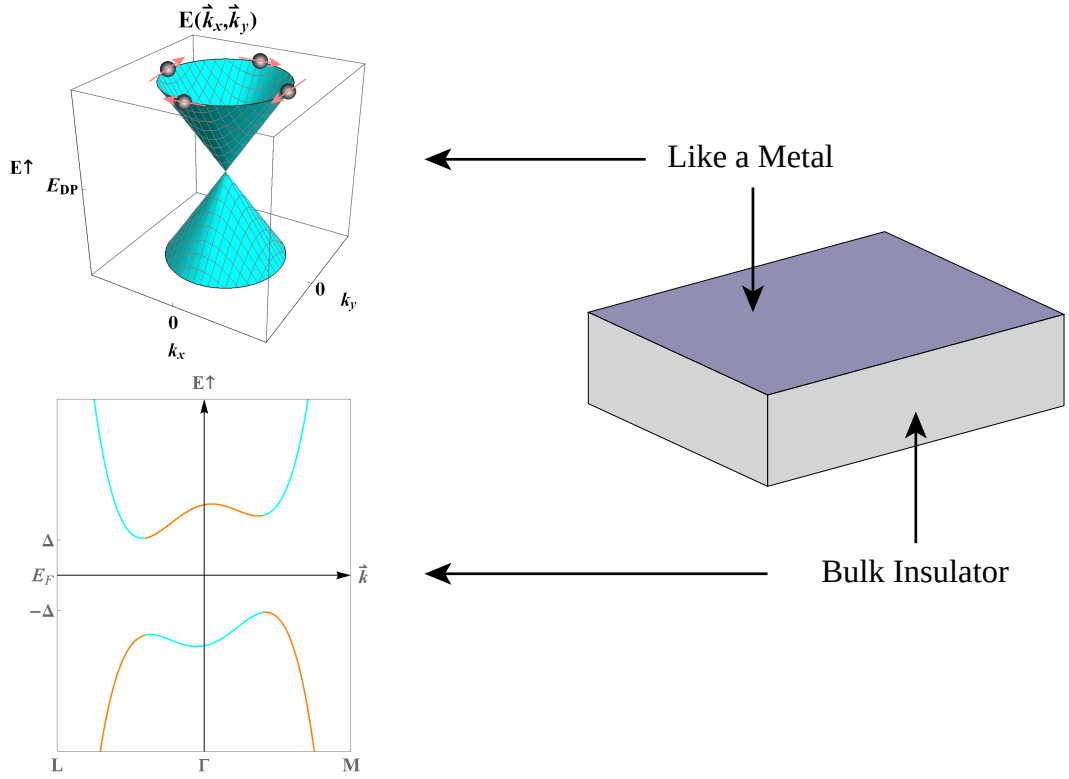

Figure 1.2: **Basic Properties of 3D Topological Insulators.** 3D TIs possess insulating bulk properties like that of a narrow band gap semiconductor. The surfaces are metal like in that they have energy bands crossing the Fermi level.

properties is shown in Fig. 1.2, qualitatively describing the bands in the bulk and at the surface.

The focus in the experiments described later will be on these 3D TIs, and the symmetry breaking proccesses that lead to more novel phases. This class of materials has rapidly expanded the application of band topology to include other symmetries, such as point group symmetry, which is discussed in Chap. 6. The surface states of the most prevalent 3D TIs, Bi_2Se_3 and Bi_2Te_3, have been experimentally observed by both angle-resolved photoemission spectroscopy (ARPES) and scanning tunneling microscopy (STM) [12, 13, 14, 15, 16, 17, 18]. This has generated much interest in finding new topological phases and device characteristics that capitalize on the unique properties of the surface state. These properties have obvious benefits for

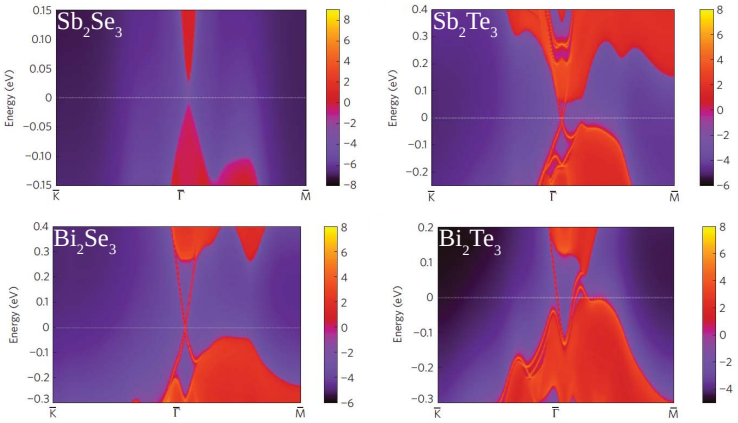

Figure 1.3: **First-Principles Band Structures of $(Bi,Sb)_2(Se,Te)_3$.** Calculation of the band structure for Sb_2Se_3, Sb_2Te_3, Bi_2Se_3, and Sb_2Se_3 (Zhang *et al*).

the realization of devices such as the spin-field effect transistor (spin-FET) and a topological transistor. However, the physics becomes much richer when we consider the system with symmetry breaking perturbations and the states that arise from these perturbations including, but not limited to, the quantum anomalous Hall effect (QAHE).

1.3 Properties of the $(Bi,Sb)_2(Se,Te)_3$ System

It turns out that several group V-VI binary compounds and their various alloys are TIs, including the ubiquitous parent compounds Bi_2Se_3 and Bi_2Te_3 as well as Sb_2Te_3. Sb_2Se_3 is not a topological insulator as this pattern suggests. First-principles calculations, Fig. 1.3, have been performed to show the existence of the surface states [19]. Experimental evidence showed that $Bi_{1-x}Sb_x$ is a STI [20]. However, the difficulty of synthesizing this alloy correctly and the complexity of its band structure changed focus to other heavy Bi/Sb based materials like Bi_2Te_3. The experimental observations of Bi_2Se_3 and Bi_2Te_3 indicate the existence of the single Dirac dispersions, or "Dirac cones", centered at the Γ point of the electronic Brillioun zone (BZ) [12, 13]. While these ARPES studies confirmed the surface state of these materials, STM was

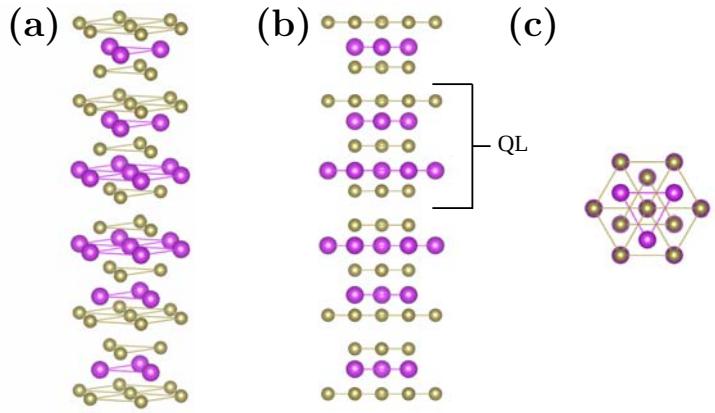

Figure 1.4: **Crystal structure of $(Bi,Sb)_2(Se,Te)_3$.** (a) isometric view. (b) a-plane $\langle 11\bar{2}0\rangle$ view. (c) c-plane $\langle 0001\rangle$ view.

employed to observe other properties such as the predicted reduced back-scattering. The fact that the spin-momentum locked states are very robust against impurities is one of the most sought after properties in these materials. What follows from this is the possibly of near-dissipationless spin and charge transport.

These materials are also very good thermo-electric generators, and technological applications already exist to leverage these properties. Therefore, crystal growth methods including thin film techniques, like molecular beam epitaxy, have already been developed. The amount of research in these materials makes them one of the most widely used platforms for more complex experiments on the TI surface state. Since it one of the main systems of focus here, we will review some of these fundamental properties and significant experiments as they will be referred to repeatedly.

The crystal structure of Bi_2Te_3 and its siblings fall in the space group of $R\bar{3}m$. Its unit cell can be represented in both rhombohedral or hexagonal unit cells. The atom basis consists of five atoms in rhombohedral units, however the crystal structure in experimental setups is easily visualized in hexagonal units (see Fig. 1.4). In the view of the a-plane, Fig. 1.4(b), there is a pattern of repeated planes within the unit cell along the c-axis. These are stacks of five atomic planes are called quintuple layers

M_2X_3	a (Å)	c (Å)
Bi_2Se_3	4.13	28.64
Bi_2Te_3	4.38	30.48
Sb_2Te_3	4.25	30.35

Table 1.1: **3D TI Lattice Parameters.** The hexagonal lattice parameters for the V-VI topological insulators.

(QL). The bonding mechanism between neighboring QLs is a weak van der Waals bonding, where the planes within a QL are covalently bonded. From an experimental perspective, this is advantageous for techniques requiring an ultra clean surface in vacuum, like ARPES and STM. In these experiments, mechanical *in situ* cleaving of a single bulk crystals is done to achieve this. The weakly bonded layers separate easily, and produces high quality surfaces with few defects. Because the inter-QL gap is the lowest energy, the cleaving exclusively occurs at the boundary between QLs. This is will always produce a Te/Se terminated surface.

It is also convenient that the lattice parameters of these materials are all within 6% of each other (see Table 1.1). Solid solutions, or alloys, of these compounds have been useful for many reasons including the tuning of thermo-electric properties, carrier concentration, and lattice parameters. Because the crystal structures and bonding are the same, Vegard's Law should hold and high quality crystals should be easily produced for any mixture of $(Bi,Sb)_2(Se,Te)_3$. In the following sections, it is made very clear the profound advantages of using a solid mixture of TI materials for designing band structures and tuning the level of free carriers.

1.4 Symmetry Breaking and the Quantum Anomalous Hall Effect

Matter can transistion to a different phase through a symmetry breaking process. TIs are in a phase where electronic states are protected by TRS. Therefore, breaking TRS will perturb the system in a way that lifts the degeneracy at the Dirac point. Several new phenomena are predicted to arise from different symmetry breaking methods such as an external magnetic field, magnetic doping, and proximity superconductivity [21]. Magnetic doping is an easy and straight forward way of breaking TRS. Breaking The resulting internal magnetism produces a gap where the Fermi surface lies within everywhere.

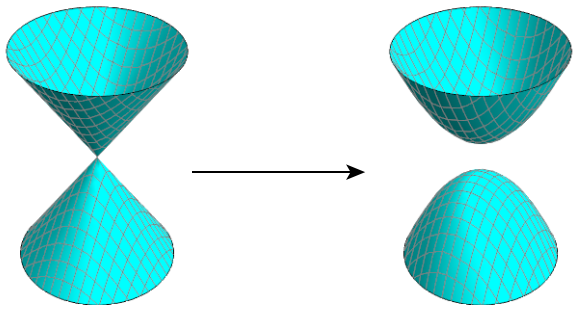

Figure 1.5: **Massive Dirac Gap.** A cartoon showing how TRS breaking lifts the degeneracy at the Dirac point.

Before discussing what occurs when this happens, it is noteworthy that quantized versions of the Hall effect and spin Hall effect have been realized. Intuitively, this should extend to the anomalous Hall effect (AHE) as well. In fact, this is the case, and the highly sought after quantum analog to AHE was recently predicted to be realized in magnetic 3D TIs [22]. With the appropriate doping of Chromium, an exactly quantized Hall conductance in zero magnetic field was measured in very thin films of $Cr_y(Bi_{1-x}Sb_x)_{2-y}Te_3$ at temperatures less than 1K [23]. This is an experimental feat,

but the temperature requirement and difficulty of reproduction is a huge barrier to taking advantage of this quantum anomalous Hall effect (QAHE).

The QAHE is analogous to AHE in that the Hall conductance is determined by the intrinsic magnetization and not an external field or the field produced by the magnetic moment [24]. Therefore, magnetic impurity doping is the key factor in producing the state. Unfortunately, the most notable QSH insulator, HgTe, does not become ferromagnetic from doping [25]. However, the prediction that thin film 3D TIs can exhibit QAHE on magnetic doping lead to the success of Chang *et al* [22, 23]. The Bi/Sb Chalcogendies are known to be ferromagnetic on doping of several transition metals (Fe, V, Cr, Mn) [26]. These transition metals have oxidation states of +3, the same as Bi and Sb. So, the doping should be charge neutral, and thus not populating the crystal with free carriers. For Bi_2Te_3 and Sb_2Te_3, ferromagnetic ordering has been found for Mn, Fe and Cr doping [27, 28, 29].

To date, a few groups have observed the QAHE in $Cr_y(Bi_{1-x}Sb_x)_{2-y}Te_3$ [23, 30]. The two common explanations for the difficulty of the measurement are the population of bulk carriers and possibly magnetic inhomogeneity. Yet, only macroscopic studies have been done to probe this. This immediately suggests the need for a microscopic study of these films to elucidate the effects of local defects, chemical composition, and band structure. With a combination of high precision molecular beam epitaxy and scanning tunneling microscopy, we can acquire this information that Hall measurements and photo-emission techniques cannot.

1.5 Current Experimental Problems

The first issue is this presistant problem with the 3D TIs where their natural tendency to defects increases the bulk carrier concentration. This acts as an electrical short of the surface states, adding conductivity to the material, and causes difficulty in

measuring the QAHE. Making a thin film thinner reduces the overall bulk carriers, but it cannot be made purely 2D because a hybridization gap will occur from coupling of the two surfaces. The other option mentioned previously is through compositional tuning. This works well with n-type Bi_2Te_3 and p-type Sb_2Te_3, but is not suitable for Bi_2Se_3 because Sb_2Se_3 is not a topological insulator. $(Bi_{1-x}Sb_x)_2Te_3$ was found to be a ferromagnetic topological insulator, and the Dirac point is gapped out as should occur from the TRS breaking [29]. For isolation of the surface state, thin films are required not only for reduction of carriers but also for effective gating. Electrical back-gating typically requires a film substrate with a high dielectric constant in which some cases may not be suitable for high quality growth. In that case, a top layer of dielectric material would be deposited on the film.

Dispite the amount of publications on this topic, it is interesting that the issue of bulk conductivity and magnetic disorder remain problematic. The bulk conductivity should have been compensated for when using $(Bi_{1-x}Sb_x)_2Te_3$ because previous studies indicate that intrinsic TI films can be obtained. Back-gating the film with a dielectric substrate should also be able to correct for a small offset in the chemical potential. One apparent inconsistancy in the literature, related to the chemical tuning of $(Bi_{1-x}Sb_x)_2Te_3$, is the "optimal" composition yielding the lowest bulk carrier concentration. Different studies determine a different composition fraction, x, and the variance of these values is left unexplained. In regards to the magnetic inhomogeneity, only a couple of nanoscale studies have been done. These were STM measurements on $Cr_y(Bi_{1-x}Sb_x)_{2-y}Te_3$ and $Cr_ySb_{2-y}Te_3$ [31, 32]. Both were bulk crystals, which are prepared in significantly different conditions from thin films.

The experiments in the following chapters address these issues by identifying factors that contribute to both the chemical potential and magnetic inhomogeneity in TI alloys, specifically in thin films. Isolating the surface states is the key objective in the use of thin films. Since their preparation procedure is drastically different from

bulk single crystals, nanoscale experiments are likely to show a different picture. $(Bi_{1-x}Sb_x)_2Te_3$ films have been studied, but there exists a parameter space of growth conditions beyond the chemical composition that affects the electronic properties. For $Cr_y(Bi_{1-x}Sb_x)_{2-y}Te_3$, the Cr doping adds another layer of complexity. In fact, the compound is very difficult to grow with a high enough quality for surface sensitive techniques such as STM. Not only was high quality growth of $Cr_y(Bi_{1-x}Sb_x)_{2-y}Te_3$ accomplished here, but correlations between massive Dirac gap and the Cr impurities revealed the existence of states in the band gap that are likely contributing to the sample conductivity. This effect may also degrade the ferromagnetic order.

The remaining chapters are organized as follows. Chaps. 2 and 3 are a detailed description of the experimental techniques employed to perform STM measurements on TI thin films. The first topic is the film deposition technique called molecular beam epitaxy. This discussion also includes the supporting experimental techniques used to characterize the samples to optimize the film growth conditions. Chap. 3 discusses scanning tunneling microscopy and its modes of operation. Chaps. 4 and 5 document the experiments involving $(Bi_{1-x}Sb_x)_2Te_3$ chemical tuning and the $Cr_y(Bi_{1-x}Sb_x)_{2-y}Te_3$ magnetic inhomogeneity. The final chapter focuses on a study where the techniques used to study TI materials are employed to measure the electron-phonon coupling in $Pb_{1-x}Sn_xSe$, which is in a class of materials that have their own unique surface bands similar to the conventional TIs.

Chapter 2

Experimental Techniques: Molecular Beam Epitaxy

To obtain ultra-high quality thin films of V-VI topological insulators, such as Bi_2Te_3 and Sb_2Te_3, a vacuum deposition technique known as molecular beam epitaxy (MBE) is used. MBE is similar to more standard physical vapor deposition techniques inasmuch as the elemental source materials are thermally evaporated from ceramic crucibles. However, the distinction of MBE from other techniques lies in a few requirements, namely, very low deposition rates, precise flux control, ultra-high vacuum (UHV) pressures, use of reflection high-energy electron diffraction (RHEED), and the high quality of substrates used to seed epitaxial growth of films. Great attention must be paid to each and every one of these defining aspects to insure the quality of the films is at a level such that only a few nanometers can be grown with a very low defect and impurity density.

The basic procedure in accomplishing successful MBE growth involves both the aspects of the deposition process and the leveraging of characterization techniques. These are both covered in this chapter, which starts with the physics of the MBE vacuum deposition process and then covers the *in situ* and *ex situ* material characterization techniques.

2.1 Thin Film Growth

2.1.1 Effusion

The growth of thin films is fundamentally dependent on the evaporation of elements or compounds in a vacuum environment and subsenquent absorption to a substrate. The first step is governed by the effusion process, which was well described by Hertz, Knudsen, and Langmuir in the past [33]. Initially, Hertz measured the evaporation rate of liquid mercury in an evacuated environment and determined that liquids have a maximum theoretically evaporation rate given by

$$\mathcal{M} = \frac{p(T)}{\sqrt{2\pi RT}} \tag{2.1}$$

where $\mathcal{M}$ is the mass rate of evaporation per unit area, $p(T)$ is the saturated pressure at temperature T, and R is the specific gas constant [34]. However, his measurements yielded significantly lower rates than than expected from Eq. 2.1. Knudsen later performed the same measurement and considered a pressure factor, α, associated with gas particles which collide with the Mercury surface but don't recondense [35]. The effect of those particles is a contribution to the vapor pressure but not to the net evaporation flux [33]. This factor was also found to be dependent on the impurity concentration of the Mercury surface [35]. With this consideration, he was able to measure a nearly theoretical maximum rate when carefully distilling and measuring pure Mercury surfaces. The result of this is the relation

$$\mathcal{M} = \frac{\alpha p(T)}{\sqrt{2\pi RT}} \tag{2.2}$$

which is known as the Hertz-Knudsen equation. Simultaneuous to Knudsen's experiments, Eq. 2.2 was demonstrated to apply also to heated solid surfaces; specifically

current carrying filaments [36]. Knudsen though had previously developed a design for producing vapor pressure for both solids and liquids [37]. His design comprises of a heated isothermal container where the vapor of the source material is in equilibrium with its condensed phase. A small hole penetrates the side of the container allowing for gas to effuse from it in a way consistent with kinetic gas theory and also eliminating the back pressure which α accounts for. This device is called a Knudsen cell, or K-cell. Its operating principle is the basis for nearly all evaporation sources currently used in MBE. The resulting evaporation rate from the effusion point of an ideal K-cell is

$$\mathcal{M} = \frac{p(T) - p_{vac}}{\sqrt{2\pi RT}} \tag{2.3}$$

where p_{vac} is the pressure of the system outside of the cell. The calculation of the angular spread of the molecular flux from an ideal K-cell resulted in the well known cosine law of effusion [38]. Shown in Fig. 2.1(a) is the geometry of a K-cell with a finite size opening for the effusing gas. Considering this scenario and following steps similar to Ref. [33], one can calculated the infinitesimal flux distribution as a function of θ. The first constraint is that the total integrated flux must equal the mass rate given by Eq. 2.3. Expressed as number of total mass per unit time, this is

$$F_o = A\mathcal{M} = \frac{A(p(T) - p_{vac})}{\sqrt{2\pi RT}} \tag{2.4}$$

where A is the area of the opening in the K-cell. Now the flux distribution can be built from this. Assuming a Boltzmann velocity distribution for the vapor in the K-cell, the probability, ρ, of a particle exiting between θ and $\theta + d\theta$ is the ratio of the solid angle $d\Omega = \sin\theta d\theta d\phi = r^2 dS$ to the total solid angle of the hemispherical range, 2π. Integrating over ϕ is trivial given the symmetry. This yields

$$\rho = \frac{d\Omega}{2\pi} = \sin\theta d\theta \tag{2.5}$$

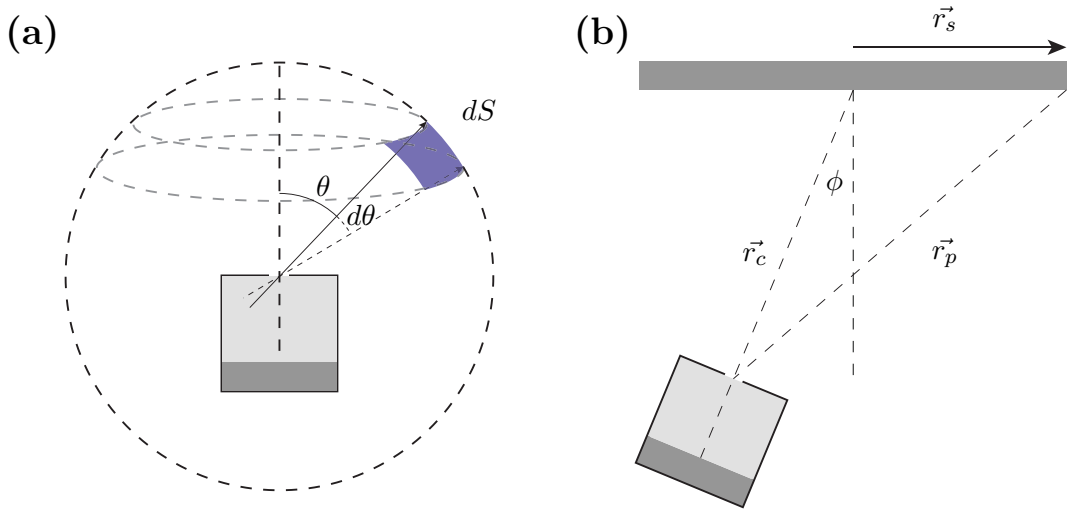

Figure 2.1: **Ideal Knudsen Cell.** (a) Geometry of an ideal K-cell and the unit surface area seen by the cell opening. (b) Geometry of a tilting K-cell with respect to a substrate surface.

Now at angle θ, the total rate seen is suppressed because the projected K-cell opening area decreases like $\cos\theta$. The flux distribution dF scales like the product of $\cos\theta$ with the probability, ρ. Integrating this over the entire hemisphere must equal the total flux, F_o. This determines the proportionality constant, K. Eqs. 2.6 - 2.8 show the result.

$$dF = K\cos\theta\sin\theta d\theta \tag{2.6}$$

$$\int_0^{\frac{1}{2}\pi} dF = \int_0^{\frac{1}{2}\pi} K\cos\theta\sin\theta d\theta \tag{2.7}$$

$$F_o = -K\frac{1}{2}[\cos^2\frac{\pi}{2} - \cos^2 0]$$

$$F_o = \frac{K}{2}$$

$$\Downarrow$$

$$dF = 2F_0\cos\theta\sin\theta d\theta \tag{2.8}$$

With Eq. 2.8, we are poised to generalize this to the flux of a system with a geometry

likely used in a real MBE system (see Fig. 2.1(b)). The insight from this is the initial step in the design process of an MBE system. In general, the K-cell is tilted with respect to the substrate normal vector and directed at its center. The K-cells must be tilted because multiple sources cannot simultaneously be physically directed toward the substrate at normal incidence. Therefore, the MBE system must be designed carefully to create an approximately uniform flux impinging on the substrate. To ensure this, the flux should be calculated as a function of radial distance along the substrate surface. A general solution to the mass flux on a circular substrate is difficult to calculate, however the scaling as function of tilt angle, ϕ, and position, r_s, can be obtained with relative ease. First, consider the case where $\phi = 0$. The flux density is $\frac{dF}{dS}$, where dS is the differential surface area at r and θ. Obviously, $dS = r^2 d\Omega = 2\pi r^2 \sin\theta d\theta$. Therefore, the mass flux at r and θ is

$$\frac{dF}{dS} = \frac{F_o \cos\theta}{\pi r^2} \tag{2.9}$$

For $r = r_c$ (so $\theta = 0$), it simplifies to

$$\frac{dF}{dS} = \frac{F_o}{\pi r_c^2} \tag{2.10}$$

For the edge of the substrate ($r = r_p$), we can use the relations $r_c = r_p \cos\theta$ and $dS_p = dS_c \cos\theta$. Then Eq. 2.9, becomes

$$\frac{dF}{dS} = \frac{F_o \cos^2\theta}{\pi r_p^2} \frac{\cos^2 r_p^2}{r_c^2} = \frac{F_o \cos^4\theta}{\pi r_c^2} \tag{2.11}$$

Because this flux is quartic in $\cos\theta$, the flux density falls off rapidly as function of distance from the substrate center. Since $r_c = r_p \cos\theta$, the substrate size can be accommodated by increasing r_c. If we include the correction for the tilt angle, ϕ, Eqs. 2.10 and 2.11 become significantly more complex. In Appendix A, it is shown that a

large enough value for $\frac{r_c}{r_p}$ well produce an approximately uniform flux with a tilt angle of $\frac{\pi}{6}$, or 30°. For example, the relative decrease in flux density from the center of the substrate to the edge for $r_c/r_s = 20$ is about 7%, which is considerably good. These dimensions are the first design consideration in building an MBE system as well as the properties of Eq. 2.3 (i.e. p_{vac}, A, etc.). UHV environments are mandatory not only to maintain a desire flux but also to reduce the impurity concentration arising from the incorporation of other molecules in the film growth.

The analysis in this section considered only an ideal K-cell. Real effusion sources have a different geometry, namely they long cylindrical crucibles with an opening approximately equal to the cylinder diameter. Real crucibles do in fact have important correction factors, but the the qualitative results and uniformity estimates should be a reasonable guide for practical application.

2.1.2 Measuring Effusion Flux

Given a nearly uniformly generated effusion flux, the next important step is to measure the impinging flux of each effusion source per unit surface area of the substrate. The most common way of doing this is by employing a quartz crystal microbalance (QCM). Quartz is a piezoelectric material, which responds mechanically to external fields. Due to the acoustic wave properties of quartz, a sinusoidal driving voltage can excite resonance vibration modes if the driving voltage is similar in frequency to one of the modes. When a high quality single crystal is cut along an appropriate crystallographic axis, certain modes become pronounced while others are suppressed. This makes quartz ideal for frequency-based measurements because the vibrational modes are dependent on internal and external physical properties. Specifically, the mass of the resonator contributes to determining the resonant frequency. The most common crystallographic cut is the AT-cut quartz, which is designed for use of the thickness-shear mode. Changes in the resonator mass inherently result in a change

in resonant frequency. This is the fundamental operating principle of the QCM.

In the past, the relationship between deposited solid mass on an AT-cut Quartz surface and the resonant frequency was approximated as linear. However, this is only accurate to 2% change in frequency. Further improvements were made which accounted for the shear modulus of the deposited film [39]. This relation translates to a thickness calculation by the formula

$$t = \frac{C\rho_q}{\pi\rho_f Z f_{loaded}} \arctan\left[Z \tan\left[\frac{\pi(f - f_{loaded})}{f}\right]\right] \tag{2.12}$$

where t is the thickness, C is the quartz resonance constant, ρ_f is the density of the film, ρ_q is the density of quartz, f is the original frequency of the sensor crystal, and f_{loaded} is the frequency of the sensor crystal after deposition [40]. The factor Z is given by

$$Z = \sqrt{\frac{\rho_q G_q}{\frac{\rho_f}{G_f}}} \tag{2.13}$$

where G_q is the shear modulus of quartz and G_f is the shear modulus of the film material.

In practice, two other considerations come into play. First is the temperature dependence of the resonator frequency. This can have detrimental effects on precise measurements, especially in a MBE system where effusion sources produce excess radiant heat. To maintain a constant temperature in all environments water cooling is provided to the QCM. The second practical consideration is the tooling factor and atomic packing ratios. The tooling factor is a ratio that converts the measurement at the location of the QCM to the accumulated thickness on the film's substrate. This ratio is determined by depositing a film and measuring its thickness *ex situ* by profilometry or some other method. After this procedure, the tooling is calculated

by

$$\text{Tooling} = 100\% \times \frac{t_{substrate}}{t_{QCM}} \tag{2.14}$$

where $t_{substrate}$ is the thickness on the substrate and t_{QCM} is the thickness on the sensor surface [40]. The atomic packing ratios are also important because the MBE growth is dependent on the molecular ratios (see next section). Therefore, naïvely assuming the ratios from the QCM monitor rates will lead to errors. The ratios must be compensated for by the molar mass and densities of the source elements.

Commercial QCM and driving electronics make implementing the above aspects simple. The frequency of the crystal is measured with very high accuracy. Therefore, Sub-Ångstrom rates can be measured, which is necessary for low temperature depositions because the adatoms are less mobile and require lower deposition rates. Our MBE system implements as retractable QCM sensor, which moves into the location of the film deposition and measures the flux. This eliminates the need for *ex situ* measurements to calculate the tooling because the tooling should be near unity at this point. Nonetheless, it is important to be able to monitor the overall rate during growth when the QCM is retracted and the tooling should be known.

2.1.3 Growth Physics

Once the effusion is generated and set to the desired rates, the crystal substrate is subjected to the desired impinging molecular fluxes. The conditions for growth are now determined by a few factors, namely, absorption/desorption processes, substrate crystal structure, and the substrate temperature.

When the molecules of the impinging flux beam reach the surface of the substrate they participate in two types of absorption processes, physisorption and chemisorption. During the the physisorption process, molecules stick due to the attractive van der Waals (VDW) interaction between the substrate atoms and the molecule's

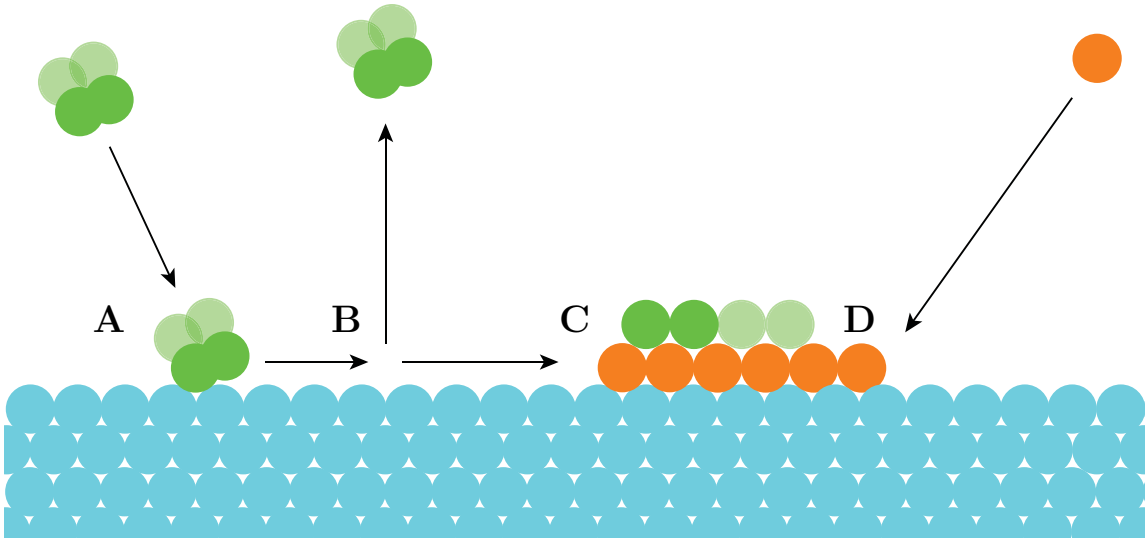

Figure 2.2: **Growth Process.** **A** Te_2/Te_4 (green) can physisorb to substrate (blue). **B** If Te_2/Te_4 reaches its lifetime before finding 2 or 4 Bi (orange) it re-evaporates. **C** Dissociation of Te_2/Te_4 and chemisoprtion on Bi layer. **D** Bi chemisorbs with a probability of nearly unity.

atoms. The VDW attraction is weak, and the molecules maintain their chemical identity [33, 41]. They are easily desorbed as a consequence. The desorption rate, or surface diffusion lifetime, is dependent on the substrate temperature. In contrast, the chemisorption process is much stronger, and involves the chemical bonding of the molecule with the substrate surface atoms. Initially, the molecule will stick to the substrate surface in a way similar to physisorption and diffuse over the surface. Given a long enough lifetime on the surface, the molecule will dissociate and the atoms will chemically bond to the surface [41]. Both processes contribute to growth of the initial monolayer and additional layers of the film [33].

Much work has been done to understand how these processes contribute to the growth of thin films, and particularly for GaAs. The growth of GaAs thin films is done by first evaporating Ga and As from their respective effusion cells. While Ga evaporates as an atomic gas, As will evaporate as As_2 and As_4 molecules. These molecules can stick to the substrate by physisorption. Depending on the substrate, a molecule will often not chemically bond at the temperatures used for the growth. However, it

will likely bond to a monolayer of Ga. The growth of GaAs is a prototypical example, and is of general significance as a basic procedure for binary compounds.

Bi_2Te_3 grows similarly. The Te source evaporates as mostly Te_2/Te_4 resulting in a reduced surface diffusion lifetime. On the other hand, Bi should be sticking to the substrate with a probability of nearly unity. The Bi layer creates a surface chemistry where it is energetically favored for Te_2/Te_4 to dissociate and bond to the layer. The process is then repeated. An illustration of this is shown in Fig. 2.2. Typical substrate temperatures used are around 200-300 °C and can grow with high quality on Al_2O_3, $SrTiO_3$, or Si. The flux ratios are typically Te:Bi=10 or higher. This is a similar over-pressure technique used in GaAs growth. If this procedure is extended to Sb_2Te_3, high quality growth is more difficult to achieve, especially at higher temperatures. The Sb effusion flux is dominated by Sb_2/Sb_4, similar to Se and Te. Bi and Sb are the species that seed and continue the film's growth. Therefore, the Sb molecules must dissociate in order to produce the surface energy conditions to bond with the substrate and allow Te_2/Te_4 to chemisorb.

A couple of techniques exist to improve the growth process for Sb based compounds. One way is to use a special K-cell design called a "cracker", which can break Sb_2/Sb_4 at the K-cell orifice. Another way is to use much lower substrate temperatures. However, this can cause poor crystallinity. Two-step growth has been previously used for the $(Bi_{1-x}Sb_x)_2Te_3$ alloy as well as molecular Sb_2Te_3 evaporation [42]. Each technique has it advantages and disadvantages. Cracker effusion sources are extremely expensive and because of this are not used in the custom MBE system used here. Regardless, it is possible to obtain high quality thin films of these materials given the appropriate thermodynamic conditions.

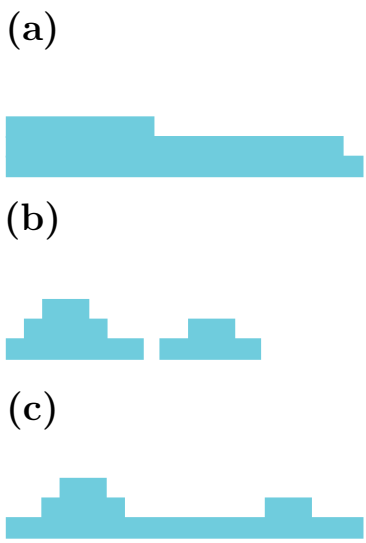

Figure 2.3: **Growth Modes.** (a) Frank-van der Merwe. (b) Volmer-Weber. (c) Stranski-Krastanov.

2.1.4 Growth Modes

Another important aspect of MBE growth is how the film accumulates on the surface. This is dependant on the bonding between the source elements and the substrate as well as the bonding of the compound comprising the film. The three basic types of the growth modes, Fig. 2.3, that characterize film growth patterns in MBE are called the Frank-van der Merwe, Volmer-Weber, and Stranski-Krastanov modes [43]. In Frank-van der Merwe growth (or layer-by-layer), the atoms in the molecular beam stick to the substrate and have a higher bond strength with the substrate than with each other, whereas in Volmer-Weber (or island) growth, the bond strength between the atoms is stronger than with the substrate [41]. In Stranski-Krastanov growth, layer-by-layer is accompanied by island growth on top of the layers.

The growth mode of the film is determined by a couple of factors. The requirement for layer-by-layer growth is that a full monolayer of atoms can reduce the surface energy of the substrate energy and subsequently the surface energy of the next layer. A common thermodynamic explanation is to consider the surface free energies of the

film, substrate, and interface, γ_f, γ_s, and $\gamma*$. The inequality

$$\gamma_f + \gamma* \leq \gamma_s \tag{2.15}$$

states the condition to obtain layer-by-layer growth [44]. 3D island formation occurs otherwise. The Stranski-Krastanov mode develops because the interface free energy, $\gamma*$, increases as a function of monolayers [41].

For Bi_2Te_3 and Sb_2Te_3, layer-by-layer and Stranski-Krastanov type growth modes can be obtained depending on the substrate and growth conditions. For the experiments here, layer-by-layer growth is desired because it replicates an ideal quasi-two-dimensional system that hosts phenomena like the QAHE. Layer-by-layer growth also produces better samples for STM measurements because the terrace sizes are large. However, the substrate miscut is another practical hurdle. The miscut produces "step-flow" growth where molecules diffusing on the substrate surface are limited by terraces. The resulting film will have steps even if layer-by-layer growth is achieved. More often than not Stranski-Krastanov growth is achieved, and the topmost islands are usually limited to only a couple of layers giving an overall high quality flat film.

2.2 Sample Characterization

An MBE grown thin film is useless without knowing several properties including composition, crystal structure, and morphology of the final product. *in situ* and *ex situ* characterization techniques are mandatory to utilize the precision of MBE. The nature of the growth process makes monitoring the environment at the substrate surface nearly impossible. Even measurements as simple as the substrate temperature have calibration offsets because contact measurements are obviously not feasible. The inability to make mechanical contact to the substrate during growth limits real-time

measurements to electron diffraction, QCM, and mass spectroscopy techniques. Reflection high energy electron diffraction (RHEED) is the workhorse during growth, and a tremendous amount of information can be obtained from this technique. However, most of the characterization measurements must be performed *ex situ*, like X-ray diffraction and X-ray photo-emission spectroscopy. The techniques described in this will be only those that are utilized for the experiments in Chaps. 4 and 5, beginning with X-ray diffraction.

2.2.1 X-ray Diffraction

Diffraction phenomena has been ubiquitous in experimental solid state physics starting with the discovery of X-ray diffraction (XRD), which is the result of interfering X-rays after scattering in a 3D periodic structure of crystalline material. The wave length of the light determines the separation of scattering centers which produce a significant interference effect. X-rays, which have a wavelength on the order of Ångstroms, produce diffraction patterns resulting from the multiple scattering associated with atomic crystal structures.

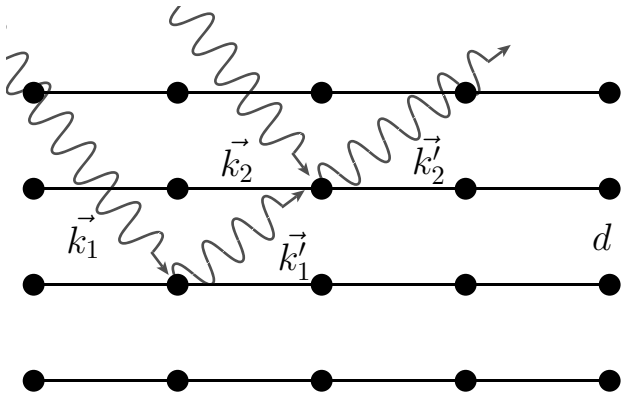

Figure 2.4: **Bragg Diffraction Condition.** The diffraction condition is defined by the superposition of the waves after the interaction of photons with the lattice planes. Constructive/destructive interference may occur between wavevectors $\vec{k_1'}$ and $\vec{k_2'}$.

Originally formulated by Bragg, XRD can be described by a basic model consisting of X-rays reflected by multiple parallel lattices planes (see Fig. 2.4). Bragg stated that the diffraction condition for constructive interference is given by

$$m\lambda = 2d\sin(\theta) \qquad m = \pm 1, \pm 2, \pm 3, ... \tag{2.16}$$

where λ is the X-ray wavelength, d is the lattice plane spacing, and θ is the detector angle with respect to the lattice planes [45]. This condition by itself is only considerate of one possible reflection plane. Generalizing this to all possible scattering, one can interpret the scattering of the atomic nuclei to be spherically symmetric, and the diffraction condition results from the interference of the X-rays re-emitted spherical waves from the periodic scattering centers. This method from understanding XRD was developed by Laue. The diffraction conditions then generalize to

$$\begin{aligned} \vec{a} \cdot (\vec{k'} - \vec{k}) &= 2\pi h \\ \vec{b} \cdot (\vec{k'} - \vec{k}) &= 2\pi k \\ \vec{c} \cdot (\vec{k'} - \vec{k}) &= 2\pi l \end{aligned} \tag{2.17}$$

where $(\vec{a}, \vec{b}, \vec{c})$ are the primitive lattice vectors, $\vec{k}$ and $\vec{k'}$ are the initial and final X-ray wave vector, and (h, k, l) are reciprocal lattice indices [46]. The significance of these conditions is made clear by considering the relation $\vec{K} \cdot (\vec{a} + \vec{b} + \vec{c}) = 2\pi(h + k + l)$, which comes directly from the definition of a reciprocal lattice vector, $\vec{K}$. From this, we now have

$$(\vec{a} + \vec{b} + \vec{c}) \cdot (\vec{k'} - \vec{k}) = \vec{K} \cdot (\vec{a} + \vec{b} + \vec{c}) \tag{2.18}$$

$$(\vec{k'} - \vec{k}) = \vec{K} \tag{2.19}$$

which restates the Laue condition in simpler form. If the wavevector change is equal

to a reciprocal lattice vector, then constructive interference will occur [47].

A concept that is useful for understanding the diffraction conditions is the Ewald sphere. Named after its creator, the Ewald sphere was developed to visualize the points on the reciprocal lattice that satisfy the diffraction condition. Consider the case for elastic scattering where $|\vec{k'}| = |\vec{k}|$. The integration of all possible points, $\vec{k'} - \vec{k}$, traces a sphere in k-space that is centered at $\vec{k}$, called the Ewald sphere. Thus, if a reciprocal lattice point lies on the sphere's surface the Laue condition, Eq. 2.17, is satisfied. An image of Ewald sphere demonstrating an example of this is shown in Fig. 2.5.

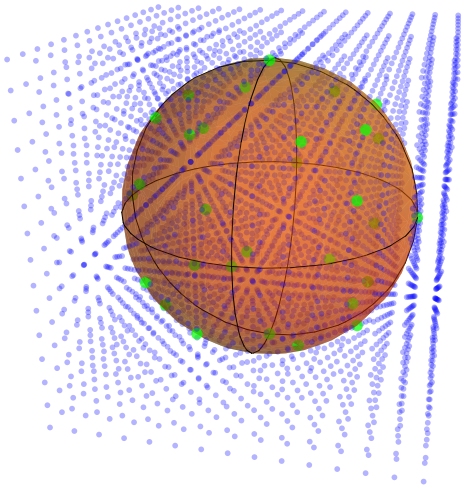

Figure 2.5: **XRD Ewald Sphere.** The Ewald sphere (orange) coincident with several reciprocal lattice points (green) in the reciprocal lattice (blue).

With the above considerations, an XRD experiment can be used to identify crystal orientation. Specifically, the crystal phase of a thin film can be identified. Typically, this is done by measuring the Bragg reflections associated with crystal planes that are parallel to the substrate surface. The geometry of the X-ray source, thin film, and detector is illustrated in Fig. 2.6. The two parameters which are varied during a measurement are 2θ and ω. How these values are set depends on the type of

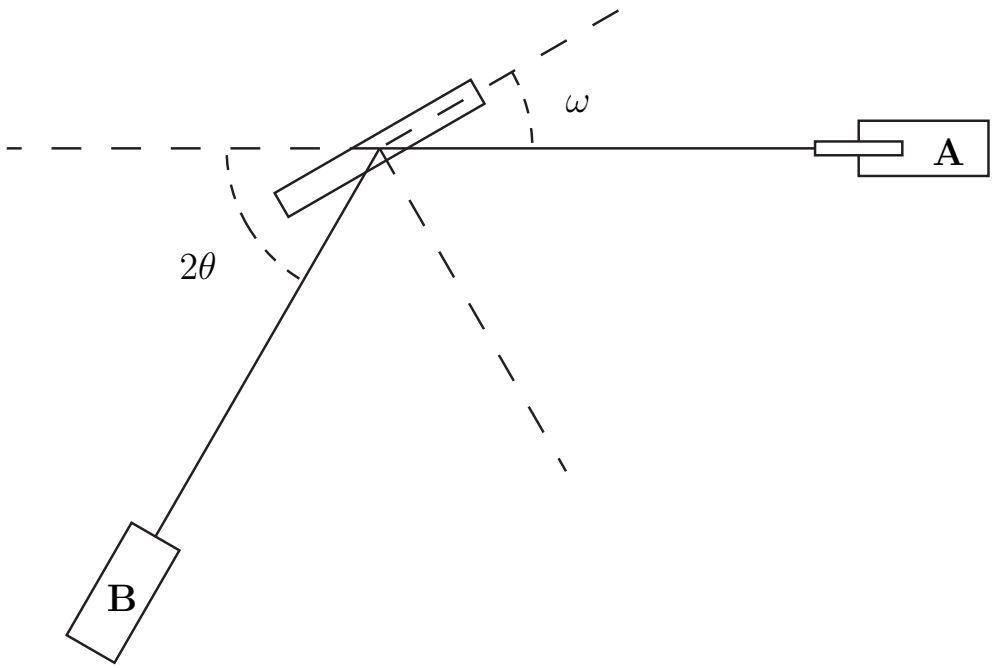

Figure 2.6: **XRD Geometry. A** X-ray radiation source. **B** X-ray detector.

measurement.

The two most commonly used measurements are the 2θ-ω coupled scan and ω scan (also called a rocking curve). The 2θ-ω scan maintains the relation $\theta = \omega$ while slowly adjusting 2θ through a specified range. When doing a quick measurement this range is typically 10-80°. The coupling between 2θ and ω provides that the detector always looks at specular reflections. Of course, destructive interference will occur except for angles where the Bragg condition is satisfied. The detector's X-ray count will increase sharply at these angles, which identify the crystal plane's Bragg reflections. For example, Bi_2Te_3 can be grown on $\langle 0001 \rangle$ Al_2O_3. The desired growth phase for Bi_2Te_3 is its $\langle 0001 \rangle$ orientation, perpendicular to the substrate surface. Therefore, only $\langle 000x \rangle$ reflections should be observed, and any other peaks in the 2θ-ω scan will indicate a different phase.

Even when the desired growth phase is obtained, distortions that tilt the surface of

the thin film resulting from defects can also occur. This could be from screw and edge defects, or even twinning. This misshaping of the film, or mosaicity, is determined by a rocking curve measurement. For rocking curves, the values of 2θ and ω are set to a position corresponding to one of the diffraction peaks found in the 2θ-ω scan. Then the value of ω is adjusted in a small range about its original position. The X-ray counts are collected for the range of ω and will appear as a single peak. The full-width half maximum (FWHM) of these peaks is used to measure the level of mosaicity in the film. High quality epitaxial films should have a FWHM of 0.1° or less. This measurement is the most substantial evidence that a thin film was grown in the correct phase and copies the underlying substrate crystal surface (i.e. epitaxial). The rocking curve and 2θ-ω scans are supportive of the quality of thin films grown for the research presented here, but are not the only evidence as *in-situ* electron diffraction also serves an extremely important propose in determining quality.

2.2.2 X-ray Reflectivity

The Bragg diffraction condition suggests that as the angle decreases, constructive interference will occur for planes separated by larger distances. This can be used to the advantage of the experimenter to produce diffraction from larger structures, such as the thin film's top and bottom surfaces. Although X-rays will scatter when interacting with atomic planes, they can also scatter at interfaces given the media on either side of the interface have a sufficiently different densities. This is certainly the case with the top surface of the film, and usually the case with the film's substrate interface. Therefore, when a 2θ-ω scan is performed at very low angles diffraction peaks can be observed from the constructive/destructive interference of X-rays reflected at the film interfaces. This technique, called X-ray reflectivity (XRR), is one of the most reliable ways to measure thin film thickness. The interfence peaks at these low angles are called Kiessig fringes, and may be either well defined or washed

out by the background X-ray counts. The visibility of these fringes is dependent on the quality of the film. A larger roughness results in less visible fringes and a larger background.

Given the fringes are well defined in a low angle 2θ-ω scan, the Bragg condition can be used to obtain the thickness of the film from the slope of $\sin^2\theta_i$ vs. n_i given by

$$\sin^2\theta_i = \theta_c^2 + (n_i + \delta)^2 \frac{\lambda^2}{4t^2} \tag{2.20}$$

where θ_i is the angle of the i^{th} fringe maximum/minimum, θ_c is the critical angle for total internal reflection, λ is the X-ray wavelength, t is the thickness, and δ is either 0 or 0.5 if i is a minimum or maximum respectively [48]. To eliminate the need for labeling the peaks with their index, we can simply use neighboring peaks to calculate the thickness. The slope of Eq. 2.20 with some simple algebra yields

$$t = \frac{\Delta n \lambda}{2\left[\sqrt{\sin^2\theta_{i'} - \theta_c^2} - \sqrt{\sin^2\theta_i - \theta_c^2}\right]} \tag{2.21}$$

where Δn is the difference in index between the i^{th} and i'^{th} fringe.

The geometry of the XRR experiment is identical to that of a typical 2θ-ω scan (see Fig. 2.6). The only significant differences are the source beam spread and low angles. To calculate film thickness from a 2θ-ω measurement, the angles at which the Kiessig fringes occur are determined. Then they are used either to fit Eq. 2.20, or determined by Eq. 2.21.

2.2.3 X-ray Photo-emission Spectroscopy

X-rays are not just useful for diffraction experiments. Photo-emission of electrons can provide a plethora of information about a material and its electronic structure. For instance, ARPES has become a workhorse for mapping out band structures. However,

X-ray photo-emission spectroscopy (XPS) is one of the highest resolution methods for determining chemical composition, and is a particularly important characterization method employed in the tuning of TI alloys. Therefore, it is worth reviewing its basic principles.

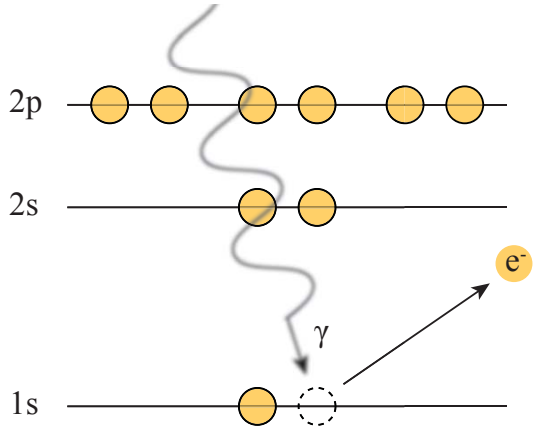

Figure 2.7: **Photo-emission Process.** Energy Diagram showing the interaction of a photon with a core electron

Photons can be adsorbed by atoms resulting in the excitation of electrons into higher energy states. If this excitation is greater than the binding energy of the electron, the electron breaks free from its nucleus and ejects into a scattering state. This photo-emission process occurs when the incident photons are of X-ray energies. Very high resolution emission lines are produced in this process. Since the incident photon energy is known, the electron detector can infer the electron's binding energy and consequently its state. The binding energy of electrons in various states are different for each element. Using this information we can determine whether a detector count came from a particular element in the sample material.

To obtain quantitative chemical composition information, the background subtracted emission counts at particular binding energies are fit to multiple Gaussian-Lorentzian product peaks, unique to certain elements. An integration of these curves giving the total detector counts from each element provides the necessary informa-

tion for determining the ratio of elements in the compound. While other information can be extracted using XPS spectra, the main purpose for the experiments here is to determine the chemical formula of alloy thin films (e.g. $(Bi_{1-x}Sb_x)_2Te_3$), which has a continuous range of stable compositions for $x = 0.0$-1.0.

2.2.4 Reflection High-Energy Electron Diffraction

Electrons are matter waves, and therefore they also can interfere with each other resulting in diffraction phenomena. At appropriate energies, electron beams can be used to determine crystal structure similarly to X-rays. Electron diffraction became extremely popular soon after this realization in material characterization due to a few main advantages over XRD. First, the wavelength of the electron beam is easily tuned by simply changing the accelerating voltage of the source electron gun. Second, the beam intensities that can be produced are much higher than that of an X-ray source. To compare, electron diffraction patterns can be acquired almost instantly whereas a single 2θ-ω XRD measurement can take from minutes to an hour to acquire a diffraction pattern. This allows one to see the pattern evolve in real-time, for example, during crystal growth. The third reason for using electrons is that they are charged particles, and are deflected by electro-magnetic fields thus allowing one to steer and focus the source beam.

In its original incarnation, low-energy electrons (20-200 eV) were used in crystallography because their penetration depth is very low, and the back-reflected electrons produce a diffraction pattern the was very surface sensitive. This effectively removes the crystal lattice periodicity in the direction perpendicular to the surface. In reciprocal lattice space, the points on the lattice are now rods that extend infinitely in the direction perpendicular to the sample surface. The Laue diffraction condition, Eq. 2.17, is therefore satisfied by the Ewald sphere intersections with these rods instead of points. An illustration of this is shown in Fig. 2.8. Using low-energy electron

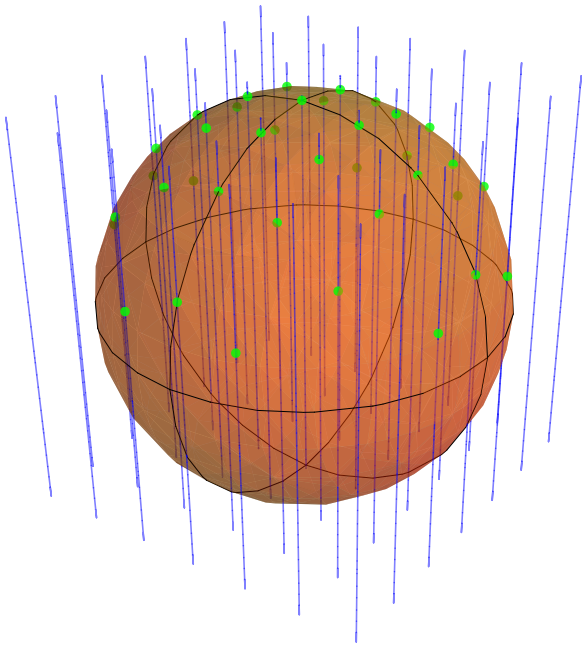

Figure 2.8: **RHEED Ewald Sphere.** Ewald sphere (orange) intersects with reciprocal lattice rods (blue) at points (green) on these rods where the Laue diffraction condition is satisfied.

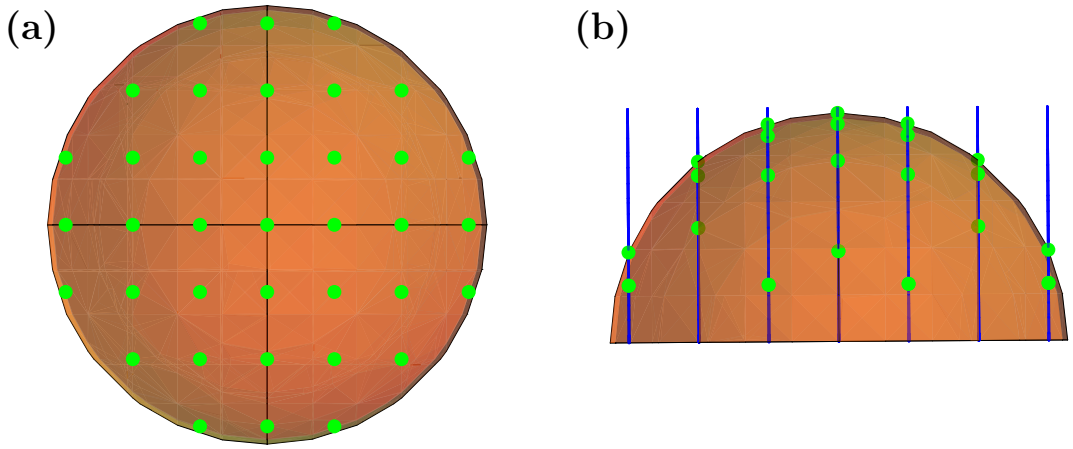

Figure 2.9: **RHEED and LEED Projections of Ewald Sphere.** Projections of the Ewald sphere and its intersections with reciprocal lattice rods for both LEED (a) and RHEED (b) geometries.

diffraction (LEED), surface crystal structures can be determined and also provide information about surface reconstructions. However, low-energy electrons are susceptible to inelastic scattering events and are not very useful at higher temperatures.

High-energy electrons (10-40 keV) reduce the inelastic scattering events, and produce sharp diffraction peaks. But now, the penetration depth is higher. To maintain surface sensitivity, the electron beam is aimed at a grazing incidence. The diffraction condition is still satisfied for the intersections in Fig. 2.8. However, the radius of the Ewald sphere is much larger, and the diffraction pattern reveals a different projection in reciprocal lattice space. This reflection high-energy electron diffraction (RHEED) is the single most important *in situ* material characterization technique employed for the MBE system. Perpendicular and parallel projections of the Ewald sphere are illustrated in Fig. 2.9, comparing the diffraction patterns obtained from both methods. The electron detector is usually a phosphor screen that emits light when an electron is interacts with it. These screens are two dimensional detectors and sample a large section of reciprocal space rather than just a point. The geometry

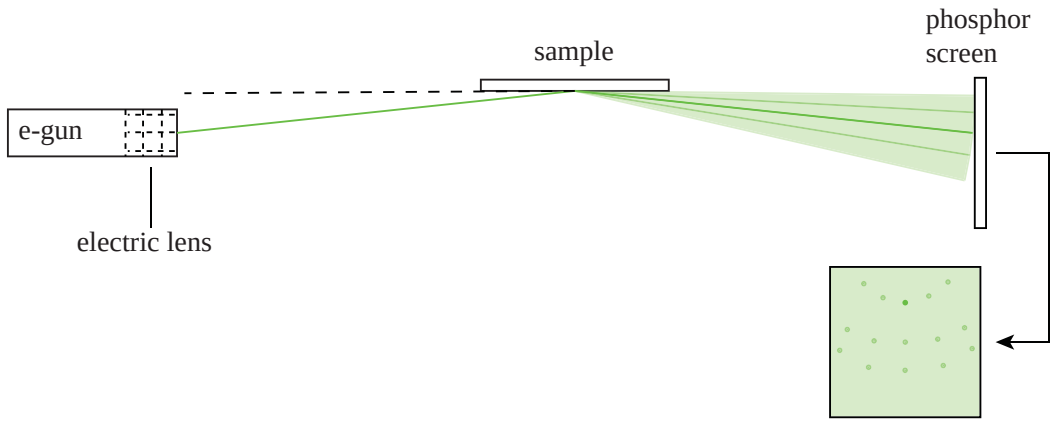

Figure 2.10: **Geometry of RHEED Setup.** The electron gun is equiped with an electric lens that both steers and focuses the beam on the sample at the appripriate angle. Scattering along with the diffracted beams then become incident on the phosphor screen.

of the RHEED setup is shown in Fig. 2.10.

It took some time to develop the theory behind RHEED due to existence of several phenomena. Eventually, techniques for determining various features in the patterns were developed [49]. The most prevalent of these features are Kikuchi lines and streaking. Kikuchi lines, which are lines connecting the diffraction maxima in the pattern, are the result of inelastic scattering events that are much more likely with a low angle incidence. Streaking, which is the elongation of the diffraction maxima, is the result of broadened reciprocal lattice rods from disordered surfaces. The rods become cylinders and the Ewald sphere intersection is now a cut through the rods' cross-section. The spots in the diffraction pattern become elongated vertically appearing as streaks. Both of these phenomenon are important to identify as they are prevalent in both substrate and thin film diffraction patterns. The existence of point-like diffraction maxima and Kikuchi lines are important to verify the quality of the substrate before growth. On the other hand, it is unlikely that the quality of an MBE grown film would produce such a pattern. Typically, the standard is to observe streaks form on the first order diffraction peaks (as called the first Laue circle). Films are inherently disordered from terraces, dislocations, and point defects. All of this disorder contributes to the broadening of the reciprocal lattice rods. As a result, the film is likely to produce streaks for, at most, two Laue diffraction circles and not more. This is considered an indicator of a high quality film, and we will see the comparison to the STM topographic images later.

2.3 The Custom MBE Design

The MBE system was constructed with the effusion and *in situ* characterization considerations discussed in previous the sections. The system was also designed for inter-operability with an existing scanning tunneling microscope. The main objective

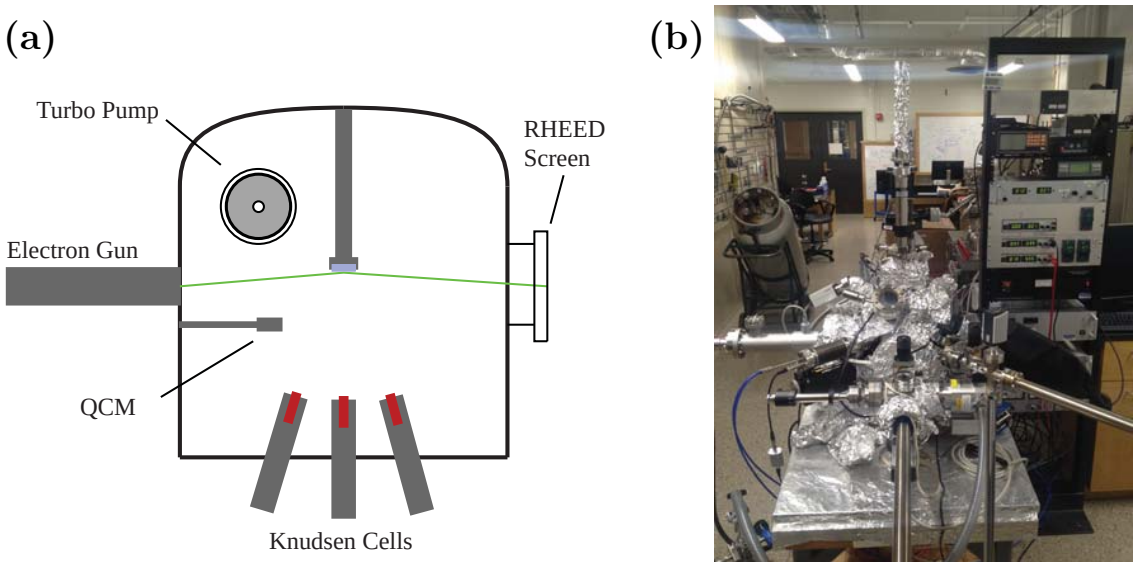

Figure 2.11: **Custom MBE System.** (a) Schematic depiction of MBE vacuum system with components and geometry. (b) Actual depiction of the MBE system.

is to perform the seamless transfer of films from the MBE vacuum chamber to the STM vacuum chamber without exposure to atmospheric gases.

To perform this kind of transfer, there are two general approaches. The first approach is to create a combined MBE/STM vacuum system where physical transfer of the samples is trivial. The second is to transport the sample using a vacuum shuttle system. The former requires a huge capital investment. It also does not allow for use of the MBE while STM measurements are being performed because STM is a very noise sensitive measurement and mechanical pumps will degrade the quality of measurements. The STM system is usually locked in a sound proof room and all mechanical noise must be eliminated (i.e. turbomolecular pumps). The latter solution, while less convenient, is more cost effective and flexible. The vacuum shuttle is the chosen method for the MBE design here. In either case, the crystal substrates on which films are grown must be attached to the final sample holder, which is used for STM measurements. Once these design considerations were taken into account, all other aspects were determined including the K-cell configuration, RHEED system, and vacuum pumps.

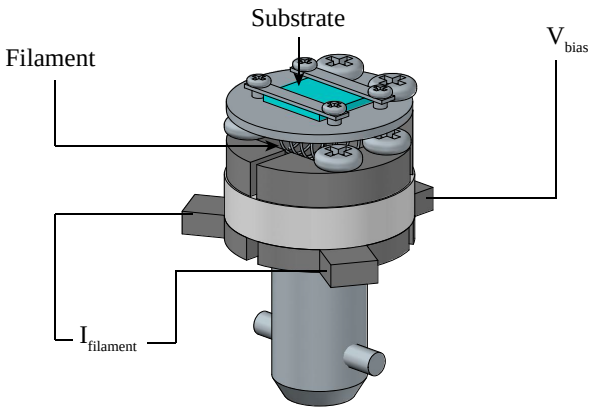

Figure 2.12: **MBE/STM Custom Sample Holder.** This sample holder is a modified version of the Unisoku sample holder used in their low temperature STMs. The top plate provides clamps for the substrate and the STM bias voltage which is provided by the plate as well. The filament is used to heat the plate and substrate during growth.

The actual system built, Fig. 2.11(b), comprises of six K-cells of different types. The K-cells are directed upward from the bottom of the chamber towards the substrate which is mounted on a customized Unisoku style STM sample holder, Fig. 2.12. The distance from the top of the K-cell crucibles to the substrate usually around 9in. The substrate sizes are a maximum of 10×10 mm which gives a distance-to-width ratio (r_c/r_s) of approximately 22:1. This ratio provides a very uniform molecular beam flux (see Fig. A.1). The angle of incidence is $\sim 23°$, similar to Fig. A.1. The RHEED system used in this setup is a Staib Instruments 15 keV electron gun with an 8in phosphor screen.

The sample holder, Fig. 2.12, is a variation of a Unisoku STM sample holder used for heating samples in vacuum. The top plate serves two purposes. The first purpose is to facilitate the application of the sample bias voltage, required to perform STM measurements. The second purpose is to clamp the substrate to a position above the heating filament. The filament is made of 0.25in diameter Tungsten wire, and is capable of bringing the substrate temperature to ∼500 °C. Radiative heating of this kind is also very stable for lower temperature control in the range of 100-300 °C.

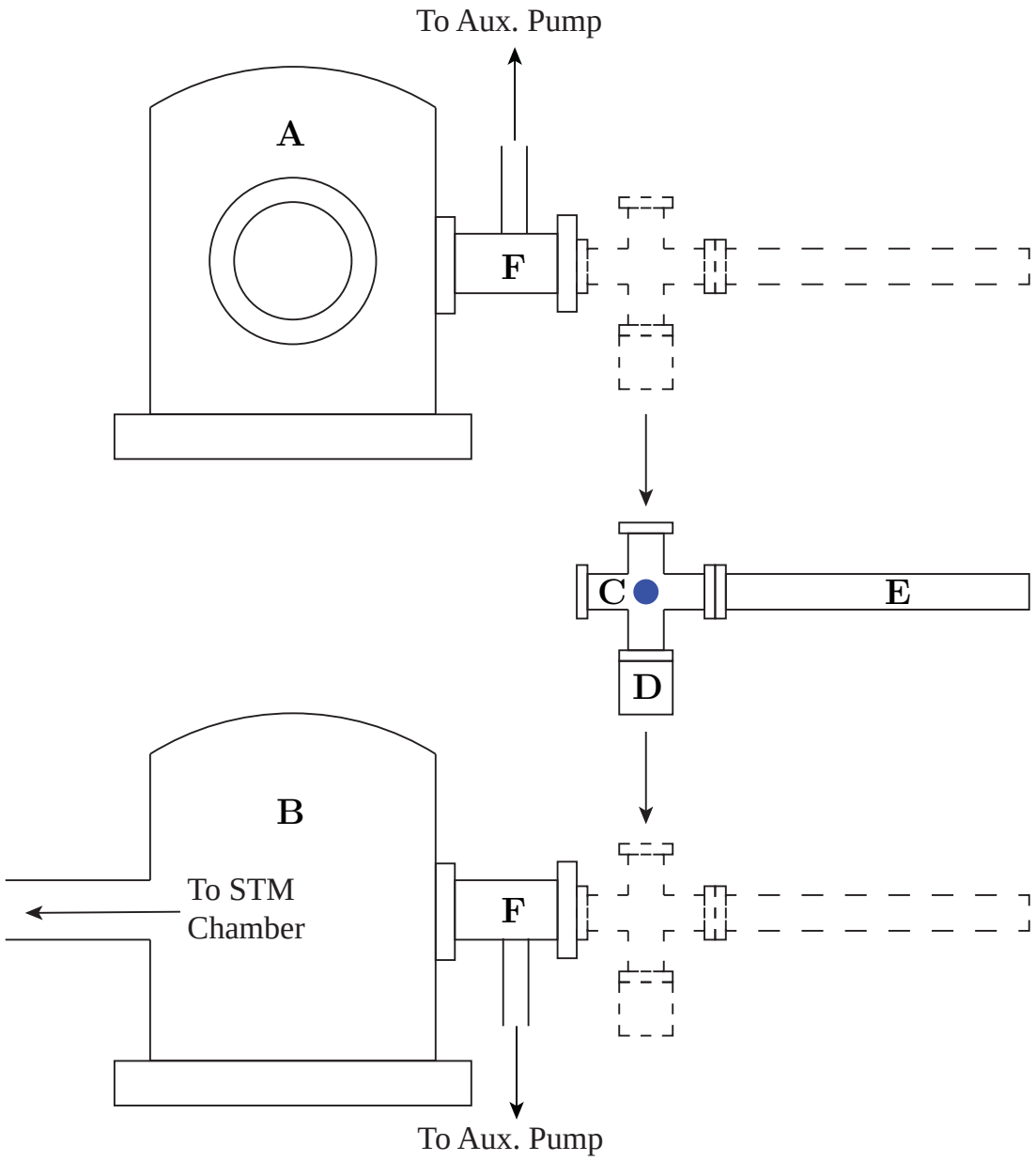

Figure 2.13: **Custom Vacuum Shuttle System.** **A** Primary MBE vacuum chamber. **B** STM preparation chamber. **C** Vacuum shuttle chamber holding the sample (blue). **D** Non-evaporable gettering pump. **E** Vacuum shuttle transfer arm. **F** Vacuum interlock sections.

To measure the molecular flux, a retractable QCM is installed to precisely measure deposition rates from each K-cell. Typically, the QCM is at a fixed point in the vacuum chamber, and the tooling factor is used to calibrate the measurement from each K-cell. The setup here is simpler in that the QCM can extend to the position of the substrate where the tooling factor is 100%, or 1:1.

All of the features mentioned so far ensure a stable, reliable, and high quality system for growing thin films. However, it is useless for our purposes if the films cannot be transferred to an STM vacuum system without exposure to air. The gases in the atmosphere can react with or be absorbed by the thin film surface making an STM experiment impossible. As mentioned earlier, a vacuum shuttle system is employed to solve this problem in a flexible way. Fig. 2.13 depicts the basic operating principle of the shuttle designed for the MBE system. It consists of a small four-way vacuum fitting with a magnetic transfer arm attached. The vacuum pressure in the shuttle is maintained by a non-evaporable getter (NEG) compound. The NEG is thermally activated in a UHV environment, and a chemical reaction begins. This reaction continuously pumps the reactive gases in the chamber. This particular pump is able to maintain a vacuum level of $\sim 10^{-9}$ Torr.

To perform the transfer, the shuttle is first attached to an interlock that is then evacuated by an auxiliary turbomolecular pump. Now the vacuum is continuous between the main MBE chamber and the shuttle. The gate valves on either side of the interlock are opened, and the sample holder can be extracted. The reverse procedure is performed to remove the shuttle. Transfer into the STM chamber is performed the same way.

High quality samples grown in the MBE system have exhibited no evidence that surface contamination results from this transfer process. High resolution STM images were acquired during the initial stages of the MBE system's operation. As an initial experiment, Bi_2Te_3 thin films were grown and measured with STM as a proto-

typical example to demonstrate the operation. These measurements, along with the operating principle of STM, are discussed in the following chapter.

Chapter 3

Experimental Techniques: Scanning Tunneling Microscopy

In the previous chapter, the methods involved in the production and optimization of thin films, specifically TI materials, were discussed. The main objective after developing a novel TI thin film is to determine nanoscale physical and electronic properties. To do this, we use scanning tunneling microscopy and spectroscopy (STM/STS). It is the highest resolution method for probing the physical and electronic structure of crystal surfaces in real space. Because of this, STM has been a very successful complement to ARPES studies in the field of TIs. This comes in part from the highly localized nature of the technique, as well as the tunneling spectroscopy energy resolution.

The STM principle of operation is based on the positioning of an atomically sharp metallic tip within Ångstroms of a crystal surface. When the atomic potentials are separated by this distance the orbital wave function of electrons in the crystal and also in the tip's closest atom begin to overlap and share a finite sized tunneling barrier. Upon application of a bias voltage between the tip and the crystal, the probability of a transition, where the tunneling of electron to or from the tip occurs, becomes substantial. The resulting steady current is referred to as the tunneling current.

Because every other physically significant quantity is derived from the tunneling current, its formulation will be discussed first. Then, the operating modes will be explained, followed by data from the first significant TI thin film grown with the custom MBE system.

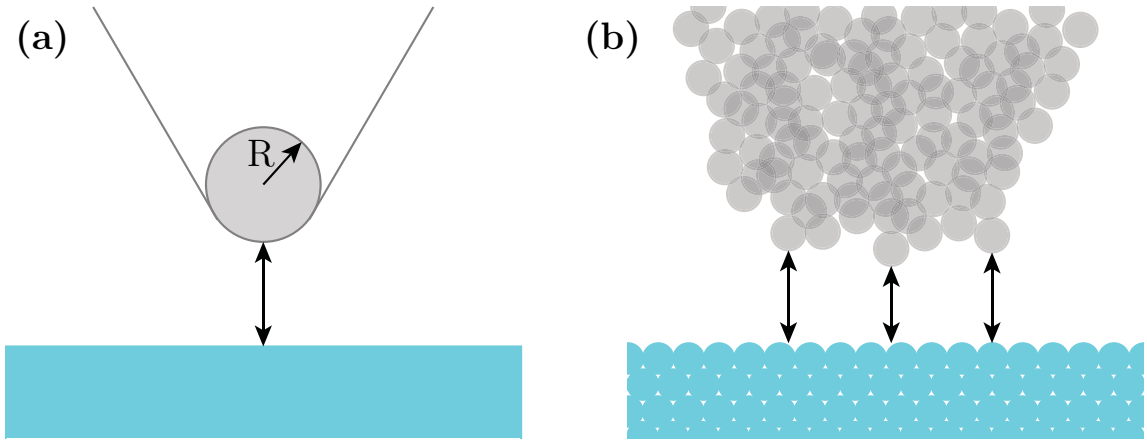

Figure 3.1: **STM Tip Models.** Illustration of a simple (a) and disordered (b) model of STM tip.

3.1 Tunneling Current

The theory of STM and the tunneling current have been developed both by application of Bardeen's tunneling current, Eq. 3.1, to a spherically approximated tip, and by Green's function formulation [50, 51, 52]. Using a spherical tip of radius R (see Fig. 3.1(a)), the tunneling current can be calculated by

$$I = \frac{2\pi e}{\hbar} \sum_{t,s} f(E_t)[1 - f(E_s + eV)]|M_{ts}|^2 \delta(E_t - E_s) \tag{3.1}$$

given the energy levels of electronic states in the sample, E_s, and of the tip, E_t. While the general solution of Eq. 3.1 for the model shown in Fig. 3.1(a) is somewhat cumbersome, a couple of approximations still yield the qualitative properties. The first approximation is of very small tip radius, $R \to 0$. From this the tunneling matrix element term, $|M_{ts}|^2$ simply becomes proportional to the probability density of each sample state at tip position, $\overrightarrow{\mathbf{r}}_0$ [51]. The sum over the tip states gives

$$I \propto \frac{2\pi e}{\hbar} \sum_{s} f(E_s)[1 - f(E_s + eV)]|\psi_s(\overrightarrow{\mathbf{r}}_0)|^2 \tag{3.2}$$

Because the experiments here use low temperature (4K) STM, a low temperature approximation for the Fermi function can be used. This obviously reduces to a step function equivalent to unity below the Fermi energy and zero above.

$$f(E) = \frac{1}{e^{(E-E_F)/k_BT} + 1} \tag{3.3}$$

$$\downarrow$$

$$f(E) = \begin{cases} 0 & \text{for} \quad E > E_F \\ 1 & \text{for} \quad E \leq E_F \end{cases} \tag{3.4}$$

So the terms in Eq. 3.2 that are nonzero correspond to $E_s < E_F$ and $E_s + eV > E_F$. By inserting the density of states (DOS), the summation becomes an integral given by

$$I \propto \frac{2\pi e}{\hbar} \int_{E_F - eV}^{E_F} |\psi_s(\overrightarrow{\mathbf{r}}_0)|^2 \rho_s(E) dE \tag{3.5}$$

which is simply proportional to the sum of states in the sample between E_F and $E_F - V$. The tunneling bias voltage, V, can be positive or negative. This means that the integrated states can be either occupied or unoccupied. If the states are unoccupied, the corresponding sign change of the tunneling current intuitively indicates the flow of electrons from the tip to the sample.

For a finite sized tip ($R > 0$), the tunneling current at low temperature is

$$I = \frac{8\pi^3 \hbar^3 R^2 e^{2\kappa R} e}{m^2 \mathcal{V}} \int_{E_F - eV}^{E_F} |\psi_s(\overrightarrow{\mathbf{r}}_0)|^2 \rho_s(E) dE \tag{3.6}$$

where $\mathcal{V}$ is the tip probe volume. $\kappa = \frac{\sqrt{2m\phi}}{\hbar}$ where ϕ is the work function for the sample surface. It is different from Eq. 3.5 by only a scale factor.

Now this picture can appear to be overturned completely when one considers an actual tip micro-structure. An example of this is an imperfectly shaped probe (see

Fig. 3.1(b)). Multiple atoms near the tip of the probe can act as the nearest approach points and contribute to the tunneling current. However, the probability density from the states in the sample, $|\phi_s(E)|^2$, falls off exponentially with approach distance d. Occasionally in practice, two microscopic probes at the end of an etched wire can have similar approach distances. This is called a "double tip" and it is parasitic to the integrity of careful measurements. Thus preparing a metallic tip appropriate for high resolution measurements is extremely important.

If the tip is reasonably sharp and stable, a significant amount of information can be obtained from the tunneling current. Primarily, we can perform topographic imaging. Because insulators and semiconductors contain more tightly bound electrons, the tunneling current will be larger if the tip is directly above an atomic site and lower if the tip is in between atomic sites. The tunneling current is directly proportional to the electron density, and can thus be used to map out the atoms on the surface of a crystal lattice. This STM operation mode is called constant current tunneling. In this mode, the sample-tip bias voltage, V, is applied at a fixed value. Using a proportional-integral-derivative (PID) controller, a chosen set point tunneling current is maintained by adjusting the distance between the tip's nearest-approach distance. The probe tip is designed to be mounted to a piezo-electric tube, which can control the movement of the tip with sub-Ångstrom precision. The adjusted height of the tip and the tunneling current as a function of position is collected. If the PID parameters are chosen appropriately, the height map reveals an image of the charge density of electronic states between E_F and $E_F + V$. For semiconductors and insulators, this height map will appear as an image of the atoms at the crystal's surface. For metals, a much larger bias voltage is required to see the atoms.

Equivalently, you could use a constant tip height and measure only the tunneling current as a function of position. However, this method has disadvantages from a practical standpoint. First, the natural tilt of the sample's surface or of the tip will

prevent the tip from successfully tracking the sample's surface. Second, large jumps from terraces or debris, which is inevitable with real materials' surfaces, will cause the tip's terminating atoms to approach so close that they significantly interact with the surface. This results in a change of the tip microstructure and possibly ruins the stability required to perform the measurement. This is called "crashing".

Topographic imaging is a fundamentally important measurement on any sample because it gives us an idea of the sample quality, morphology, crystal structure, and defects. Using this information, many different experiments can be set up to probe different locations including spectroscopic measurements where the charge density is not only mapping in space but also resolved in energy.

3.2 Scanning Tunneling Spectroscopy

The tunneling current, Eq. 3.7, is proportional to the integrated electronic DOS. Therefore, the derivative of the tunneling current is proportional to the DOS. Specifically, the derivative of the tunneling with respect to the bias voltage, Eq. 3.8, gives a very clear method to measure the DOS at a particular point on the sample surface. This is more precisely the local density of states (LDOS), which is what scanning tunneling spectroscopy (STS) is used to obtain.

$$I \propto \int_{E_F - eV}^{E_F} |\psi_s(\overrightarrow{\mathbf{r}}_0)|^2 \rho_s(E) dE \tag{3.7}$$

$$\frac{dI}{dV} \propto |\psi_s(\overrightarrow{\mathbf{r}}_0)|^2 \rho_s(E_F - eV) \tag{3.8}$$

The tunneling conductance, Eq. 3.8, is measured very precisely by modulating a reference signal on top of the bias voltage. The response of the tunneling current is feed into the input of a lock-in amplifier, which produces a signal that is proportional

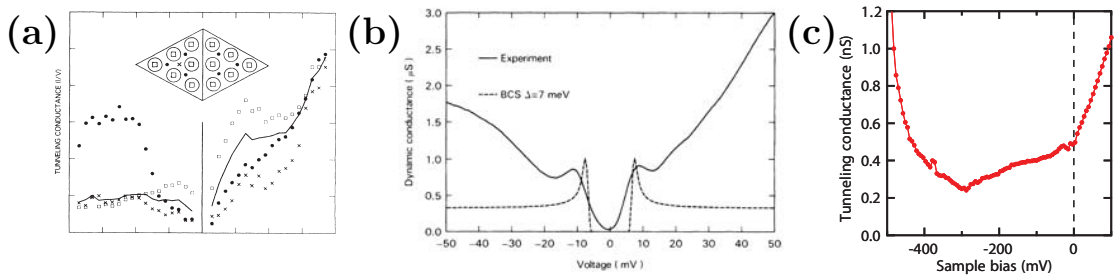

Figure 3.2: **Tunneling Conductance Examples.** (a) Differential tunneling conductance of the Silicon ⟨111⟩ surface with 7x7 reconstruction *Hamers et al.* (b) Experimental and theoretical superconducting band gap in LSCO *Kirtley et al.* (c) Bi_2Se_3 spectrum including the TI surface DOS *Hanaguri et al.*

to the tunneling conductance. In practice, the output value is used directly without any worry of the scale factor involved because the absolute value of the tunneling conductance is not strictly important. The structure and the location of features in energy axis yield the underlying physics of the electronic states. Notable examples of the physics we can observe with a dI/dV spectrum are shown in Fig. 3.2. Limited only by thermal broadening of the states and the sensitivity of the electronics being used, STS, also called dI/dV spectroscopy, provides an extremely high precision method for obtaining energy resolved information about the electronic structure in the sample being studied. Specifically, we can obtain not only an energy resolved LDOS, but also two-dimensional mappings of the LDOS, quasi-particle interference patterns, and Landau quantization.

If we position the STM tip at some location on, for instance, a semiconductor crystal surface and then sweep the bias voltage (with a small sinusoidal reference excitation from the lock-in amplifier), the resulting conductance curve will have a generally concave upwards structure centered approximately about 0 meV. This is because the Fermi energy is located at zero tunneling bias; recall that Eq. 3.8 is a function of $E_F - eV$. This is the energy gap in the states that are present in the tunneling vicinity of the tip. A fairly trivial example is the Silicon ⟨111⟩ surface, which is simply a bulk semiconductor (see Fig. 3.2(a)). Some of the first real space imaging

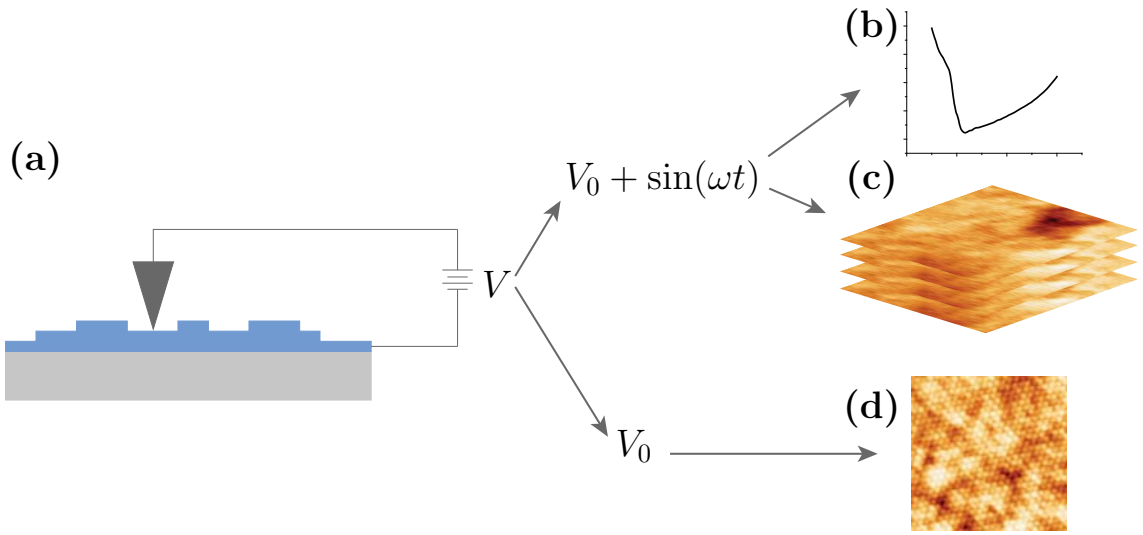

Figure 3.3: **Basic Operations of STM.** (a) The tip (dark gray) is held within Ångstroms of the thin film (blue) grown on its substrate (gray) in the MBE system. The film is biased by voltage, V. (b) Point bias spectroscopy using the lock-in reference signal. (c) Real-space and energy resolved mapping of bias spectroscopy. (d) Topographic image obtained using constant current tunneling.

and tunneling conductance of the Si-(7x7) reconstructed surface demonstrated the ability to map the band gap in materials as a function of position [53]. Another use of tunneling conductance is the high resolution that allows one to see interaction induced gaps, like the superconducting gaps in oxide materials where the gap size is measured on the order of a few meV wide (see Fig. 3.2(b)).

Additionally, the information about the electronic energy momentum dispersion can be obtained from STS. Fig. 3.2(c) shows the spectrum acquired on the Se terminated $\langle 0001 \rangle$ surface of Bi_2Se_3. The conductance is non-zero in the middle of the bulk band gap. This is the contribution of the topological surface states. Not only has this been identified in ARPES measurements, but the LDOS increases linearly as one would expect from theory calculations. Consider the differential number of states in a 2D electron system, $dN = 2\pi k dk$. The topological surface state has a linear Dirac

dispersion, $E = \alpha k$. Given this, the LDOS as a function of energy is $2\pi\alpha^{-1}E$.

dI/dV spectra acquired at a point on the surface can be extended to a 2D spatial mapping of the LDOS. This application of STS can provide impurity correlations, quasi-particle interference patterns, and most importantly for TIs, Landau-Level spectroscopy. An illustration of the operating modes of STM including the topographic imaging and dI/dV curves/maps is shown in Fig. 3.3. One significant difficulty with dI/dV spectroscopy and TI materials is identifying the surface bands' contribution to the LDOS. For example, this is problematic with Bi_2Te_3. The energy of the Dirac point is lower than the energy at the top of the valence bands. As a result, the Dirac point is not in the middle of the bulk band gap, and is not easily identified. To use dI/dV spectroscopy to probe the surface states exclusively, Landau level spectroscopy is used.

3.3 Landau Level Spectroscopy

The distinct signature of the Landau quantization of the topological surface states allows us to measure the Dirac point energy and the Fermi velocity with high accuracy. Recall from Chap. 1 that when a system of free electrons is subjected to high magnetic fields, the electrons accumulate into degenerate Landau levels. If the electron gas is confined to 2D dimensions, there is no propagation perpendicular to the plane. The Landau levels appear as peaks in the dI/dV spectrum, and the energies of these states disperse with magnetic strength. For a system of massless Dirac fermions, the dispersion is

$$E_n = E_D + \mathrm{sgn}(n) v_F \sqrt{2eB\hbar|n|} \tag{3.9}$$

where E_D is the Dirac point energy, v_F is the Fermi velocity, B is the external magnetic field, and n is the Landau-level index [18]. To actually measure this energy dispersion for a TI sample, we acquire several dI/dV spectra while applying a large

external magnetic field perpendicular to the sample's surface. Several peaks will form and will shift energy as the field strength increases. All of these peaks will disperse with field strength except for the $n = 0$ level because now $E_n = E_D + 0$ at all fields. The one non-dispersing peak, the Dirac point, provides a reference to label all the other peaks with their appropriate index. Once the peaks are labeled, they are fit with a Gaussian or Lorentzian curve to obtain their position in energy. These energies are the Landau level energies, and the dispersion of the states is given by $E_n = f(\sqrt{B|n|})$. This dispersion is also easily obtained as a function of wavevector. For an isotropic dispersion, the associated radially averaged wavevector is related to the magnetic field strength and Landau level index by

$$k_n = \sqrt{\frac{2e|n|B}{\hbar}} \tag{3.10}$$

and hence $E_n = f(\sqrt{B|n|}) = f(k_n)$ [15]. Because these energy levels form only from the surface states, Landau level spectroscopy provides a very reliable and accurate way to measure the energy dispersion of specifically surface state electrons in a topological insulator. Therefore, the technique is also robust in systems with a large, or complex, background contribution to the tunneling spectra from the bulk or tip states.

An alternative to Landau levels is to probe the quasi-particle interference. However, this is difficult to measure in TIs due to the lack of many back-scattering events. Landau level spectroscopy produces an unmistakable signature, and overcomes these problems. Furthermore, isotropic surface bands can be calculated generally from Eq. 3.10, and need not be a linear dispersion. This is precisely what is done to calculate the surface state dispersion for the trivial bulk insulator $Pb_{1-x}Sn_xSe$ in Chap. 6.

3.4 MBE Grown Bi_2Te_3

Several trial runs were performed during the process development of the custom MBE-STM sample transfer and measurement system (see Chap. 2). One initial study was the growth and measurement of Bi_2Te_3 because it is known to be grown with high quality easily. Also, the main experimental focus later will be on $(Bi_{1-x}Sb_x)_2Te_3$ with and without Cr doping. Bi_2Te_3 is intiutively a good starting point as growth processes have already been developed [54, 55, 56, 57, 58, 59]. Using these recipes and inspiration from the well understood GaAs growth physics, the custom MBE was used to grow a Bi_2Te_3 thin film and then transferred to the STM under vacuum for topographic imaging and dI/dV spectroscopy.

A high quality as-polished c-plane oriented Al_2O_3 substrate was attached to the custom STM sample holder (see Fig. 2.12). After insertion into the MBE vacuum system, the substrate was heated to 200 °C. Growth was performed by co-evaporation of Bi (99.9999%) and Te (99.9999%) from standard effusion cells using an effusion flux ratio of Te:Bi=20:1. RHEED patterns were obtained for both the bare substrate and the resulting film, shown in Fig. 3.4. The solid streaks are indicative of high quality single crystal film growth. After the growth, the sample was transferred to a low temperature STM via the vacuum shuttle illustrated in Fig. 2.13. Several topographic images and dI/dV spectra, shown in Fig. 3.5, were acquired, confirming the single crystal quality. Screw dislocations are prevalent in nearly all nucleation centers. This is likely a result of using an as-polished Al_2O_3 wafer rather than using additional chemical and temperature treatment.

Atomic resolution images reveal the existence of a few types of point defects in addition to the dislocations. Real TI crystals are rarely insulating even though the bulk band gap sizes are in the range of 200-300 meV. Typically, this conductivity arises from defects and disorder (i.e. dislocations), in which dangling bonds can

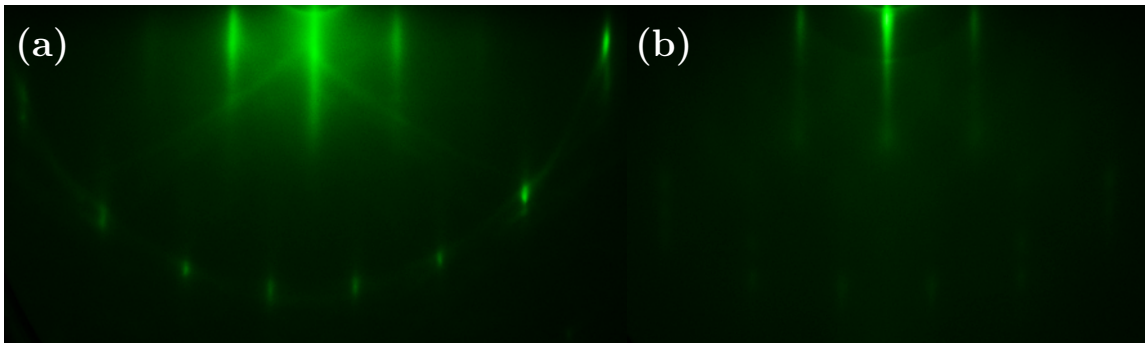

Figure 3.4: **RHEED Patterns from Bi_2Te_3 Thin Film Growth.** (a) Al_2O_3 substrate bfore growth. (b) Thin film of Bi_2Te_3 after mild annealing.

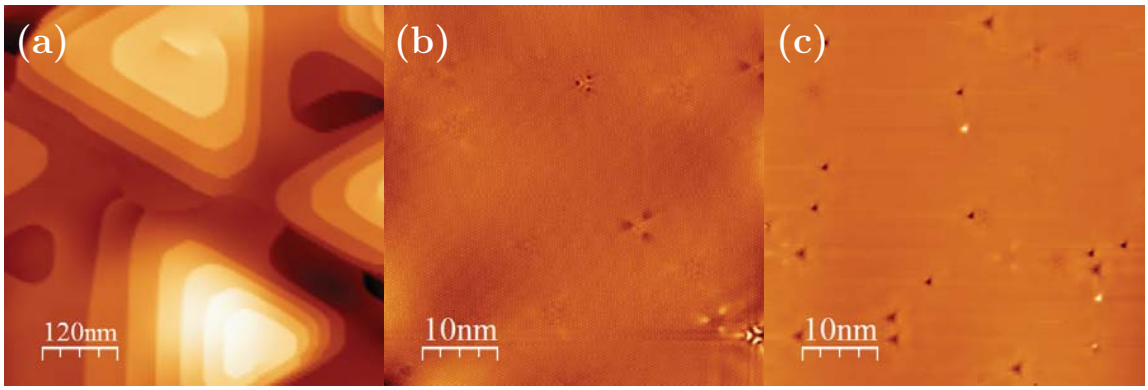

Figure 3.5: **Topographic Images of Bi_2Te_3.** STM topographic images of a Bi_2Te_3 thin film including (a) large scale, (b) atomic scale showing one kind of impurity, and (c) atomic scale showing another kind of impurity.

populate the crystal with free carriers and various oxidation states from impurities can shift the chemical potential. Even the highest quality thin films and bulk crystals of compounds such as Bi_2Se_3, Bi_2Te_3, and Sb_2Te_3, exhibit a level of bulk conductivity. So far, the following reasons have been determined. For the Bi based TIs, Se and Te vacancies tend to be the most prevalent defects. For Bi which has an oxidation state of +3, the missing Chalcogen with +4 leaves an extra electron that is unpaired. Consequently, this electron becomes a free carrier. In the case of Sb_2Te_3, the most prevalent defect is the Sb-Te anti-site defects, where the Te occupies the Sb sites in the lattice and vice-versa.

Previously, it has been found that the defects seen in our Bi_2Te_3 thin films are Te vacancies and Bi-Te anti-site defects. The anti-site defects are more prevalent

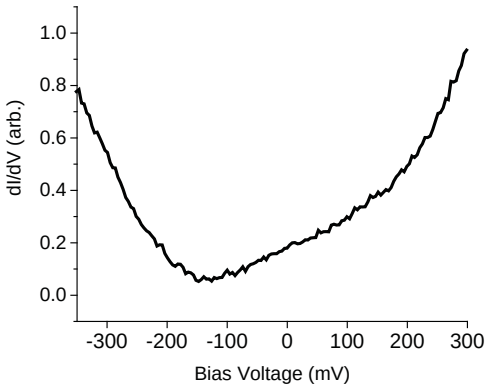

Figure 3.6: **Differential Tunneling Conductance of Bi_2Te_3.** The Differential tunneling conductance on surface of a Bi_2Te_3 thin film.

in Bi_2Te_3 than in Bi_2Se_3 and play a major role in determining the Fermi level. To confirm these properties in the current Bi_2Te_3 sample, tunneling conductance spectra were acquired to measure the bulk band gap, visualize the surface state LDOS, and determine the chemical potential. An averaged spectrum at a representative point on the surface of the film is shown in Fig. 3.6. This averaged spectrum is fairly typical in that the Fermi level (0 meV) lies close to the bottom of the conduction band in the region where the LDOS is approximately linear. The location of the Fermi level implies that it is only slightly n-type doped owing to the prevalence of the anti-site defects. The LDOS of the states in the bulk band gap, between -150 meV and 100 meV, are approximately linear. This linear portion is the contribution of the surface states to the LDOS. A rough estimate of the Dirac point location can be obtained by extrapolating this linear trend to $\frac{dI}{dV} = 0$. Estimating the Dirac point this way yields -150 meV, which is close to the top of the valance band. This value is expected based on previous measurements and calculations. However, extrapolating the location of the Dirac point this way is not accurate because the shift in the slope of the LDOS is obscured which makes the Dirac point difficult to identify. As mentioned previously, the Dirac point should be determined using Landau level spectroscopy.

Comparing this data to Bi_2Se_3, Fig. 3.2(c), highlights the difference of the properties of these two compounds. Bi_2Se_3 is heavily n-type doped, and it is difficult to achieve compensation without using very large back-gate voltages or ion-implantation techniques. However, the Dirac point is directly in the middle of the bulk band gap. As a result, we have a trade off to make when choosing a TI parent material for a particular application. Bi_2Te_3 has a Dirac point buried in the bulk valence bands, but is promising for chemical tuning. Another consideration is that Sb_2Te_3 has Dirac point at a higher energy from the valence band and is heavily p-type doped. These points are the crux of the problem with developing isolated TI surface states in an experimental setting.

The next chapter documents an experiment that attempts to isolate the tuning parameters for the carrier density in thin films of the $(Bi_{1-x}Sb_x)_2Te_3$ alloy. This material has been very successful for isolating surface state physics and detecting the quantum anomalous Hall effect.

Chapter 4

Free Bulk Carriers in Topological Insulators

Bulk electrical conductivity arising from defect doping has been a significant hurdle in producing intrinsic 3D TIs. We saw earlier how this doping affects both Bi_2Te_3 and Bi_2Se_3. The most successful technique for reducing bulk carriers in 3D TIs is to alloy Bi_2Te_3 and Sb_2Te_3. Both compounds are TIs and have nearly identical crystal structure. Therefore, no phase transition will occur from this mixture. Balancing the types of bulk carriers is only one consideration. It is also necessary to consider the exposure of the surface band crossing (Dirac point) in the bulk band gap. Specifically for observing the quantum anomalous Hall effect (QAHE), the location of the Dirac point is equally important and will remain a consideration for later when the magnetic doping is added. Before attempting to create a quantum anomalous Hall insulator, it is necessary to develop the growth process and understand the factors that contribute to the carrier tuning in $(Bi_{1-x}Sb_x)_2Te_3$. These are the first steps toward creating a platform for observing novel phenomenon arising from the surface bands in TI materials.

4.1 The $(Bi_{1-x}Sb_x)_2Te_3$ Alloy

Previous studies of $(Bi_{1-x}Sb_x)_2Te_3$ (BST) reported tuning of the chemical potential by controlling only the Sb:Bi composition ratio. A few studies indicated "optimal" compositions including $x = 0.96$, $x = 0.5$ and even $x = 0.47$ [60, 61, 62]. The first ARPES study demonstrated the ability to tune the chemical potential to the charge

neutral point ($E_F \approx E_{DP}$) [60]. This was followed by two transport studies, both indicating a different composition for lowest carrier density [61, 62]. The only notable STM measurement done on this system was quasi-particle interference imaging, where the authors indicated the existence of higher energy surface bands that coexist with the topological surface states [63]. In this experiment, STM and STS were used to probe the electronic and crystal properties of BST thin films grown using the custom MBE system described earlier. In contrast to varying the composition ratio, the growth conditions were used as a tuning parameter, which shows the multi-variate dependence of the BST electronic properties. Identifying this multi-variate dependence can also explain the variance of past results. The MBE growth conditions can significantly affect the concentration of certain defects, and this is especially true in Bi_2Te_3, where both anti-site and vacancy defects are prevalent.

A particularly important parameter is the substrate temperature during and after the growth. Bi_2Te_3 and Sb_2Te_3 are typically grown at temperatures between 150-250 °C. Higher growth temperatures have been known to produce improper nucleation phases for Bi_2Te_3 [59]. However, such low substrate temperatures reduce adatom surface diffusion, and can produce poor crystallinity. One reason to use lower growth temperatures, especially for BST, is that the sticking coefficient of higher vapor pressure species, such as Sb_2, is better. The fact that Sb does not evaporate as an atomic gas is problematic because not only do the Te_2 molecules need to chemisorb to a pair of Bi/Sb sites, but Sb_2 must also do the same. We find that low growth rates at low temperatures helps with getting a high success rate for growing BST films. This is consistent with previous studies. However, low temperatures and reduced mobility results in the formation of taller nucleation centers, and possible island type growth, which results in a rougher film.

A two step growth process is one technique that has been used to solve the growth problems[42, 59]. The film is initially deposited at a low temperature to obtain

the proper nucleation phase and is then annealed at a higher temperature during a secondary growth phase or post-growth. The higher temperature gives remaining adatoms a higher surface mobility allowing them to fill in the gaps between the nucleation islands that form on top of the layered growth. However, the higher annealing temperature can have adverse effects on the electronic properties, which is counterproductive to carrier concentration tuning. To understand these effects, two nominally similar BST films were grown, and one is annealed at a higher temperature than the other. Beginning with the MBE growth of two BST thin films, it is shown here that different growth procedures yielded significantly different electronic properties, and may be contributing to the variance in BST thin film results.

4.2 MBE growth of $(Bi_{1-x}Sb_x)_2Te_3$

4.2.1 Substrate and Preparation

Much success has been made with the MBE growth of Bi_2Se_3, Bi_2Te_3, and Sb_2Te_3 on various substrates. α-Al_2O_3, also known as sapphire or corundum, has been a popular choice for its ease of preparation and high quality surface that can be obtained [42, 59, 60, 64, 65]. For the $(Bi,Sb)_2(Se,Te)_3$ compounds, c-plane $\langle 0001 \rangle$ oriented sapphire substrates are used because the surface lattice is hexagonal and mimics the c-plane symmetry of the film.

Shown in Fig. 4.1 is both the hexagonal unit cell and the unit cell viewed from the a-plane $\langle 11\bar{2}0 \rangle$ and c-plane $\langle 0001 \rangle$. Previous studies found that the energetically stable surface termination for the c-plane is a single Aluminum layer with an Oxygen layer directly below [66, 67, 68]. This layer along with the other possibilities are indicated in Fig. 4.1(b). Another study showed that an as-polished substrate will have typical steps heights of $\frac{1}{6}$ unit cell height and that annealing in Oxygen at 1200 °C significantly reduces the roughness and produces step heights equal to the unit cell

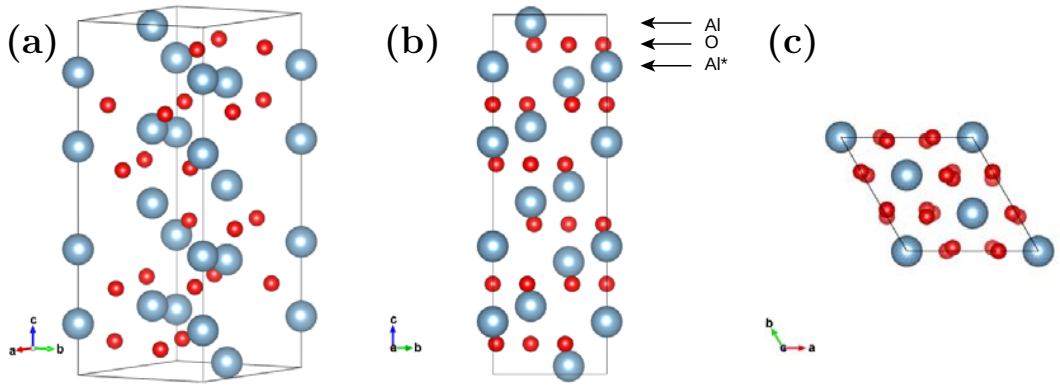

Figure 4.1: **Crystal Structure of α-Al_2O_3.** (a) Isometric view of unit cell showing Al sites (blue) and O site (red). (b) a-plane view of unit cell showing the possible termination surfaces. (c) c-plane view of unit cell.

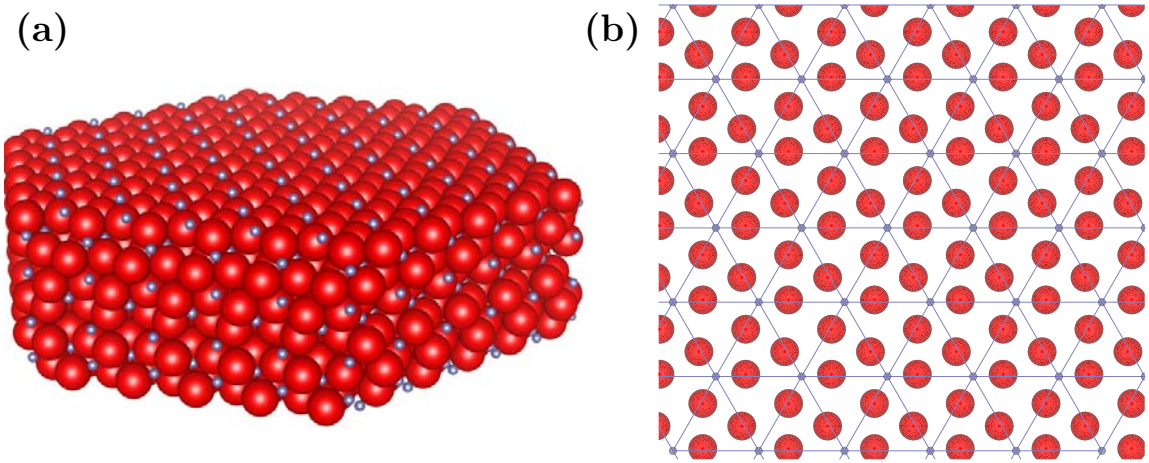

Figure 4.2: **Surface Termination of α-Al_2O_3.** (a) Isometric view of crystal with an Al terminated surface lattice showing Al (blue) and O (red) atoms. (b) c-plane projection of Al terminated surface showing Al (blue) and O (red) sites.

[69]. With an ideal Al termination (Fig. 4.2), The Al plane has atoms spaced by the unit cell hexagonal lattice parameter, $a = 4.758\,\text{Å}$, which is close to the Bi_2Te_3 and Sb_2Te_3 hexagonal lattice parameters, $a = 4.38\,\text{Å}$ and $a = 4.25\,\text{Å}$ respectively. This is gives an average 10% lattice mismatch for the BST alloy depending on the composition.

Using a similar substrate preparation to previous studies, the c-plane Al_2O_3 used here is annealed in a tube furnace at 1000 °C while flowing ultra-high purity O_2 for 12 hours. Once the substrate is cooled, it is immediately mounted to the MBE/STM

sample holder (Fig. 2.12) and inserted into the MBE vacuum system.

4.2.2 Growth Conditions

Two BST thin films were grown in the custom MBE with one post-growth annealed at a lower temperature (sample-L) and the other post-growth annealed at a higher temperature (sample-H). For each growth, the substrate was heated to 200 °C, and the films were deposited by co-evaporation of Bi (99.9999%), Sb (99.9999%) and Te (99.9999%) from standard single and dual filament effusion sources. The growth rate used was typically around 0.3-0.4 nm/min. The effusion flux ratios for sample-L were Sb:Bi=1.36:1 and Te:(Sb,Bi)=2.1. For sample-H they were Sb:Bi=1.57 and Te:(Sb,Bi)=2.2. The films were annealed after growth at 220 °C for sample-L and 300 °C for sample-H for 4 hours. After annealing, the samples were immediately transferred to the low-temperature STM using the custom vacuum shuttle system so not to expose the samples to atmospheric pressures.

4.2.3 Sample Characterization

Fig. 4.3(a,b) shows the RHEED patterns after the annealing process for each film. Both patterns indicate good crystallinity. The streaks from the sample-H are slightly sharper indicating better crystallinity. This is confirmed in real space by topographic imaging. Fig. 4.3(c,d) shows the large scale and atomic resolution topographic images of both samples. For Fig. 4.3(c), the root-mean-squared roughness was 2.3nm. For Fig. 4.3(d), the root-mean-squared roughness was 0.7nm. This is a clear indication that the higher post-growth annealing temperature improved the surface roughness.

The next important property is the alloying ratio, x in $(Bi_{1-x}Sb_x)_2Te_3$. This ratio is controlled by adjusting the relative effusion fluxes of Sb and Bi during the film growth, and can be used to tune x through the entire range from 0.0 to 1.0. x is

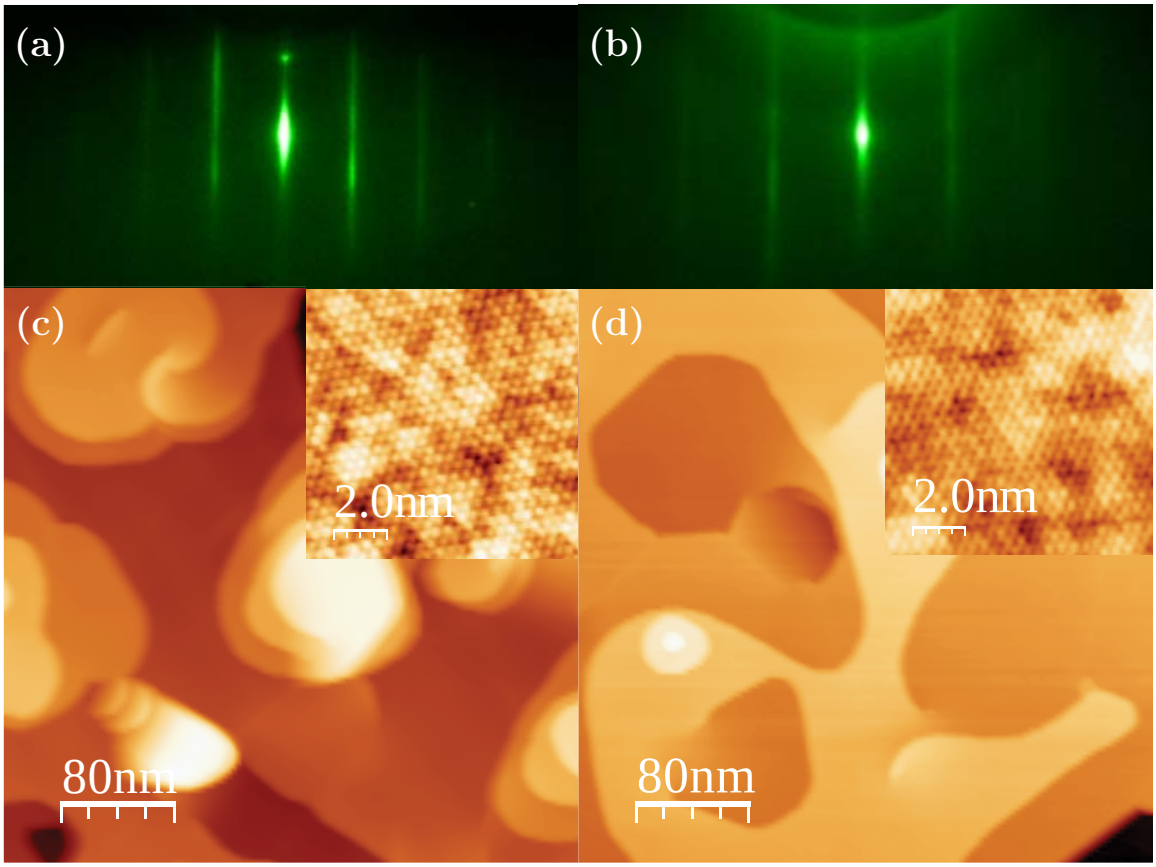

Figure 4.3: **Characterization of BST Thin Films.**(a) RHEED pattern of sample-L. (b) RHEED pattern of sample-H (c) 400×400 nm and 10×10 nm (inset) STM topographic images of sample-L. Images were acquired using a tunneling current and bias voltage of 50pA and 600mV (400×400 nm) and 550pA and 100mV (inset). (d) 400×400 nm and 10×10 nm (inset) STM topographic images of sample-H. Images were acquired using a tunneling current and bias voltage of 50pA and 600mV (400×400 nm) and 200pA and 100mV (inset).

commonly determined by a couple of ways. The first is to directly use the flux ratio Sb:Bi, which assumes that the sticking coefficient of both Sb and Bi are unity. The second is to calibrate the individual effusion fluxes to the growth rates of Bi_2Te_3 and Sb_2Te_3 respectively, which can account for the sticking coefficients. Both of these methods have intrinsic error and are only predictive of the outcome.

It is more reliable to measure x directly rather than to infer. Energy-dispersive X-ray spectroscopy (EDX), X-ray photo-emission spectroscopy (XPS), and atomic emission spectroscopy (AES) are all popular methods measuring chemical composi-

tion. To determine exactly the chemical composition of the sample-L and sample-H, *ex situ* XPS measurements are used because XPS provides very high energy resolution emission lines. The XPS results yield the chemical compositions for both sample-L and sample-H. The background-subtracted photo-emission counts are shown in Fig. 4.4. For this data, the values determined for x were 0.68 for sample-L and 0.71 for sample-H. Based on the assumption that the carrier tuning is uni-variate in x, sample-H should have a slightly lower Fermi energy. The most significantly different quantity was the Te:(Sb,Bi) ratio. For the sample-L, Te:(Sb,Bi) is 1.5, close to stoichiometric. For sample-H, it is was 1.16 which is a significant Te deficiency.

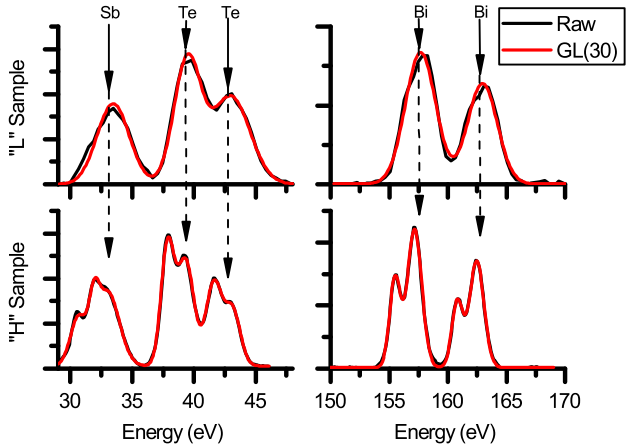

Figure 4.4: **XPS Peaks of sample-L and sample-H.** The background subtracted photoemission peaks (black) along with the Gaussian-Lorentzian product fit (red).

To verify that the composition of both samples is not the result of the formation of a different crystal phase, *ex situ* XRD measurements were also performed to complement RHEED, which only indicates the in-plane structure of the surface crystal lattice. 2θ-ω coupled scans and rocking curves were obtained for both samples using a Phillips X'pert XRD system. A Cu K-alpha source was used and alignment was performed using the Al_2O_3 (006) diffraction peak. Both 2θ-ω scans, Fig. 4.5(a,b), produced only c-plane reflections. Rocking curves, Fig. 4.5(c,d), were performed about the alignment with the BST (0015) peak yielding a full-width half maximum

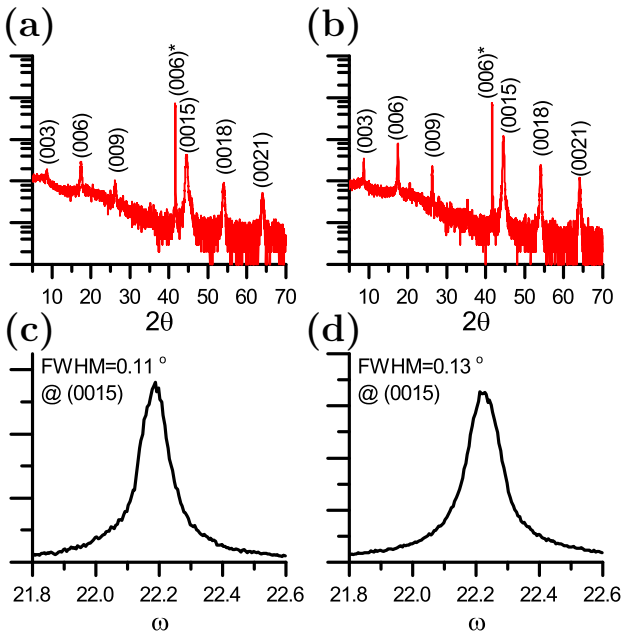

Figure 4.5: **X-ray diffraction Results for sample-L and sample-H.** (a) 2θ-ω scan. (b) 2θ-ω scan. (c) Rocking curve of sample-L about the BST (0015) reflection. (d) Rocking curve of sample-H about the BST (0015) reflection.

of 0.11 and 0.13 for sample-L and sample-H respectively. The c-plane orientation, rocking curves, and RHEED patterns indicate the correct crystal phase is undoubtedly obtained, and that the compositions measured by XPS should be the result of point defects.

4.3 STM and Landau Level Spectroscopy

Landau level spectroscopy, as described previously, was used to obtain the surface state energy momentum dispersion of each sample. A line-cut of dI/dV spectra were acquired along the sample surface with the application of various magnetic fields perpendicular, $\vec{B} = B_z\hat{z}$, to the film's surface. These spectra for both sample-L and sample-H are shown in Fig. 4.6(a,c). As expected, the ripples in the curves suggest the existence of Landau levels, and this is confirmed by their dispersion with the magnetic field. The 0T spectrum is subtracted out, and the peaks, shown in Fig.

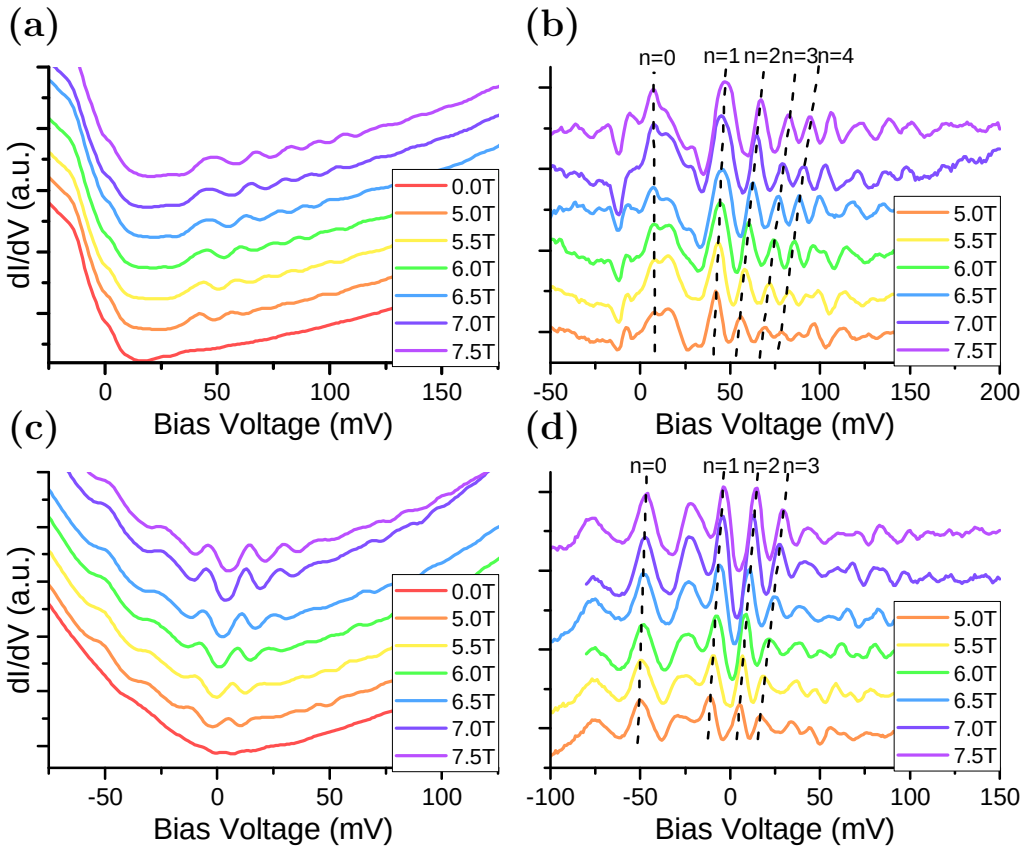

Figure 4.6: **Tunneling Conductance Spectra of BST Films.** (a) Line averaged point spectra at several magnetic fields of sample-L. (b) Background subtracted spectra of sample-L. (c) Line averaged point spectra at several magnetic fields of sample-H. (d) Background subtracted spectra of sample-H.

4.6(b,d), are fit to Gaussian curves. These peak energies are then plotted in Fig. 4.7 with respect to $\sqrt{nB_z}$, where n is the n^{th} Landau level index. The energy clearly disperses linearly for both sample-L and sample-H, and is fit to Eq. 3.9.

The most obvious difference between these two dispersions is the y-axis intercept. Recalling Eq. 3.9 shows that the intercept is exactly equal to the Dirac point energy. Of course, in STS this energy is measured with reference to the Fermi level (see Eq. 3.8). The fit to Eq. 3.9 yields $E_D = 6\,\text{meV}$ for sample-L and $E_D = -48\,\text{meV}$ for the sample-H. The Fermi velocities obtained from the slope were both approximately 4.4×10^5 m/s, which is expected for BST. This result indicates that sample-H, annealed at higher temperature, has a much higher chemical potential with respect to the Dirac

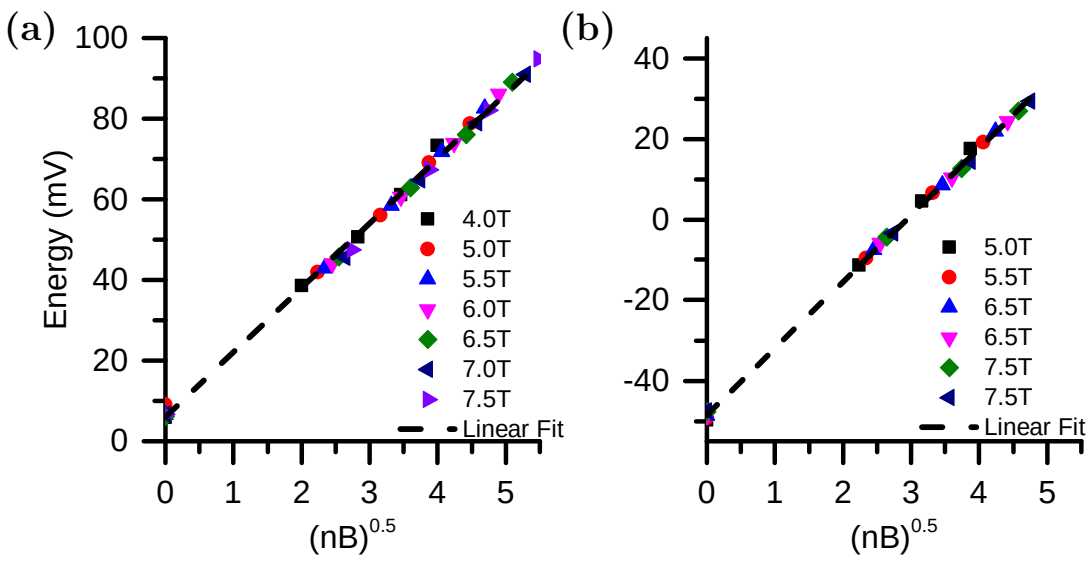

Figure 4.7: **Landau Level Dispersions.** (a) LL dispersion obtained from sample-L. (b) LL dispersion obtained from sample-H.

point. Therefore, n-type doping is likely a result of the growth conditions. This immediately suggests that the Te vacancies are more prevalent in sample-H, whereas the Te_{Bi} anti-site defect may be more dominant in sample-L. This is intuitive and consistent with previous knowledge about the tendency of vacancy formation at higher temperatures.

4.4 Discussion

These results show that the growth conditions of BST thin films affect native defects and bulk carrier concentration, adding another variable to the tuning parameter space. It was shown that the Fermi energy of sample-H is significantly higher than sample-L even though the Sb concentration was nearly the same. The Landau level spectroscopy and the calculated Dirac point energy unambiguously support this. The only meaningful difference in preparation was each film's post-growth annealing temperature. Furthermore, XPS results show a significant deficiency of Te in sample-H, whereas sample-L was nearly stoicheometric. The Te vacancies are usually cited as

the major contributing factor for n-type doping of TI materials, and the results here suggest the same.

What is learned here is that low temperature growth conditions are singificant in maintaining a lower Fermi energy. This stresses the importance of the substrate preparation and low growth rates. The diatomic evaporation of Sb poses an issue. The growth here appears to be Stranski-Krastanov mode where full layers form and then lead into island type growth. With a low enough temperature, low growth rate, and very high quality surface, low defect thin films in the range of a few nanometers are likely possible. One solution used by others is to evaporate Sb with a cracker cell. Another solution is to evaporate Sb_2Te_3 rather than an elemental source [42].

Although the chemical tuning of BST has been shown to be clearly dependent on multiple parameters, much more work is required to understand the detailed contributions from various properties. Defect formation is also not obvious as the alloy changes the formation of energies of both anti-site and vacancy defects. However, with the empirical evidence here we are in a position to explore the physics that occurs when a magnetic impurity is added to BST. We know that the surface state's degeneracy will be lifted and produce a gap. If the Fermi level lies in the gap we should be able to observe the QAHE. However, the nanoscale variations have not been studied extensively in thin films.

Chapter 5

Magnetic Inhomogeneity in $\mathbf{Cr}_y(\mathbf{Bi}_{1-x}\mathbf{Sb}_x)_{2-y}\mathbf{Te}_3$

The previously demonstrated chemical tuning, indicated that low growth and post-growth substrate temperatures are important for defect doping compensation as well as substrate quality. Adding a magnetic dopant complicates the situation even more because the surface state band gap, or massive Dirac gap, can vary in size if the doping is non-uniform. This variance has been studied in bulk crystals, but not in thin films [31]. In general, microscopic studies of magnetically doped TI thin films are lacking. So, STM/STS is used here to reveal insight into the effects that contribute to the bulk conductivity making Hall conductance measurements difficult.

5.1 Ferromagnetic $(\mathbf{Bi}_{1-x}\mathbf{Sb}_x)_2\mathbf{Te}_3$

Several transition metal dopants are considered to be suitable for producing ferromagnetism in BST. Fe, Cr, and V are all possible magnetic dopants with stable oxidation states of +3, therefore not introducing free carriers upon substitution of either Bi or Sb. So far, Cr has been the most successful candidate, even though it has a uniquely large number of different oxidation states (+3 being the most stable) [70]. Because Chromium has been found in compounds in various oxidation states, including +2, +3, +4, +5, and +6, the assumption that only the stable state in BST is +3 is not completely obvious. However, this is the consensus.

The QAHE has been observed several times in $Cr_y(Bi_{1-x}Sb_x)_{2-y}Te_3$ (CBST) thin films at very low temperatures. There are a few proposed explanations for the dif-

ficulties in observing the QAHE. Either the contributions to the Hall current from both bulk and side surface currents are adding to the conductivity, or non-uniform doping of the transition metal is causing disordered magnetism. For CBST, the bulk carriers in principle should be compensated for by mixing Bi_2Te_3 and Sb_2Te_3, and the film thickness should isolate the probing of the surface current only. This chemical tuning combined with an appropriate back gate voltage puts the chemical potential in the bulk gap and the massive Dirac gap. In principle, the massive Dirac gap size of 70 mV should allow for a large range of gate voltages where the QAHE is observed. Contrary to this, milli-Kelvin temperatures are still required.

Previous STM studies of CBST include an impurity density correlation study of the massive Dirac gap size and also a spin-polarized STM study [31, 32]. *Lee et al.* performed STS measurements on the surface of cleaved bulk CBST single crystals, and found a positive correlation between the local Cr density and the massive Dirac gap. A similar correlation calculation is performed here, but unique in that the measurements are performed using thin films grown on $\langle 111 \rangle$ $SrTiO_3$. Thin films are more directly relevant with respect to the QAHE, and thus the STM/STS measurements should be done on an analogous system due to the differences of real materials from various fabrication techniques.

The films studied here will be grown by MBE and have a similar nominal chemical composition to previous studies [23]. The target Cr substitution fraction is 5% and for and the Sb/Bi ratio Sb:Bi=9:1 which should be near the charge neutral point. Utilizing the nanoscale sensitivity of STM/STS the impurity concentrations are mapped out. The massive Dirac gap, created by the magnetism, is calculated and the spatial variations are correlated to the impurity density. It is shown in this experiment that the gap is not well formed everywhere on the surface. The implication is that conductivity may arise from impurity states that formed within the gap.

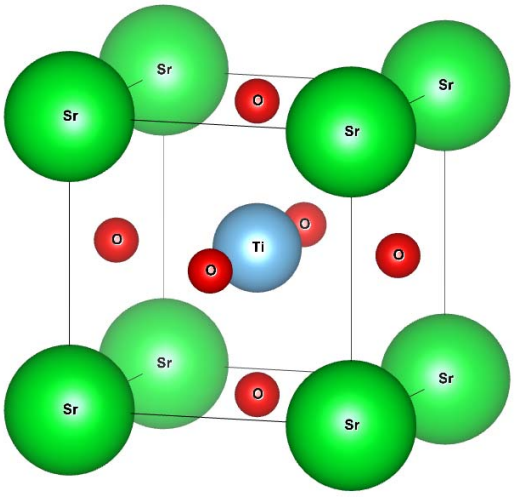

Figure 5.1: **Strontium Titanate Unit Cell.** Perovskite-type cubic unit cell of $SrTiO_3$. The cubic lattice parameter is 3.905 Å.

5.2 MBE growth of $Cr_y(Bi_{1-x}Sb_x)_{2-y}Te_3$

5.2.1 Substrate and Preparation

Al_2O_3 is often the choice substrate for epitaxial growth of TIs. However, the existence of defect induced carriers, even with chemical tuning, requires the use of a substrate with a high dielectric constant. This allows the application of a significant gate voltage to raise or the lower the chemical potential in the thin film effectively. Transport measurements rely heavily on gating even when BST is used as the platform material. $SrTiO_3$ (STO) is a good choice, and specifically the $\langle 111 \rangle$ surface orientation is effective for growing TIs because the hexagonal surface symmetry and lattice parameters are well matched. STO substrates are also used here to replicate previous studies' material quality.

STO has a pervoskite-type cubic crystal structure, Fig. 5.1. Preparation and application of STO $\langle 100 \rangle$ substrates has been developed for many years in the field of high-T_c superconducting oxide films. The development of a buffered-hydroflouric

acid (BHF) etching procedure was paramount to obtaining singly TiO-terminated $\langle 100 \rangle$ planes [71]. Coincidentally, Ti terminated surfaces can be acquired for all major surfaces including the $\langle 111 \rangle$ surface [72]. However, the $\langle 111 \rangle$ surface consists alternating electrically polarized planes of Ti^{+4} and SrO_3^{-4}. The surface can terminate with either, and is very difficult to obtain a single termination using only chemical-mechanical planarization (CMP) polishing.

More recently, the $\langle 111 \rangle$ crystal substrates have been used for epitaxial film growth. This is in part due to the development of BHF etching for this surface similarly to the $\langle 100 \rangle$ surface [73]. In addition to BHF etching, two other methods for obtaining high-quality single terminated $\langle 111 \rangle$ surfaces have been developed, including high temperature annealing and de-ionized water leaching [74]. Specifically, the water leaching method is very easy and involves only agitating the substrate in hot de-ionized water followed by high temperature baking. The likely reaction during the agitation process is

$$SrO_3 \xrightarrow{H_2O, CO_2} SrCO_3 + Sr(OH)_2$$

where no Ti related compounds would form. The reaction occurs this way because Ti and TiO are nonreactive to water. The process is finished with a high temperature annealing that removes the Sr-related compounds leaving the Ti terminated surface. The resulting desired $\langle 111 \rangle$ termination is shown in Fig. 5.2.

A similar water leaching preparation is used here to avoid the use of BHF. The procedure begins by agitating the $\langle 111 \rangle$ STO in acetone for 5 minutes followed by agitation in de-ionized water for 40 minutes at 70 °C. After this hydrogenation process, the substrate is heated in a tube furnace in a pure O_2 atmosphere for 2 hours at 1000 °C. Example RHEED patterns of the STO $\langle 111 \rangle$ surfaces imaged after the leaching preparation are shown in Fig. 5.3. Clearly, Fig. 5.3(b) shows a STO surface with

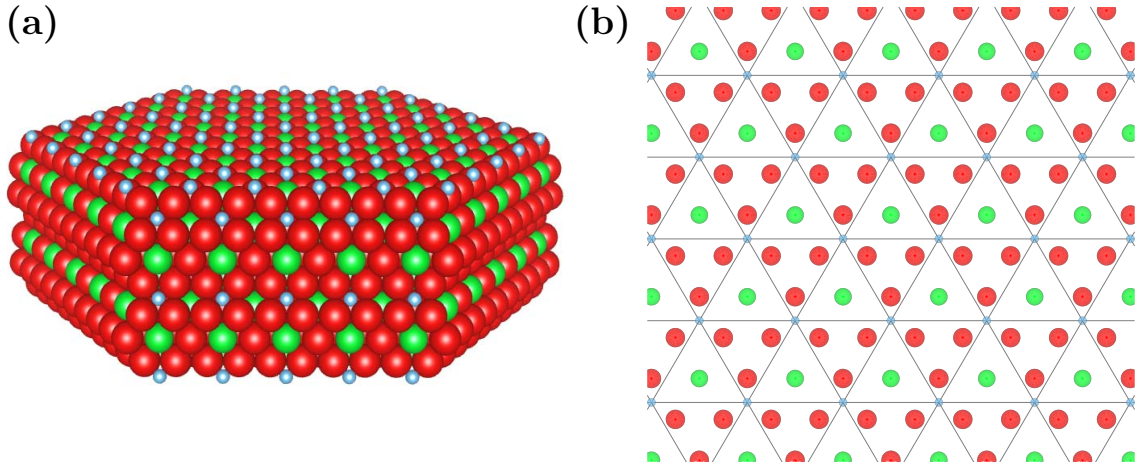

Figure 5.2: **Surface Terminations of $\langle 111 \rangle$ Oriented $SrTiO_3$.** (a) Ti^{+4} termination. Ti atoms (blue) form a hexagonal lattice separated by 5.52 Å. The Ti plane is 1.12 Å above the underlying SrO_3^{-4} plane (b) SrO_3^{-4} termination with both Sr (green) and O (red) atoms.

significantly higher quality. This is indicated by the clear diffraction peaks along each of the Laue circles. Although the first set of diffraction peaks are slightly elongated, the terrace size is likely to be very large and a single termination. It is also possible that the Ewald sphere intersection with the reciprocal lattice rods is very shallow, meaning that even a high quality surface produces a small of amount of streaking. This quality of STO surface should, in principle, seed high quality epitaxial thin films regardless of the large lattice mismatch, $\sim 20\%$.

One last thing that must be addressed is that STM requires an electrical contact to the film to apply the necessary bias voltage. Even though this problem exists for both STO and Al_2O_3, STO can be doped with Nb which pushes up its Fermi level making it a conducting substrate. A $\langle 111 \rangle$ 7% wt Nb-doped STO substrate is used for the film growth in this experiment to avoid technical issues associated with an insulating substrate. The level of doping is small enough to insignificantly affect the crystal structure and chemistry, and thus the water leaching preparation is immediately extendable to the conducting substrates.

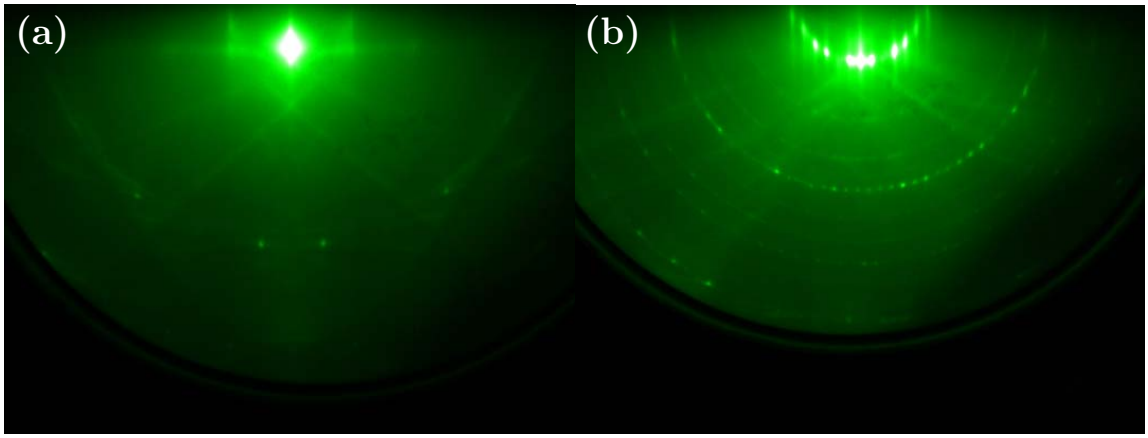

Figure 5.3: **Effect of Water-Leaching on $\langle 111 \rangle$ Oriented $SrTiO_3$.** (a) RHEED pattern of an unprepared STO substrate. (b) RHEED pattern of STO surface after water-leaching and baking.

5.2.2 Growth Conditions

After preparation, the Nb-STO substrate is transferred into the UHV system where is it heated to a growth temperature of 200 °C. The film was deposited by co-evaporation of Bi (99.9999%), Sb (99.9999%), Te (99.9999%) and Cr (99.997%) from standard single filament (Bi,Sb,Cr) and dual-filament (Te) effusion cells in the custom MBE system. The deposition rates for each source are measured by a retractable QCM and are adjusted to the desired stoichiometric ratios. For this growth, the flux ratios were Sb:Bi:Cr=10:1:1 and Te:(Sb,Bi,Cr)=10:1. RHEED patterns are monitored during growth. Solid streaks, indicative of high quality two dimensional growth, begin to form immediately after the start of the growth. After 35 minutes of growth with a rate of 0.25 nm/min, the shutters are closed and the sample is annealed at the growth temperature under continuing Te flux. The substrate before growth and the resulting thin film RHEED patterns are shown in Fig. 5.4(a,b). Immediately after annealing, the sample was transferred to our low temperature STM using the custom vacuum shuttle system. After transfer, it is immediately inserted into the STM where it is held at a temperature of 4K.

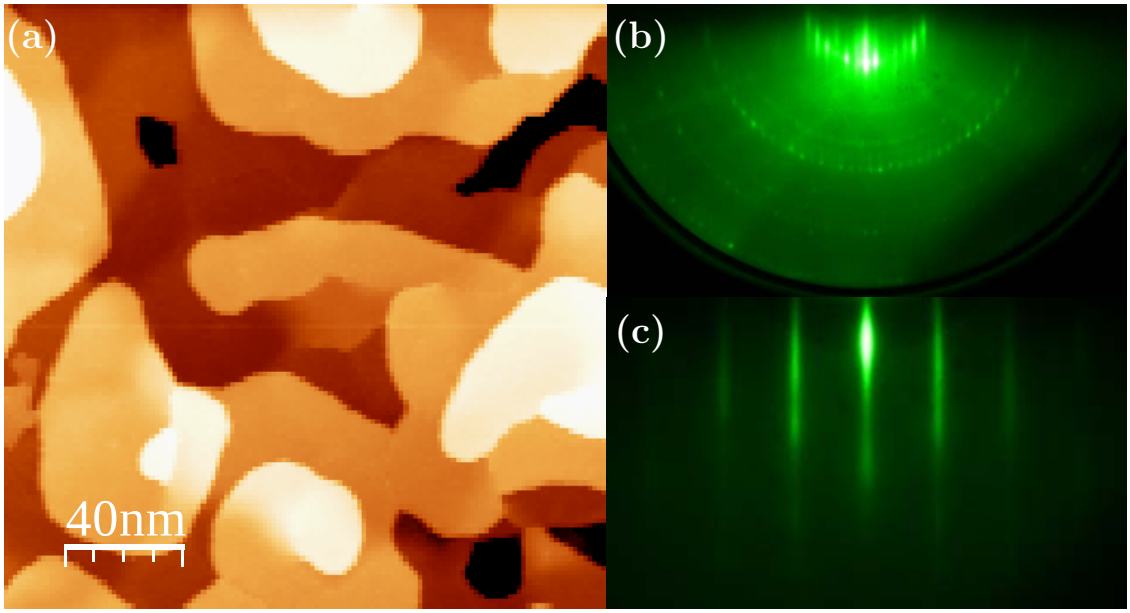

Figure 5.4: **RHEED and STM Images of CBST Thin Film.** (a) RHEED pattern of the ⟨111⟩ Nb-doped STO surface. (b) RHEED apptern of thin film after post-growth annealing. (c) 400x400nm STM topographic image of resulting CBST thin film.

5.2.3 Sample Characterization

Several *ex situ* measurements were made to determine the basic properties of the MBE grown CBST thin film. Once again, the chemical composition is determined using XPS. The background subtracted photo-emission peaks are shown in Fig. 5.5. Integration of the counts from these peaks yields $Cr_{0.12}(Bi_{0.07}Sb_{0.93})_{1.88}Te_{2.5}$ as the chemical formula for this sample. The Te deficiency is attributed to a combination of some vacancies and anti-site defects. The chemical potential should still be relatively low considering the results of Chap. 4, where low temperature annealing should result in good electronic properties.

XRD measurements are made to insure this composition is not the result of a different crystal phase. Additionally, XRR is used to determine the overall film thickness. Both XRD and XRR measurements were obtained using a Phillips X'pert XRD system with a Cu k-alpha X-ray source. Sample alignment was done by maximizing

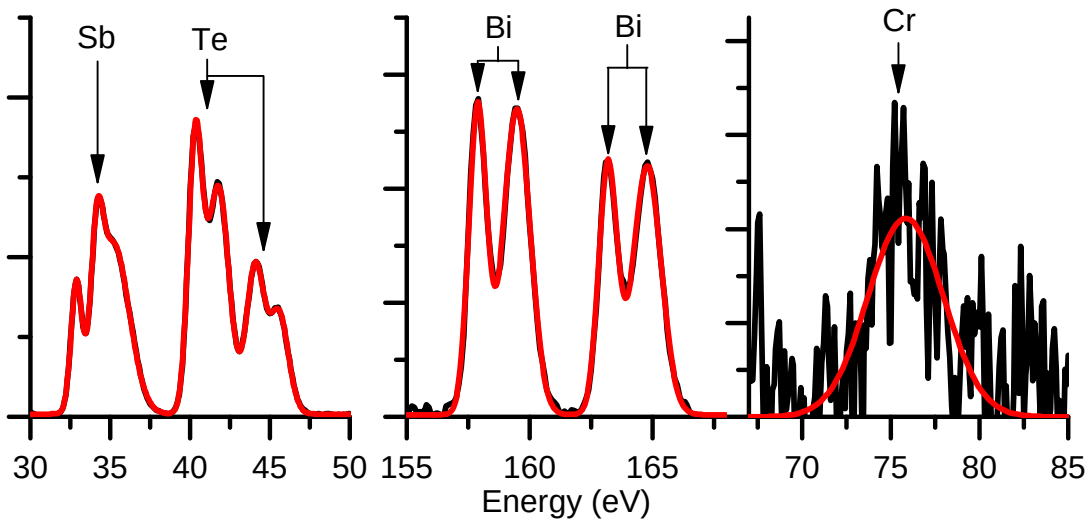

Figure 5.5: **Chemical Composition of CBST Film.** The background subtracted photoemission peaks (black) along with the Gaussian-Lorentzian product fit (red).

the intensity of the STO (111) reflection peak. Several 2θ-ω scans were obtained showing many very small peaks, which is the result of a low count rate from such a thin film, plus the STO (111) peak. These scans are shown in Fig. 5.6(b,c). The film peaks are all Bi_2Te_3/Sb_2Te_3 c-plane reflections; (003), (006), (009), (0015), (0018), and (0021). A 2θ-ω scan with higher resolution around the (0015) peak is shown in Fig. 5.6(c). Considering the quality of the RHEED pattern (Fig. 5.4(c)) and these XRD results, it is clear that the correct crystal phase is obtained. Additionally, a rocking curve, shown in Fig. 5.6(d), is also obtained while the detector is aligned with the BST (0015) reflection. Fitting a Lorentzian distribution yields a full width half maximum value of 0.13°. Therefore, the mosaicity of this film is very low, and can be considered epitaxial. Lastly, XRR is used to obtain the film thickness. Alignment is performed by maximizing the intensity of the second Kiessig fringe which is clearly seen in the low angle 2θ-ω scan, shown in Fig. 5.6(a). Using the locations of neighboring peak maxima, Eq. 2.21 gives the thickness of this film as approximately 10 nm.

Because the internal magnetic moment is the central property behind the the

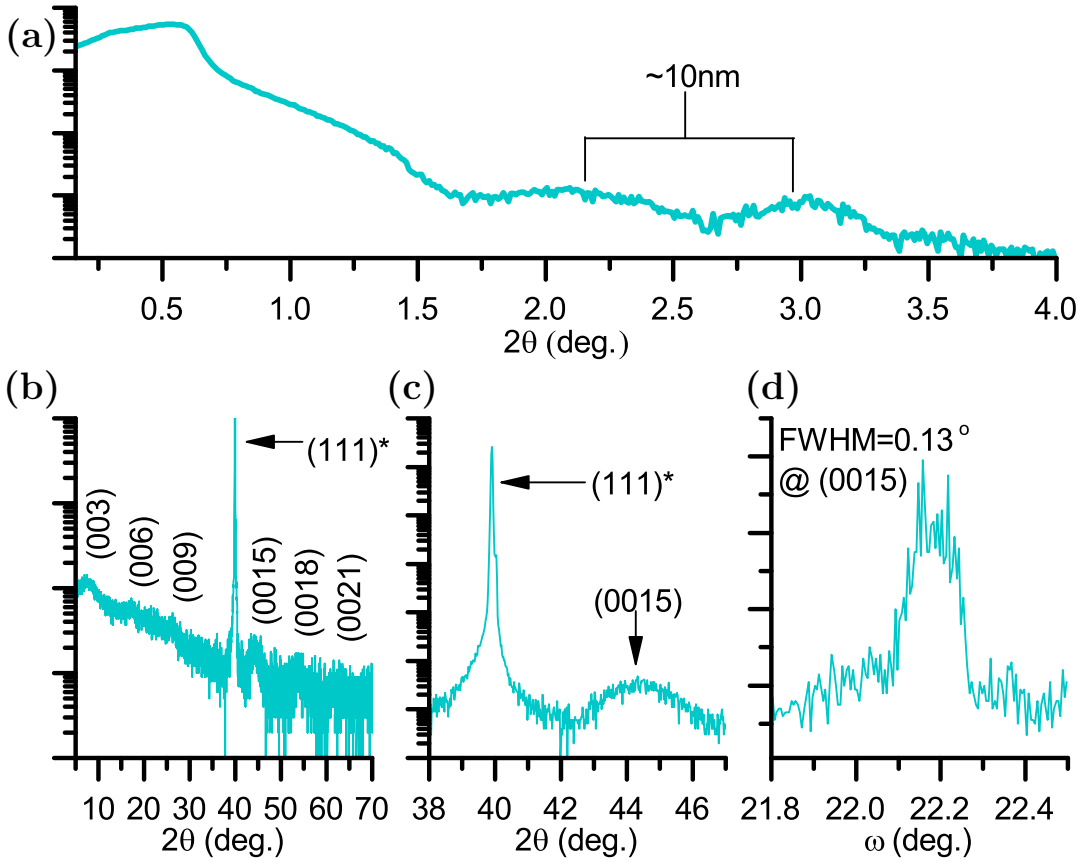

Figure 5.6: **X-Ray Diffraction Results for CBST Thin Film.** (a) XRR 2θ-ω scan with clear interference fringes. (b) XRD 2θ-ω scan about the STO (111) peak and the CBST (0015) peak. (c) rocking curve about the CBST (0015) peak.

QAHE, the magnetic properties of our CBST thin film must be verified. Superconducting quantum interference device measurements (SQUID) measurements indicate that the CBST sample is ferromagnetic. The instrument used was a Quantum Design MPMS system. The external field dependence of the DC moment was obtained at both 2.5K and 35K. These hysteresis curves are shown in Fig. 5.7. The residual moment and coercive field at 2.5K was 10^{-6} emu and 20 Oe, respectively. The hysteresis was much smaller at 35K, and vanished above this temperature suggesting this point is close to the Curie temperature.

All of these characterization measurements are important for verifying the results of the STM and STS measurements. The sample structure, magnetic order, and

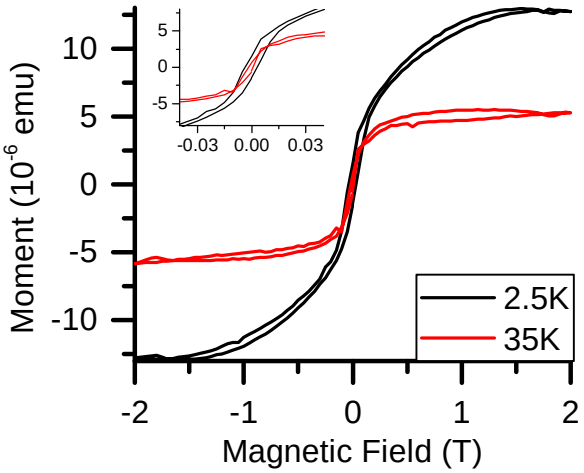

Figure 5.7: **Magnetic Hysteresis.** Magnetic moment vs. external magnetic field with diamagnetic background subtracted.

composition together are predictive of the TRS breaking that leads to the QAHE. The next step is to identify the existence of the massive Dirac gap.

5.3 Scanning Tunneling Microscopy and Spectroscopy

The CBST film was surveyed extensively including both large scale and atomic resolution topographic images. A large scale image revealing the overall morphology of the film is shown in Fig. 5.4(a). An atomic resolution image showing the Te terminated is shown in Fig. 5.8(a). The black triangular impurities in this image are the well known signature of Cr substitution. Counting these impurities and calculating their percentage yields 4% in a single plane of atoms, or $y = 0.08$. Considering the topographic image is a small sample area, this percentage is consistent with the result obtained by XPS. A spatially averaged dI/dV spectrum from this region, Fig. 5.8(b), reveals a significant gap in the surface states directly in the center of the bulk gap. The gap size is approximately 100 mV, which is significantly larger that previous

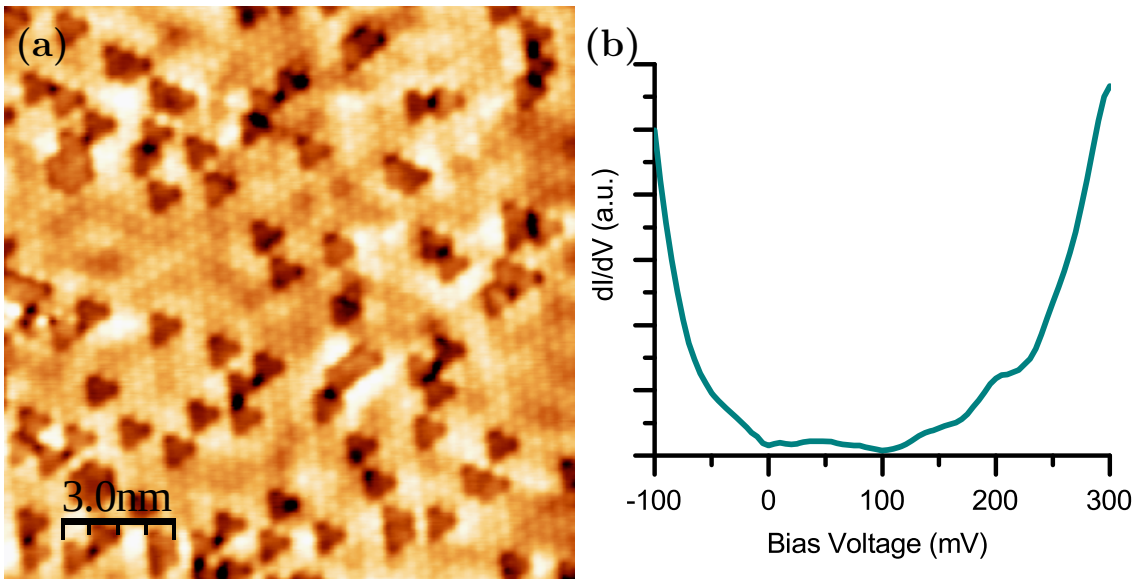

Figure 5.8: **STM Topography and Tunneling Conductance Spectrum.** (a) Atomic resolution image of the CBST surface. The black triangles are the Cr impurities. (b) Spatially averaged $\frac{dI}{dV}$ spectrum. The bottom and top of the massive Dirac gap appear to be at 0 mV and 100 mV respectively.

measurements, but is not unreasonable as the doping level of this film is larger.

Initial observations suggest the gap size is weakly variant in this region. To rigorously quantify the correlation to the Cr impurities, point dI/dV spectra are acquired over a 128×50 grid in the region of Fig. 5.8(a). The gap size at all points is calculated using an absolute dI/dV threshold value. Then, the Cr impurities are counted, and the density distribution is determined using a Gaussian kernel density estimation (KDE). The impurity positions are hand counted, and the density is calculated at each pixel by the KDE. The expression for the density value at each pixel, $\vec{r}$, is

$$\rho_{\text{impurity}}(x, y) = \sum_{r} \frac{1}{\sigma\sqrt{2\pi}} e^{-(\vec{r}-\vec{r^{i}})^2/2\sigma^2} \tag{5.1}$$

where $\vec{r}$ is the location in the image, $\vec{r^{i}}$ is the i^{th} impurity location, and σ is the Gaussian bandwidth. The value of σ is determined using the Sheather-Jones method for KDE bandwidth estimation [75]. This gap map and the Cr density map for a

subset of the region in Fig. 5.8(a) are shown in Fig. 5.9(b,c). To quantify the effect of Cr density on the gap size, a two dimensional Pearson correlation is used. The general formula is

$$C = \sum_{x,y} \frac{\rho_{\text{impurity}}(x,y) g(x,y)}{\sigma_\rho \sigma_g} \tag{5.2}$$

which is equal to 1 if the two images are perfectly correlated and -1 if they are perfectly anti-correlated. The correlation between Fig. 5.9(b) and Fig. 5.9(c) is $C = 0.11$. This is a weak positive correlation, but we can show that it is significant and represents a real relationship between the Cr density and the band gap.

Hypothesis testing for a Pearson correlation is straight forward. The test is whether or not the correlation is significantly different from the null hypothesis. In this case, the null hypothesis is $C = 0$, where no correlation exists between the Cr

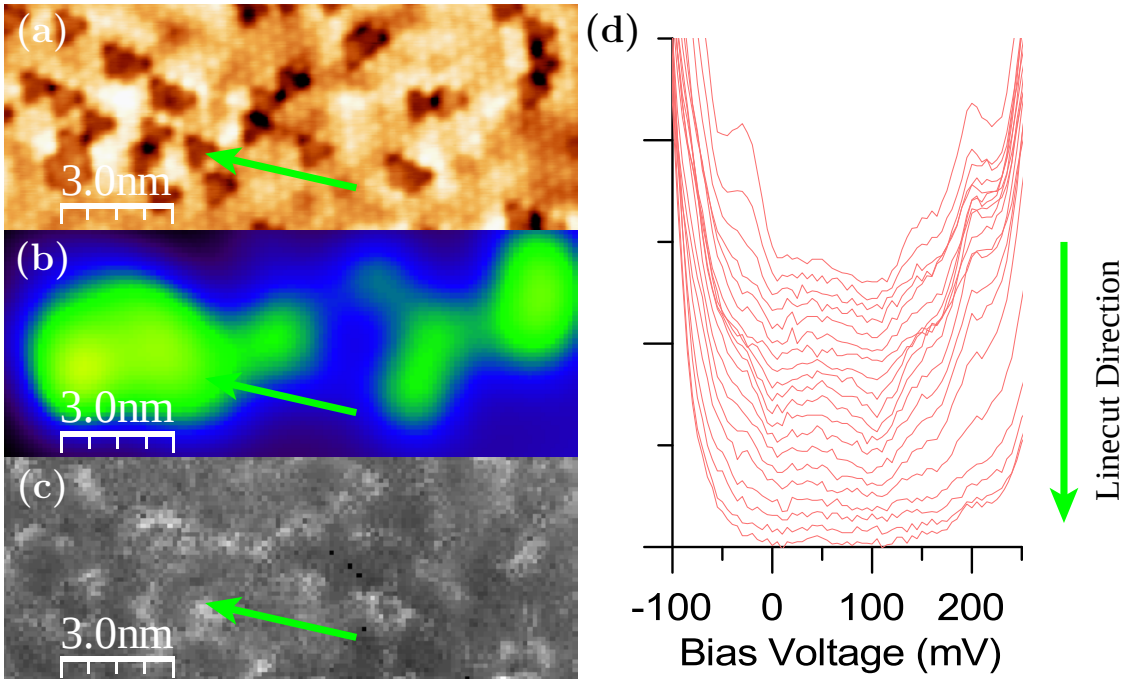

Figure 5.9: **Massive Dirac Gap Mapping without Cr Clusters.** (a) Topographic image of region with lower Cr impurities. (b) Cr density in the low-Cr region, calculated from Cr impurity positions using Gaussian kernel approximation. (c) Massive Dirac gap mapping in low-Cr region with green line indicating the path of the linecut of $\frac{dI}{dV}$ spectra. (d) Line-cut of $\frac{dI}{dV}$ spectra along direction indicated by arrow (green).

density and the gap size. To perform the test, a test statistic, or t-value, is calculate from the correlation, $C = 0.11$, and the degrees of freedom, which for Fig. 5.9(b,c) is $N - 2 = 128 \times 50 - 2 = 6398$. The formula for the t-value is

$$t = \frac{C\sqrt{\nu}}{1 - C^2} \tag{5.3}$$

where ν is the degrees of freedom (number of pixels). Now the p-value, calculated from the Student's t-distribution, is compared to the standard significance value, $p = 0.05$. This value means that there is a 5% probability that a correlation more extreme is obtained from another sampling of the data, given the null hypothesis is true. Therefore, a p-value lower than this means the null hypothesis can be rejected in favor of a model which indicates a real relationship between the correlated data. For the correlation associated with the region in Fig. 5.9(a), $p = 2.2 \times 10^{-42} < 0.05$. This means the relationship between the Cr density and the massive Dirac gap is real, and is not the result of sampling bias. The most significant point to be made from this result is that the correlation is weak in a region where the impurity density is fairly uniform. This is actually desirable because it indicates the size of the massive Dirac gap is consistent. With a small back-gating field, the chemical potential can be shifted into the gap and lie within everywhere.

However, the situation changes when the same measurements are done in a region that appears less homogeneous. One particular region of clustered Cr impurities was found to significantly affect the dI/dV spectra, and is shown in Fig. 5.10(a). The dI/dV spectra in this region appeared to have a different smaller gap-like structure form inside the massive Dirac gap. A line cut from a region of better homogeneity to the middle of the clustered region is shown in Fig. 5.10(d) to demonstrate this difference. Additional states are now appearing at 25 mV and at 100 mV. This should contribute to the overall electrical conductivity given a large enough frequency of

these regions, and the topographic surveys do indicate a significant number of these regions.

The same Pearson correlation is calculated between the Cr density and gap size, Fig. 5.10(b,c). For this region, the correlation is negative, $C = -0.43$. It is clear why this is the case. Consider the line-cut in Fig. 5.10(d). It shows the disintegration of gap from the states appearing at around 25 mV and 100 mV. The gap size calculation uses an absolute threshold of dI/dV for which the top/bottom of the gap is defined. In the middle of the clusters, the threshold defines the gap as the region between 50 and 100 mV, rather than from 0 to 100 mV. As a result, there is a sharp cutoff in gap size. Because this gap is significantly smaller in the higher density/in-homogeneous regions and much larger in the uniform region, the correlation must be negative. The significance of the correlation is calculated the same way as before. The test statistic is calculated, which gives a p-value so small it is rounded to zero. This indicates an even stronger relationship between the gap structure seen in the dI/dV curves and the Cr density in Fig. 5.10(b).

5.4 Conclusions

It is clear that the clustering of magnetic impurities significantly affects the massive Dirac gap in CBST thin films. The correlation between impurity density and gap size is weak in lower doping/uniform regions and strongly negative in high clustered regions. The gap-like structure forming in the regions of high Cr clustering definitely indicates a fundamentally different behavior. It is not obvious that the ferromagnetic ordering is suppressed in these regions because the magnetic hysteresis curves, Fig. 5.7, indicate that long range order is present. However, the CBST is a soft ferromagnet and the measurement is macroscopic, and thus is not sensitive to nanoscale variations.

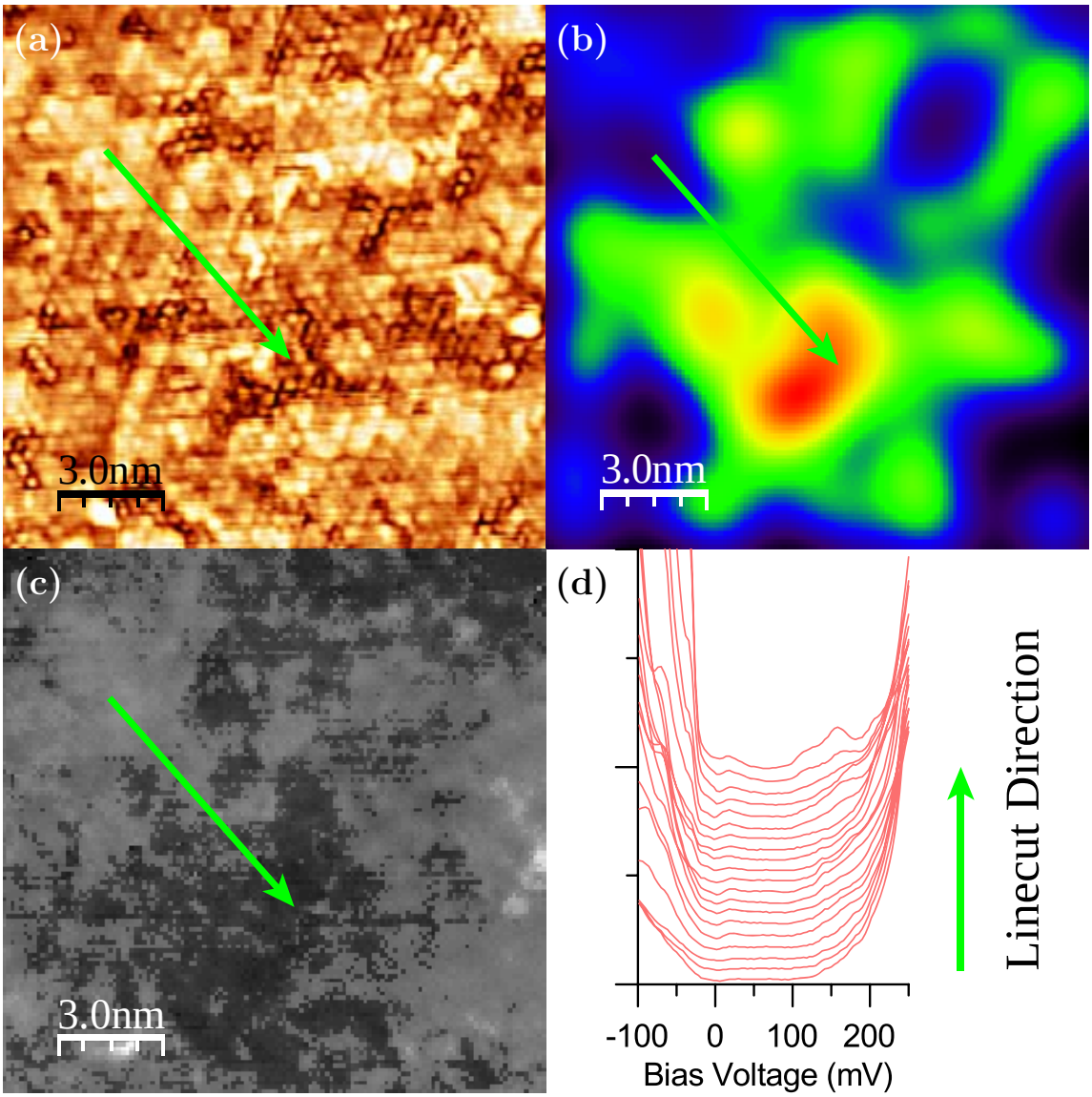

Figure 5.10: **Massive Dirac Gap Mapping with Cr Clusters.** (a) Topographic image of region with Cr clustering. (b) Cr density in the high-Cr region, calculated from Cr impurity positions using Gaussian kernel approximation. (c) Massive Dirac gap mapping in high-Cr region with green line indicating the path of the linecut of $\frac{dI}{dV}$ spectra. (d) Line-cut of $\frac{dI}{dV}$ spectra along direction indicated by arrow (green).

This significant degradation of the gap produces states at the Fermi level in many regions. These extra states contribute unwanted conductivity. Furthermore, thermal fluctuations can more easily excite electrons across the gap, which reduces the critical temperature required to isolate the quantized Hall conductance. Thus, the primary issue is the need to develop a growth condition that creates more uniform doping of Cr with higher doping levels to decrease the effect of thermal fluctuations. Previous studies state that lower substrate temperature during the film growth aids in making the doping more thermodynamically stable [29]. However, we found that using growth conditions with substrate temperatures as low as 170-180 °C resulted in suppressed adatom mobility causing formation of rough surfaces and lower crystallinity films. These defects are also likely to contribute unwanted free carriers in a non-uniform way. The quality seemed to improve though by decreasing the overall Cr content and keeping a slightly higher substrate temperature, ~ 200 °C. Although the large gaps may be more difficult to obtain with lower doping, it appears that impurities states arising in the gap are a much more detrimental.

All of these considerations are necessary for creating a robust quantum anomalous Hall insulator. The size of the band gap is the determining factor for the realization of device physics at high temperatures, as with any semiconductor material from Silicon to Gallium Nitride. More work should be done to improve the doping uniformity because the Fermi level, even with a gating field, will still cross bands which contribute unwanted conductivity and obscure the surface state conductance. Experiments have been done to find clever solutions such as the use of magnetic multi-layers, but this is still a work in progress [30]. Even the mechanism for the ferromagnetism is not agreed upon [76, 77]. This disagreement further complicates the situation, especially when one considers the various oxidation states of Chromium.

Chapter 6

Electron-Phonon Coupling in $Pb_{1-x}Sn_xSe$

The previous chapters focused on the application of STM/STS to TI thin film materials, and specifically to study symmetry-broken states. However, techniques used for these systems such as Landau level spectroscopy can reveal much more information about the surface band properties. Here, the focus is on the effect of electron-phonon coupling on the surface band dispersion. Instead of the $(Bi,Sb)_2(Se,Te)_3$ system, the unique surface states of $Pb_{1-x}Sn_xSe$ are studied. This is a material with specifically good thermo-electric properties and is part of a class of materials that (with appropriate band inversion) exhibit the topological crystalline insulator phase. The results of this chapter led to a publication in *Nature Communications* 6:6559 (2015).

6.1 Topological Crystalline Insulators

Other symmetries besides TRS have been applied to the classification of other topological phases [78, 79, 80, 81]. One in particular that has been predicted, and subsequently discovered, is the topological phase arising from point group symmetries known as the topological crystalline insulator (TCI) [78]. Crystals exhibiting four-fold rotational symmetry as well as time-reversal symmetric Hamiltonians, possess gapless surface states. These states arise from a topologically different band structure, but only on the $\langle 001 \rangle$ surfaces of C_4 symmetric crystals because surface interfaces inherently break rotational symmetry.

Similar to the 3D TIs, the TCI phase is defined by a Z_2 topological invariant, ν.

Gapless surface states exist for band structures with $\nu = 1$, as is the case with 3D TIs. The resulting surface bands contain four-fold degenerate points in momentum space, located at high-symmetry points at the edge of the Brillouin zone. This is particularly distinguished from 3D TIs, where the surface bands cross at the Γ point.

The TCI class is manifested by materials with band inversion and a crystal structure possessing this C_4 point group symmetry, otherwise known as mirror symmetry. It was predicted that SnTe and various related alloys are TCIs and have gapless surfaces states on their $\langle 001 \rangle$, $\langle 110 \rangle$, and $\langle 111 \rangle$ surfaces [82]. This was quickly verified with SnTe and the $Pb_{1-x}Sn_xSe$ alloy for $x_c = 0.23$ [83, 84]. These "lead-salts" and related crystals have been studied for several decades, and previous knowledge about their band gap inversions and their exceptional thermo-electric properties has already been developed.

The electronic properties of TCIs are similar to 3D TIs in that they are naturally conducting despite having a band gap. SnTe, for example, has a tendency to be heavily p-type carrier doped owing to its Sn vacancies. The result is that the topologically protected surface bands are unoccupied states. This poses the exact same problem that has previously been delt with in BST. However, being p-type doped adds an additional problem for ARPES, which is a probe that requires electrons to occupy the bands. Therefore, ARPES cannot probe the four-fold degeneracy at the edge of the Brillioun zone very easily, if at all.

Although, using crystals grown with very high quality allows for measurement of the surface band dispersion, alloys have generated more success [83, 84]. $Pb_{1-x}Sn_xSe$ is carrier-tunable with Sn concentration, similar to BST. Because of this it is the most popular compound to study. The relationship between the surface states and the thermo-electric properties in $Pb_{1-x}Sn_xSe$ is particularly interesting. The effect of surface phonons on the metallic surface states has been studied in Bi_2Se_3 [85]. This brings us to the focus of this experiment and the electron-phonon interaction, which

is an interaction that can contribute significantly to the surface band dispersion and thermo-electric properties.

6.2 The Electron-Phonon Interaction

Vibrations of the atomic nuclei in a crystal lattice produce quasi-particles called phonons, which facilitate the energy exchange between lattice sites as a result of these vibrations. The distortion caused by these vibrations to the periodic potential seen by the electrons ultimately affects the electronic states. For simple metals, the effect of this coupling is a reduction of the group velocity at the Fermi surface given by

$$v(k) = \frac{1}{\hbar}\frac{\partial \epsilon(k)}{\partial k} = \frac{1}{1+\lambda} v^o(k) \tag{6.1}$$

where λ is known as the mass enhancement factor. In other words, we have an effective mass given by $m^* = (1+\lambda)m_e$. Fig. 6.1 shows the effect on the dispersion.

From a fundamental perspective, the electron-phonon coupling (EPC) is governed by the product, $\alpha^2(\omega)F(\omega)$, where $\alpha(\omega)$ is the effective EPC at phonon frequency ω and $F(\omega)$ is the phonon DOS. $\alpha^2(\omega)F(\omega)$ (denoted $\alpha^2F(\omega)$) is called the Eliashberg function, which is a spectral density function that can be interpreted as the scattering probability of an electron by a phonon at an energy ω. Its contribution to the electronic states is realized in the electron self-energy which is a complex value, $\Sigma = \Re\{\Sigma\} + i\Im\{\Sigma\}$. The real part of the electron self-energy is calculated directly by the Fredholm type integral

$$\Re\{\Sigma\} = \int_0^\infty d\omega \alpha^2 F(\omega) K\left[\frac{E}{kT}, \frac{\omega}{kT}\right] \tag{6.2}$$

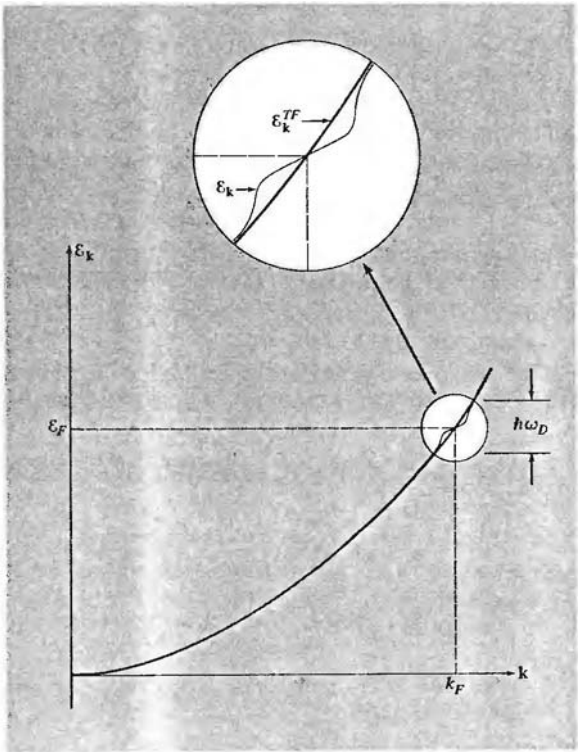

Figure 6.1: **Phonon Effect on Free Electron Dispersion.** The electron-phonon interaction cause a kink in the dispersion that is measureable and determined by Eq. 6.2 (Ashcroft and Mermin).

where $K[y, y']$ is a kernel function defined by

$$K[y, y'] = \int_{-\infty}^{\infty} dx \frac{f(x-y)2y'}{(x^2 - y^2)} \tag{6.3}$$

and $f(x)$ is the Fermi distribution function. The imaginary part represents the quasi-particle lifetime, and it is easily obtained from the real part through the Kramers-Kronig relations. Finally, a known $\alpha^2F(\omega)$ gives the mass enhancement factor directly by

$$\lambda = 2\int_0^{\infty} d\omega \frac{\alpha^2F(\omega)}{\omega} \tag{6.4}$$

This information and the prominent modes from $\alpha^2F(\omega)$ provide a comprehensive picture of the effect of EPC on the electronic properties.

Previously, $\alpha^2F(\omega)$ has been estimated using the second derivative of the tunneling

conductance, $\frac{d^2I}{d^2V}$, and λ from the derivative of the dispersion at the Fermi level. However, $\Re\{\Sigma\}$ is an observable quantity and Eq. 6.2 is invertable. To obtain $\alpha^2F(\omega)$ and λ from the $Pb_{1-x}Sn_xSe$ surface states, the real part of the self-energy is extracted from the dispersion. Once $\Re\{\Sigma\}$ is obtained, the kernel function, Eq. 6.3, is calculated, and the integral in Eq. 6.2 is inverted yielding $\alpha^2F(\omega)$. In this experiment, the surface band dispersion of $Pb_{1-x}Sn_xSe$ is obtained from Landau level spectroscopy.

6.3 Scanning Tunneling Spectroscopy and Landau Level Dispersion

Bulk $Pb_{1-x}Sn_xSe$ single crystals were grown using the self-selecting vapor method, with $x \approx 0.09$. This sample is below the topological transition, and thus is a trivial bulk insulator. However, it stills maintains its distinct surface bands, which will produce Landau levels. After transferring to the STM vacuum system, the single crystals are cleaved at 77K exposing an atomically flat $\langle 001 \rangle$ surface. Immediately after the cleaving process, the sample is inserted into a low temperature STM. All measurements were performed at a temperature of 4K.

STM topographic images and dI/dV spectra were obtained. A typical atomic resolution topographic image is shown in Fig. 6.2(a), demonstrating the presence of impurities on the $\langle 001 \rangle$ surface. The crystal defects consist of point defects, which in $Pb_{1-x}Sn_xSe$ typically raise the Fermi into the conduction band. This region's respective spatially averaged dI/dV curve is shown in Fig. 6.2(b), indicating a bulk band gap of approximately 50 mV. The dI/dV curve indicates that the Fermi level does lie in the conduction band as expected.

A high magnetic field is applied perpendicular to the sample surface, and Landau levels are clearly observed. Line-cuts of dI/dV spectra were obtained with various

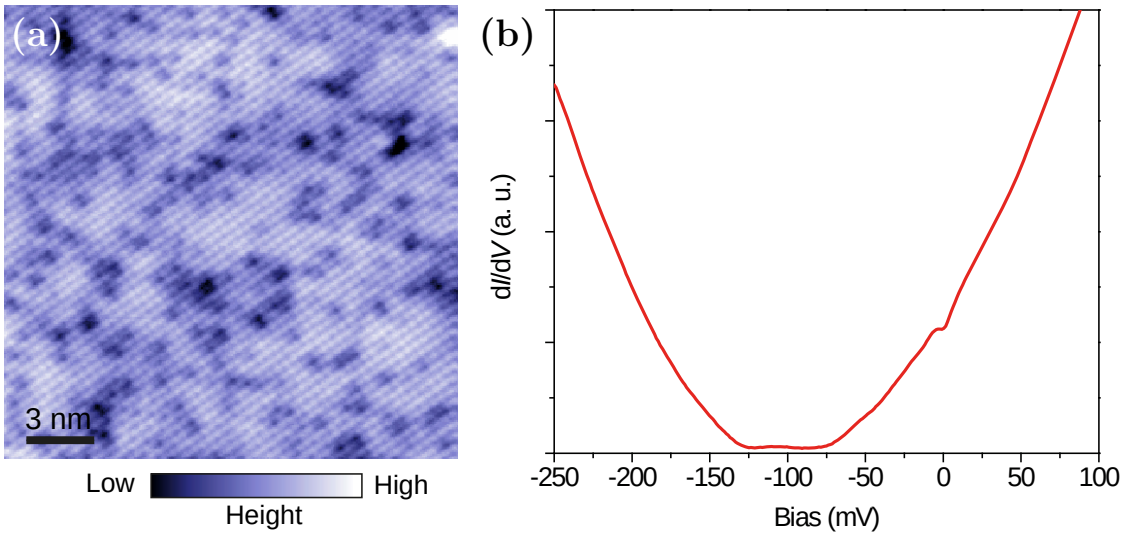

Figure 6.2: **Topographic Image and Tunneling Conductance of $Pb_{1-x}Sn_xSe$.** (a) 20×20 nm STM topographic image of $Pb_{1-x}Sn_xSe$ $\langle 001 \rangle$ surface. (b) Typical $\frac{dI}{dV}$ spectrum indicating the band gap and Fermi level in the conduction band.

magnetic field strengths, 6.1-7.5T, as well as the 0T background spectrum. The Landau level peaks disperse as expected. Once the 0T background is subtracted, the peaks are fit to Lorentzian curves, and the peak energies are related to their respective radially averaged wave-vector states by Eq. 3.10. Plots of these spectra and the calculated dispersion are shown in the Fig. 6.3. In the dispersion, Fig. 6.3(c), a "kink" near the Fermi energy is apparent which is indicative of the band renormalization that occurs from the EPC. This kink in the dispersion is the contribution of the real part of the electron self-energy, and it encodes all the information needed to extract the Eliashberg function.

To obtain the real part of the electron self-energy, $\Re\{\Sigma\}$, the non-interacting quasi-particle dispersion, or bare-particle dispersion, must be subtracted from the experimentally obtained dispersion. One method to obtain the bare-particle dispersion is to fit a polynomial function to the points far away from the Fermi level. Alternatively, the dispersion can be obtained by iteratively determining the optimal polynomial based on the properties of the self-energy, namely the anti-symmetry and

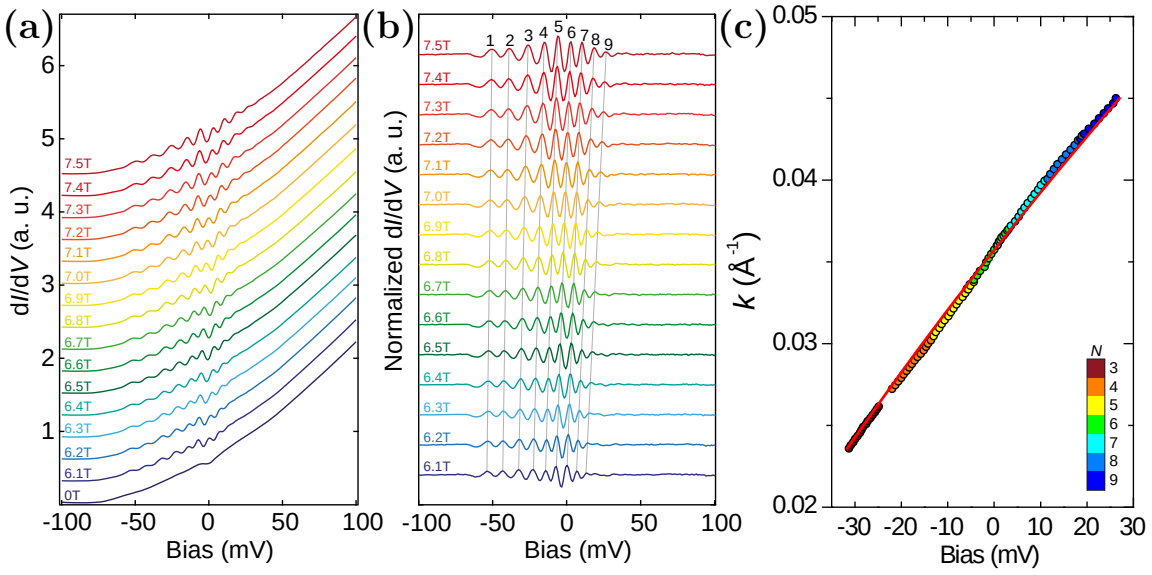

Figure 6.3: **Landau Level Spectroscopy of $Pb_{1-x}Sn_xSe$.** (a) $\frac{dI}{dV}$ spectra taken in various magnetic fields from 0T to 7.5T. (b) $\frac{dI}{dV}$ spectra with backgrounded subtratced and normalized. (c) Calculated dispersion from the LL peaks with the bare particle dispersion (red) superimposed.

convergence to zero. Lastly, a first-principles calculation can give a numerical result for the bare quasi-particle dispersion without EPC.

The bare-particle dispersion in Fig. 6.3(c) is calculated using a first-principles calculation. A tight-binding model was used to approximate the dispersion for $Pb_{0.91}Sn_{0.09}Se$. The dispersion was approximately linear with a minorly significant quadratic component given in the form of

$$E_0(k) - E_F = \alpha(k - k_F) + \beta(k - k_F)^2 \tag{6.5}$$

where k is the electron wave vector and k_F is the wave vector where $E(k_F) = E_F$. The parameters for the dispersion were $\alpha = 2.64\,\text{eV}\,\text{Å}^{-1}$, $\beta = 14.24\,\text{eV}\,\text{Å}^{-2}$, and $k_F = 0.036\,\text{Å}^{-1}$. The real self energy is then given by

$$\Re\{\Sigma\} = E(k) - E_0(k) \tag{6.6}$$

where $E(k)$ is the experimentally obtained dispersion. Now using $\Re\{\Sigma\}$, the integral in Eq. 6.2 can be inverted because the kernel function, Eq. 6.3, is known by definition.

6.4 Extracting the Eliashberg function from Electron Self-Energy

The naïve approach to obtain $\alpha^2F(\omega)$ is to discretize the kernel integration to a matrix operation

$$\overrightarrow{\Re\{\Sigma\}} = \hat{K}\overrightarrow{\alpha^2F(\omega)} \tag{6.7}$$

and perform a least-squares approximation to obtain $\alpha^2F(\omega)$. However, least-squares makes no assumptions about the general form of the solution. Consequently, this produces unphysical results. Another calculation employing the Maximum Entropy Method (MEM) has previously been developed for inverting exactly the integral in Eq. 6.2, and it was shown to be reliable in extracting $\alpha^2F(\omega)$ from dispersions acquired by ARPES measurements [86]. The MEM program developed for this was modified to utilize the Landau level dispersions obtained in the previous section. The source code and the changes made to the MEM program are discussed in App. B.

6.4.1 Maximum Entropy Method

The fundamental principle of the MEM routine is that, rather than minimizing χ^2 (the result of the least-squares solution), you can alternatively maximize the function

$$L = aS - \frac{\chi^2}{2} \tag{6.8}$$

where χ^2 is the usual sum of the square residuals, a is a tuning parameter, and S is the Shannon-Jaynes entropy given by

$$S = \int_0^\infty d\omega \left[\alpha^2 F(\omega) - m(\omega) - \alpha^2 F(\omega) \ln \frac{\alpha^2 F(\omega)}{m(\omega)}\right] \tag{6.9}$$

where $m(\omega)$ is a constraint function. This method has an advantage by encoding the basic properties of $\alpha^2 F(\omega)$ (i.e. properties of a spectral density function), into $m(\omega)$. Also, L is guaranteed to have only a single global maximum. As a matter of fact, we will see that this is precisely the case because the starting constraint function has little effect on the final solution. Consequently, the MEM routine will inherently convergent to a physical result; assuming high quality data and a reasonable $m(\omega)$.

The MEM routine is a self-consistent calculation. $\alpha^2 F(\omega)$ is assumed for the starting function. Specifically, the constraint function is chosen as a starting point, so $\alpha^2 F(\omega) = m(\omega)$. Then, the real self-energy is calculated from Eq. 6.2. This real-self energy fit and the experimental data for $\Re\{\Sigma\}$ are used to calculate χ^2, S, and thus L. L is differentiated with respect to $\alpha^2 F(\omega)$, and the maximizing slope of this function (i.e. how it tends toward its global maximum) is used to obtain a correction to $\alpha^2 F(\omega)$. The process is then repeated until these corrections are negligible.

6.4.2 Convergence and Robustness

A couple of hyper-parameters need to be tuned for this routine. The first is the parameter a, in Eq. 6.8, and the second is the constraint function, $m(\omega)$. Generally, it is acceptable to use the value of χ^2 to decide these parameters. The various orders of magnitude of a are used to fit the experimental data, and the $\alpha^2 F(\omega)$ resulting from these fits are shown in Fig. 6.4(a). While a does have an effect on $\alpha^2 F(\omega)$, it is clear that the position of the peaks, the most relevant feature of the function, remain unchanged for values below $a = 10$. Therefore, the choice of a need only be accurate to

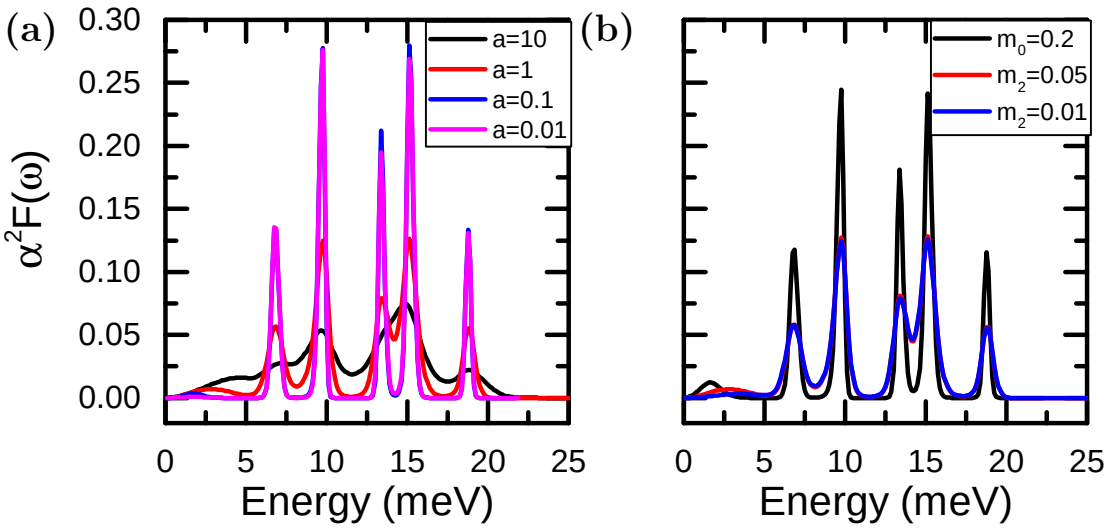

Figure 6.4: **MEM Convergence Tests.** (a) $\alpha^2F(\omega)$ obtained from the convergence tests for the maximization paramter, a. (b) $\alpha^2F(\omega)$ obtained from the convergence tests for m_o, the value of the constant term in the constrint function $m(\omega)$.

a certain degree, and the fit is robust against mild variations. Consequently, $a = 1.0$ was chosen as it produced the best χ^2 without overfitting the data.

Convergence calculations were also performed with varying constraint functions. The basic form of $m(\omega)$ is similar to the previous study, and encodes the basic properties of a spectral density function [86]. Specifically, the piecewise function used is

$$m(\omega) = \begin{cases} m_o\left(\frac{\omega}{\omega_D}\right) & \omega_D > \omega > 0 \\ m_o & \omega_M > \omega > \omega_D \\ 0 & \omega > \omega_M \end{cases} \tag{6.10}$$

where ω_D is used to ensure convergence to zero, ω_M is the maximum phonon frequency, and m_0 is the plateau of the constraint function. ω_M is easily determined by approximating the energy at which $\Re\{\Sigma\}$ converges to zero. ω_D exists merely to suppress the low frequency artifacts. m_0 is the main tuning parameter for the constraint function. In Fig. 6.4(b), $\alpha^2F(\omega)$ is plotted for various values of m_0. Once again, the qualitative features remain consistent. The optimal constraint function

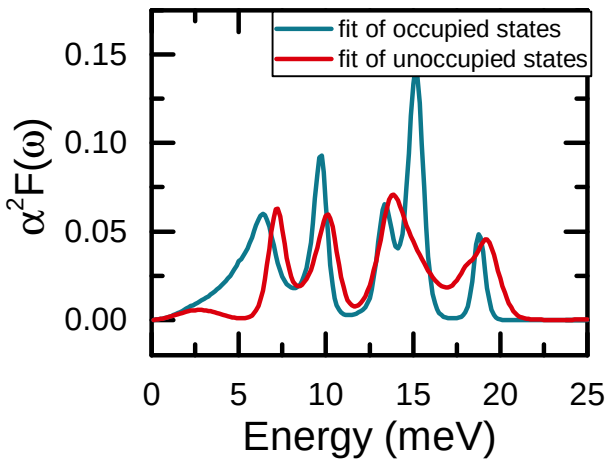

Figure 6.5: **Eliashberg Function from Occupied/Unoccupied Sates.** Eliashberg function obtained from using only the occupied states data and only the unoccupied states data.

which produced the best fit to the experimental data was $m_0 = 0.05$.

Because STS is uniquely able to measure the unoccupied states in the system, much more information can be leveraged for the MEM routine. However, it is now prudent to check that the results are consistently obtained for both the occupied and unoccupied states (i.e. anti-symmetry holds). This is the first time this MEM routine has been applied to STS data rather than ARPES, which further motivates the consistency check. Fig. 6.5 shows the result of these two calculations using the optimal parameters found in the previous convergence tests. The $\alpha^2F(\omega)$ obtained for each subset of the data are marginally different. That is expected as the noise levels are not the same. Qualitatively, the dominant peaks are consistent.

6.4.3 MEM Results

Both the real self-energy, $\Re\{\Sigma\}$, and the Eliashberg function, $\alpha^2F(\omega)$, were calculated using the previously determined optimal hyper-parameters. The results are shown in Fig. 6.6. These results visually confirm the goodness of the fit. The results also clearly show the correspondence of the peaks in $\alpha^2F(\omega)$ with the features in $\Re\{\Sigma\}$,

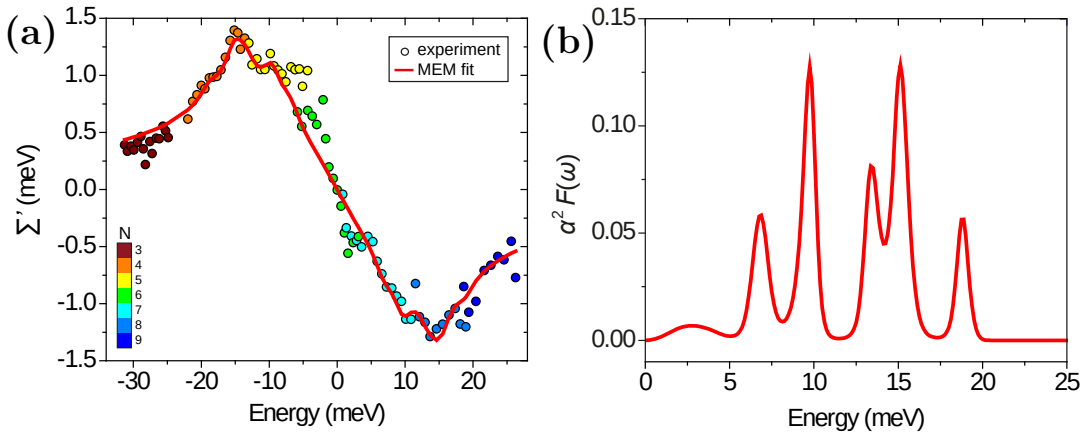

Figure 6.6: **MEM Results.** (a) Real-self energy obtained from experiment and fit (red) after calculating Eliashberg function from the MEM routine. (b) Resulting Eliashberg function obtained from MEM routine using optimal parameters.

Experimental Eliashberg modes	7.0	9.8	13.3	15.2	18.9
Calculated bulk modes	5.6	10.2	14.0	15.8	17.8

Table 6.1: **Phonon Modes.** A comparison of the primary modes in $\alpha^2F(\omega)$ and the dominant modes in the phonon DOS.

and thus demonstrate the effect that the EPC has on the band renormalization. The Eliashberg function in Fig. 6.6(b) yielded a mass enhancement of $\lambda = 0.11 \pm 0.05$. The most remarkable result of this experiment is the precision at which the identified modes correlate with the primary phonon DOS modes. A comparison of the primary modes in $\alpha^2F(\omega)$ to that of the bulk phonon DOS, $F(\omega)$, is shown in Table 6.1. The MEM routine was able to extract $\alpha^2F(\omega)$ from high enough quality data, and then identify every significant mode. Obviously, they are not the same because of the EPC function, $\alpha(\omega)$.

There are two main consequences of this agreement. First, the value of λ is consistent with low temperature measurements on similar systems. Second, the resolution and accuracy obtained with this method demonstrates the unique ability of STS to obtain EPC information at the nanoscale. This is specifically beneficial for two-dimensional systems and topological materials with surface states being affected

by EPC. Several future experiments can be done including, but not limited to, the nanoscale variations of λ and the correlation to impurity states. Furthermore, this measurement should also be performed on $Pb_{1-x}Sn_xSe$ with x above the topololgical transistion to identify the EPC effect on Dirac fermions. The information obtained from the Eliashberg function provides a tremendous insight into the EPC, especially considering the evidence of Dirac Fermion interactions with lattice excitations [85].

Chapter 7

Final Thoughts

Classifying band structures topologically is so profound not only in scientific understanding but also in a technological sense. The distinction between topological phases is so subtle that all of these materials have been studied for decades and yet their unique surface bands were only discovered several years ago. It reminds us that it is always possible to find new physics in what otherwise would be considered well understood solid materials. Furthermore, the idea behind the charge transfer mechanism in the QHE and QAHE motivates the pursuit to manipulate quantum states themselves rather than the electronic occupation of those states for device operation. The ability to manipulate topological states with symmetry breaking fields, such as magnetic and electric fields, adds another controlling parameter that can determine the state of matter. The experiments covered here were an attempt to uncover the difficulties in realizing the existence of these new states. High performance techniques were used to probe the surface bands of BST and CBST. These thin films are extremely difficult to fabricate with high quality and is likely the crux of the problem. Although, other fundamental properties could be contributory. As for the surface electron state coupling to phonons in $Pb_{1-x}Sn_xSe$, it is quite amazing that the Eliashberg function can be extracted in such a robust way, given enough *a priori* knowledge is utilized.

On one final note, I began work on these projects by designing and constructing the molecular beam epitaxy system used for fabricating the thin films discussed here. It is the first to ever be employed by our research group to study thin films using low temperature scanning tunneling microscopy. Concurrently, I performed the analysis

leading to the primary results of the experiment documented in Chapter 6. The results of Chapter 6 subsequently led to a publication in *Nature Communications* 6:6559 (2015). The experiments and results in Chapters 4 and 5 are being prepared for submission to peer reviewed journals at the time of writing this dissertation. However, the more meaningful consequence from all of these experiments is the permanent establishment of thin film research in our group that was initiated by these projects.

Appendix A

Effusion Rate Uniformity from a Knudsen Cell

Calculating the flux distribution for a tilted K-cell is more complicated because the differential unit surface area is now $dS\cos(\theta+\phi)$, and r_p is a function of both θ and ϕ. For the center point of the substrate, it is easy to calculate. Eq. 2.10 simply becomes

$$\frac{F_o\cos\phi}{\pi r_c^2} \tag{A.1}$$

and Eq. 2.11 is

$$\frac{F_o\cos\theta\cos(\theta+\phi)}{\pi r_p(\theta,\phi)^2} \tag{A.2}$$

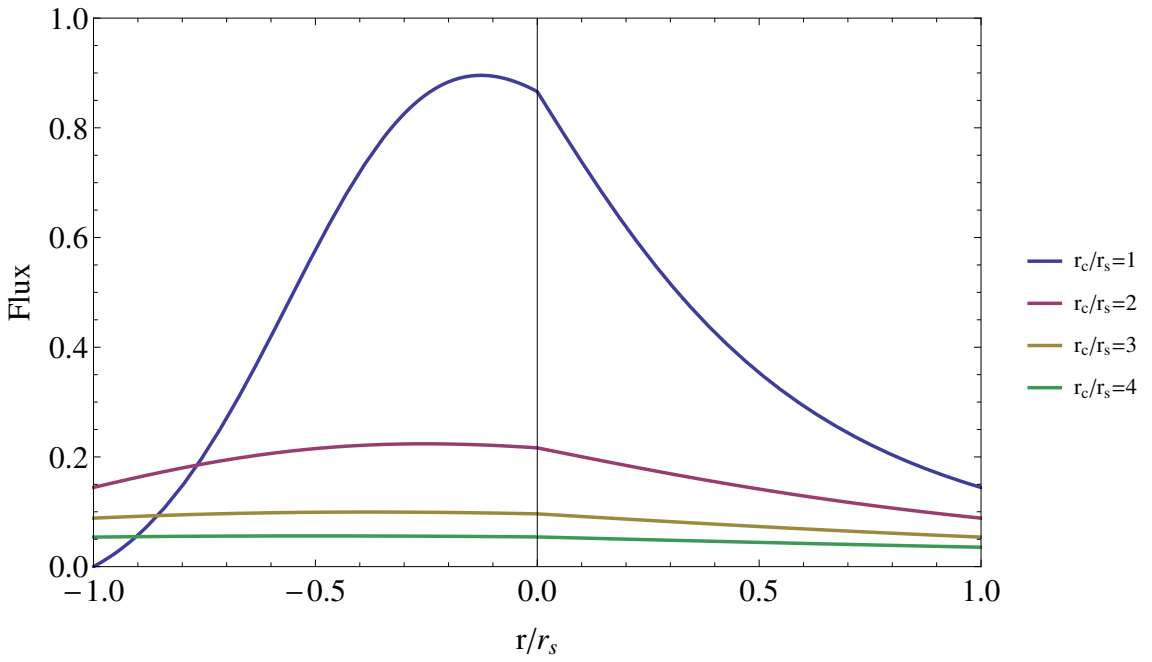

Figure A.1: **Flux Distribution.** Effusion flux, $\frac{dF}{dS}$ as a function of r/r_s (see Fig. 2.1), for $\frac{r_c}{r_s}=1,2,3,4$, $F_o=\pi$, and a tilt angle of $\frac{\pi}{6}$.

If we express Eq. A.2 as a function of r_s (see Fig. 2.1), we can calculate the reasonable ratios of r_s/r_c for flux uniformity with a given substrate size. First, the constraining function $\theta(r_s, \phi)$ is needed. The law of cosines will provide a relation between r_p and r_s. This gives

$$r_p^2 = r_s^2 + r_c^2 - 2r_s r_c \cos(\phi + \frac{\pi}{2}) \tag{A.3}$$

which reduces to

$$r_p^2 = r_s^2 + r_c^2 + 2r_s r_c \sin\phi \tag{A.4}$$

The law of cosines can be used again to obtain the constraining function $\theta(r_s, \phi)$. This time we have

$$r_s^2 = r_p^2 + r_c^2 - 2r_p r_c \cos\theta \tag{A.5}$$

$$r_s^2 = (r_s^2 + r_c^2 + 2r_s r_c \sin\phi) + r_c^2 - 2\sqrt{r_s^2 + r_c^2 + 2r_s r_c \sin\phi} r_c \cos\theta \tag{A.6}$$

$$0 = r_c + r_s \sin\phi - \sqrt{r_s^2 + r_c^2 + 2r_s r_c \sin\phi}\cos\theta \tag{A.7}$$

$$\cos\theta = \frac{r_c + r_s \sin\phi}{\sqrt{r_s^2 + r_c^2 + 2r_s r_c \sin\phi}} \tag{A.8}$$

Using Eqs. A.4 and A.8, Eq. A.2 can be expressed as

$$\frac{dF}{dS} = \frac{F_o \cos[\theta(r_s, \phi)] \cos[\theta(r_s, \phi) + \phi]}{\pi(r_s^2 + r_c^2 + 2r_s r_c \sin\phi)} \tag{A.9}$$

where the constraint function for θ is

$$\theta(r_s, \phi) = \arccos\left[\frac{r_c + r_s \sin\phi}{\sqrt{r_s^2 + r_c^2 + 2r_s r_c \sin\phi}}\right] \tag{A.10}$$

which is a function of only r_p and ϕ. Plots of the flux distribution along this profile for various values of r_c are shown in Fig. A.1. It is apparent from Fig. A.1 that larger $\frac{r_c}{r_p}$ values is more desirable because the flux is more uniform over the substrate surface. The overall total rate is lower, but this is an unimportant trade off.

Appendix B

Modified Maximum Entropy Method Routine

The program used to invert the integral in Eq. 6.2 is called `MEM_ELIASHBERG`. It is a modified version of the program authored by the Shi *et al* in Ref. [86], and was used to produce the results in Chap. 6. The Fortran77 source code is contained in three files, `MEM_inc.f`, `MEM3_Main.f`, and `MEM_ALG.f`. The input data is defined in a configuration file named `CONF3.INI`. The program is hard-coded to read the input parameters from this file.

There are two main improvements to the program that facilitate a more general use of the code for both ARPES and STM data. First, the options for errors determination were expanded. In addition to automatic errors calculation, user provided errors can be read in from a file. Furthermore, an errors only calculation can be done where the program exits premuturely without performing the fit and writing the errors to a file. The other major improvement is the added ability to use certain energy states of the input dispersion, namely all states, only occupied states, and only unoccupied states.

Shown below is the configuration file with all the input parameters along with the source code files. The modified portions of the code are shaded in light gray as well as the additional parameters in `CONF3.INI`.

`CONF3.INI`

```
1  PbSnSeDispersion.txt  DATA FILE NAME
2  NONE   MODEL DATA FILE
3  PbSnSe  OUTPRX
4  94  NDRAW: NUMBER OF DATA POINTS OF THE DISPERSION
```

```
200  NA: MUNBER OF POINTS THE ELIASHBERG FUNCTION SHOULD TAKE
0.05  ECUTOFF: THE POSITION OF FERMI ENERGY
2  STATES (0: ALL 1: OCCUPIED 2: UNOCCUPIED)
4.5  KT: TEMPERATURE IN K
0  FITBPD
1.57  A1
4.54  A2
0.0  EF
0.0633  KF
2  ERRCALC: ROUTINE FOR ERRORS (0: CALC-FIT 1: CALC 2: READ-FIT)
-1  ERRB0
0.018  ERRB1
PbSnSe_ERR.dat  ERROR FILE NAME
2  METHOD
1000  ITERNUM
100  ALPHA
0.02  DALPHA
43  XCHI
5E-3  OMEGAD
25E-3  OMEGAM
0.05  LAMBDA0
-1.0  BETA
4  NBIN
0
35
50
68
90
```

MEM3_Main.f

```
C     ************************************************************
C     This program takes the quasiparticle dispersion as input
C     ************************************************************

      PROGRAM MEM2_ELIASHBERG
      IMPLICIT NONE
      INCLUDE 'MEM_inc.f'
      INTEGER NDRAW, ND, NA
      DOUBLE PRECISION Y(NMAX), D(NMAX), SIGMA(NMAX), KERN(NMAX, NMAX)
      DOUBLE PRECISION A(NMAX), M(NMAX), Y1(NMAX), EM(NMAX, NMAX)
```

```
11        DOUBLE PRECISION ERAW(NMAX), KRAW(NMAX), K(NMAX)
12        CHARACTER*32 DATAIN, ERRFILE, MODEL, OUTPRX, FILENAME
13        DOUBLE PRECISION KT, ECUTOFF, A1, A2, DA1, DA2, KF, EF, E0
14        INTEGER METHOD, ITERNUM, NBIN, FITBPD, ERRCALC, STATES
15        DOUBLE PRECISION OMEGAD, OMEGAM, LAMBDA0
16        DOUBLE PRECISION YMIN, YMAX, DY1, OMEGABIN(NMAX), BETA
17        DOUBLE PRECISION ALPHA, DA, DALPHA, ERRB0, ERRB1
18        DOUBLE PRECISION LAMBDA, DLAMBDA, OMEGALOG
19        DOUBLE PRECISION EBX(NMAX), EBY(NMAX), EBDX(NMAX), EBDY(NMAX),
20       $     D1(NMAX)
21        DOUBLE PRECISION CHI, XCHI, CHI0, Q, S, IMS, IMSIGMA
22        INTEGER I, J, LOUTPRX
23        DOUBLE PRECISION X1, X2, X12, S1, S2, XX
24
25
26        OPEN(10, FILE = 'CONF3.INI')
27
28        READ(10, *) DATAIN
29        READ(10, *) MODEL
30        READ(10, *) OUTPRX
31
32  C     * DATA PARAMETERS *
33        READ(10, *) NDRAW
34        READ(10, *) NA
35        READ(10, *) ECUTOFF
36        READ(10, *) STATES
37        READ(10, *) KT
38
39  C     * RAW DATA CORRECTION PARAMETERS *
40        READ(10, *) FITBPD
41        READ(10, *) A1
42        READ(10, *) A2
43        READ(10, *) EF
44        READ(10, *) KF
45
46  C     * ERROR BARS *
47        READ(10, *) ERRCALC
48        READ(10, *) ERRB0
49        READ(10, *) ERRB1
50        READ(10, *) ERRFILE
51
```

```
C      * FITTING PARAMETERS *
       READ(10, *) METHOD
       READ(10, *) ITERNUM
       READ(10, *) ALPHA
       READ(10, *) DALPHA
       READ(10, *) XCHI

C      * DEFAULT MODEL PARAMETERS *
       READ(10, *) OMEGAD
       READ(10, *) OMEGAM
       READ(10, *) LAMBDA0

       READ(10, *) BETA
C      * OUTPUT PARAMETERS *
       READ(10, *) NBIN
       DO I = 1, NBIN+1
          READ(10, *) OMEGABIN(I)
       END DO
       CLOSE(10)

C      ***************************************************************
       LOUTPRX = INDEX(OUTPRX, ' ')-1

       FILENAME = OUTPRX(1:LOUTPRX)//'.LOG'
       OPEN(10, FILE = FILENAME)

       WRITE(10, *) '************************************************'
       WRITE(10, *) 'INPUT DATA         : ', DATAIN
       WRITE(10, *) 'INPUT MODEL        : ', MODEL
       WRITE(10, *) 'OUTPUT FILE PREFIX : ', OUTPRX

       WRITE(10, *) 'TOTAL DATA POINTS  : ', ND
       WRITE(10, *) 'TOTAL OMEGA POINTS : ', NA
       WRITE(10, *) 'CUTOFF ENERGY      : ', ECUTOFF
       WRITE(10, *) 'TEMPERATURE        : ', KT

C      * RAW DATA CORRECTION PARAMETERS *
       WRITE(10, *) 'A1                 : ', A1
       WRITE(10, *) 'A2                 : ', A2
       WRITE(10, *) 'EF                 : ', EF
       WRITE(10, *) 'KF                 : ', KF
```

```
93
94
95  C      * ERROR BARS *
96         IF(ERRB0 .LE. 0.0D0)THEN
97            WRITE(10, *) 'DATA ERROR BAR     : AUTOMATIC'
98         ELSE
99            WRITE(10, *) 'DATA ERROR BAR     : ', ERRB0
100           WRITE(10, *) 'DATA ERROR BAR SLOP: ', ERRB1
101        END IF
102
103 C      * FITTING PARAMETERS *
104        IF(METHOD .EQ. 1)THEN
105           WRITE(10, *) 'MEM METHOD         : HISTORIC'
106           WRITE(10, *) 'TARGET CHI^2       : ', XCHI
107           WRITE(10, *) 'MAX ALPHA          : ', ALPHA
108        ELSE IF(METHOD .EQ. 2)THEN
109           WRITE(10, *) 'MEM METHOD         : CLASSIC'
110        ELSE IF(METHOD .EQ. 3)THEN
111           WRITE(10, *) 'MEM METHOD         : BRYAN'
112           WRITE(10, *) 'MAX ALPHA          : ', ALPHA
113           WRITE(10, *) 'ALPHA STEP         : ', DALPHA
114        ELSE
115           WRITE(10, *) 'MEM METHOD         : NONE'
116        END IF
117
118        WRITE(10, *) 'MAX ITERATION NUMB : ', ITERNUM
119
120
121 C      * DEFAULT MODEL PARAMETERS *
122        IF(MODEL .EQ. 'NONE')THEN
123           WRITE(10, *) 'DEF MODEL OMEGAD   : ', OMEGAD
124           WRITE(10, *) 'DEF MODEL OMEGAM   : ', OMEGAM
125           WRITE(10, *) 'DEF MODEL LAMBDA0  : ', LAMBDA0
126        END IF
127
128        WRITE(10, *) 'WEITHT EXPONENT    : ', BETA
129        WRITE(10, *) 'TOTAL OUT BINS     : ', NBIN
130  200   FORMAT(8F10.2)
131        WRITE(10, 200) (OMEGABIN(I), I = 1, NBIN+1)
132        WRITE(10, *) '************************************************'
133        WRITE(10, *) 'RESULTS:'
```

```
134         WRITE(*, *) 'RESULTS:'
135
136   C     ***************************************************
137
138         OPEN(1, FILE=DATAIN)
139         DO I = 1, NDRAW
140            READ(1, *) ERAW(I), KRAW(I)
141            ERAW(I) = ERAW(I) - EF
142            KRAW(I) = KRAW(I) - KF
143         END DO
144         CLOSE(1)
145
146   C     * DETERMINE THE SUBSET OF THE DISPERSION TO USE *
147         ND = 0
148         IF(STATES .EQ. 0)THEN
149   C        * ALL STATES *
150            DO I = 1, NDRAW
151               IF(ABS(ERAW(I)) .LE. ECUTOFF)THEN
152                  ND = ND + 1
153                  Y(ND) = ERAW(I)
154                  D(ND) = ERAW(I) - A1 *  KRAW(I) - A2 * KRAW(I)**2
155                  K(ND) = KRAW(I)
156               END IF
157            END DO
158         ELSE IF(STATES .EQ. 1)THEN
159   C        * OCCUPIED STATES ONLY *
160            DO I = 1, NDRAW
161               IF(ABS(ERAW(I)) .LE. ECUTOFF .AND. ERAW(I) .LT. 0.0D0)THEN
162                  ND = ND + 1
163                  Y(ND) = ERAW(I)
164                  D(ND) = ERAW(I) - A1 *  KRAW(I) - A2 * KRAW(I)**2
165                  K(ND) = KRAW(I)
166               END IF
167            END DO
168         ELSE IF(STATES .EQ. 2)THEN
169   C        * UNOCCUPIED STATES ONLY *
170            DO I = 1, NDRAW
171               IF(ABS(ERAW(I)) .LE. ECUTOFF .AND. ERAW(I) .GT. 0.0D0)THEN
172                  ND = ND + 1
173                  Y(ND) = ERAW(I)
174                  D(ND) = ERAW(I) - A1 *  KRAW(I) - A2 * KRAW(I)**2
```

```
175               K(ND) = KRAW(I)
176            END IF
177         END DO
178      ELSE
179C        * DEFAULT TO ALL STATES *
180         DO I = 1, NDRAW
181            IF(ABS(ERAW(I)) .LE. ECUTOFF)THEN
182               ND = ND + 1
183               Y(ND) = ERAW(I)
184               D(ND) = ERAW(I) - A1 *  KRAW(I) - A2 * KRAW(I)**2
185               K(ND) = KRAW(I)
186            END IF
187         END DO
188      END IF
189
190      WRITE(10, *) 'ND                  = ', ND
191      WRITE(* , *) 'ND                  = ', ND
192
193C     ****************************************************
194
195C     * DETERMINE THE ERRORS *
196      IF(ERRCALC .EQ. 0)THEN
197         CALL POST_PROCESS(ND, Y, D, SIGMA, ERRB0, ERRB1)
198      ELSE IF(ERRCALC .EQ. 1)THEN
199         CALL POST_PROCESS(ND, Y, D, SIGMA, ERRB0, ERRB1)
200         FILENAME = OUTPRX(1:LOUTPRX)//'_ERR.dat'
201         OPEN(1, FILE = FILENAME)
202            DO I = 1, ND
203               WRITE(1, 100) SIGMA(I)
204            END DO
205         CLOSE(1)
206         WRITE(* , *) 'WRITING ERRORS TO:    ', FILENAME
207         CALL EXIT(0)
208      ELSE IF(ERRCALC .EQ. 2)THEN
209         WRITE(* , *) 'READING ERRORS FROM: ', ERRFILE
210         OPEN(1, FILE=ERRFILE)
211         DO I = 1, ND
212            READ(1, *) SIGMA(I)
213         END DO
214         CLOSE(1)
215
```

```
216         DO I = 1, ND
217            Y(I) =  - Y(I)
218         END DO
219      ELSE
220         WRITE(* , *) 'NOT A VALID ERROR CALCULATION'
221         CALL EXIT(0)
222      END IF
223
224      KT = KT / 1.1604D4
225
226      CALL DSCAL(ND, 1.0D0/KT, Y, 1)
227      CALL DSCAL(ND, 1.0D0/KT, D, 1)
228      CALL DSCAL(ND, 1.0D0/KT, SIGMA, 1)
229
230      CALL DSCAL(NBIN+1, 1D-3/KT, OMEGABIN, 1)
231
232      OMEGAD = OMEGAD / KT
233      OMEGAM = OMEGAM / KT
234
235
236      IF(MODEL .NE. "NONE")THEN
237         OPEN(1, FILE = MODEL)
238         DO I = 1, NA
239            READ(1, *) Y1(I), M(I)
240            Y1(I) = Y1(I) * 1D-3 / KT
241            M(I) = M(I) * LAMBDA0
242         END DO
243         DY1 = Y1(2) - Y1(1)
244         CLOSE(1)
245      ELSE
246         DY1 = OMEGAM / DBLE(NA)
247
248         DO I = 1, NA
249            Y1(I) = DBLE(I) * DY1
250         END DO
251
252         DO I = 1, NA
253            IF(Y1(I) .LE. OMEGAD)THEN
254               M(I) = LAMBDA0 * (Y1(I) / OMEGAD)**2
255            ELSE IF(Y1(I) .LE. OMEGAM)THEN
256               M(I) = LAMBDA0
```

```
257               ELSE
258                  M(I) = ZERO
259               END IF
260               IF(M(I) .LE. 0.0D0) M(I) = ZERO
261            END DO
262         END IF
263
264
265         X1 = 0.0D0
266         X2 = 0.0D0
267         X12 = 0.0D0
268         DO I = 1, ND
269            X1 = X1 + K(I)**2 / SIGMA(I)**2
270            X2 = X2 + K(I)**4 / SIGMA(I)**2
271            X12 = X12 + K(I)**3 / SIGMA(I)**2
272         END DO
273         XX = X1*X2 - X12**2
274         X1 = X1 / XX
275         X2 = X2 / XX
276         X12 = -X12 / XX
277
278         CALL SETUP_KERN(ND, NA, Y, Y1, DY1, KERN)
279
280   C     ******************************************
281         DA1 = 1.0D0
282         DA2 = 1.0D0
283         A1 = -A1
284         A2 = -A2
285         J = 0
286         DO WHILE((DA1 .GT. 1D-3 .OR. DA2 .GT. 1D-2) .AND. J .LE. 200)
287            J = J + 1
288            IF(METHOD .EQ. 1)THEN
289               CALL MEMFIT_HST(ND, NA, ITERNUM, KERN, D, SIGMA, M,
290        $           A, DA, ALPHA, XCHI, EM)
291            ELSE IF(METHOD .EQ. 2)THEN
292               CALL MEMFIT_CLS(ND, NA, ITERNUM, KERN, D, SIGMA, M,
293        $           A, DA, ALPHA, DALPHA, EM)
294            ELSE IF(METHOD .EQ. 3)THEN
295               CALL MEMFIT_BRYAN(ND, NA, ITERNUM, KERN, D, SIGMA, M,
296        $           A, DA, ALPHA, DALPHA, EM)
297            ELSE IF(METHOD .EQ. 4)THEN
```

```
298              CALL MEMFIT_FIXALPHA(ND, NA, ITERNUM, KERN, D, SIGMA, M,
299       $           A, DA, ALPHA, DALPHA, EM)
300           ELSE
301              STOP
302           END IF
303
304           IF(FITBPD .EQ. 0)GOTO 1000
305
306
307           CALL DGEMV('N', ND, NA, 1.0D0, KERN, ND, A, 1, 0.0D0, D1, 1)
308
309           S1 = 0.0D0
310           S2 = 0.0D0
311           DO I = 1, ND
312              S1 = S1 + KT * (Y(I)+ D1(I)) * K(I) / SIGMA(I)**2
313              S2 = S2 + KT * (Y(I)+ D1(I)) * K(I)**2 / SIGMA(I)**2
314           END DO
315
316           DA1 = A1
317           DA2 = A2
318
319           A1 =  X2 * S1 + X12 * S2
320           A2 =  X12 * S1 + X1 * S2
321
322           DA1 = ABS(DA1 - A1) / ABS(A1)
323           DA2 = ABS(DA2 - A2) / ABS(A2)
324
325           DO I = 1, ND
326              D(I) = (A1 *  K(I) + A2 * K(I)**2) / KT - Y(I)
327           END DO
328
329           PRINT*, J, A1, A2
330        END DO
331
332   1000 A1 = -A1
333        A2 = -A2
334
335        WRITE(*, *) 'A1                  = ', A1
336        WRITE(*, *) 'A2                  = ', A2
337
338        WRITE(10, *) 'A1                  = ', A1
```

```
339         WRITE(10, *) 'A2                  = ', A2
340
341
342         CHI0 = CHI(ND, NA, KERN, D, SIGMA, A)
343         S = 0.0D0
344         DO I = 1, NA
345            S = S + A(I) - M(I) + A(I) * LOG(A(I) / M(I))
346         END DO
347         Q = CHI0 / 2.0D0 - ALPHA * S
348
349         WRITE(10, *) 'CHI^2               = ', CHI0
350         WRITE(10, *) 'Q                   = ', Q
351
352         WRITE(*, *) 'CHI^2                = ', CHI0
353         WRITE(*, *) 'Q                    = ', Q
354
355         IF(METHOD .EQ. 1 .OR. METHOD .EQ. 2)THEN
356            WRITE(10, *) 'ALPHA                = ', ALPHA
357            WRITE(*, *) 'ALPHA                 = ', ALPHA
358         END IF
359         IF(METHOD .EQ. 1)THEN
360            WRITE(10, *) 'DALPHA               = ', DALPHA
361            WRITE(*, *) 'DALPHA                = ', DALPHA
362         END IF
363
364         CALL DGEMV('N', ND, NA, 1.0D0, KERN, ND, A, 1, 0.0D0, D1, 1)
365
366         FILENAME = OUTPRX(1:LOUTPRX)//'_DAT.dat'
367         OPEN(1, FILE = FILENAME)
368         DO I = 1, ND
369            IMS = IMSIGMA(NA, Y(I), A, Y1, DY1)
370            WRITE(1, 300) Y(I)*KT*1D3, D(I)*KT*1D3, SIGMA(I)*KT*1D3,
371        $         D1(I)*KT*1D3, IMS*KT*1D3
372         END DO
373         CLOSE(1)
374
375         FILENAME = OUTPRX(1:LOUTPRX)//'_SPT.dat'
376         OPEN(1, FILE = FILENAME)
377         DO I = 1, NA
378            WRITE(1, 100) Y1(I)*KT*1000.0, A(I), M(I)
379         END DO
```

```
380         CLOSE(1)
381
382
383         CALL WEIGHT(NA, NBIN, OMEGABIN, BETA, A, Y1, DY1, EM,
384        $      EBX, EBY, EBDX, EBDY)
385
386         FILENAME = OUTPRX(1:LOUTPRX)//'_WGT.dat'
387         OPEN(1, FILE = FILENAME)
388         DO I = 1, NBIN
389            WRITE(1, 100) EBX(I)*KT*1000.0, EBY(I), EBDX(I)*KT*1000.0,
390        $         EBDY(I)
391         END DO
392         CLOSE(1)
393
394         CALL INTAVG(NA, A, Y1, DY1, EM, LAMBDA, DLAMBDA, OMEGALOG)
395
396         WRITE(10, *) 'LAMBDA              = ', LAMBDA
397         WRITE(10, *) 'DLAMBDA             = ', DLAMBDA
398         WRITE(10, *) 'OMEGALOG            = ', OMEGALOG * KT * 1D3
399
400         WRITE(*, *) 'LAMBDA              = ', LAMBDA
401         WRITE(*, *) 'DLAMBDA             = ', DLAMBDA
402         WRITE(*, *) 'OMEGALOG            = ', OMEGALOG * KT * 1D3
403
404         CLOSE(10)
405
406   C     ************ DISPERSION OUTPUT *************************
407         FILENAME = OUTPRX(1:LOUTPRX)//'_DSP.dat'
408         OPEN(1, FILE = FILENAME)
409
410         CALL DSCAL(NDRAW, -1.0D0/KT, ERAW, 1)
411         CALL SETUP_KERN(NDRAW, NA, ERAW, Y1, DY1, KERN)
412         CALL DGEMV('N', NDRAW, NA, 1.0D0, KERN, NDRAW, A, 1, 0.0D0, D1, 1)
413
414         DO I = 1, NDRAW
415            E0 = - (ERAW(I) + D1(I)) * KT
416            K(I) = 2.0D0*E0/(ABS(A1) + SQRT(A1**2+4.0D0*A2*E0)) *
417        $         DSIGN(-1.0D0, A1)
418            IMS = IMSIGMA(NA, ERAW(I), A, Y1, DY1)
419            WRITE(1, 300) -ERAW(I) * KT, KRAW(I), K(I),
420        $         IMS * KT,
```

```
421       $        2.0D0 * IMS * KT /ABS(A1 + 2.0D0 * A2 * K(I))
422        END DO
423        CLOSE(1)
424
425
426    100 FORMAT(4G20.8)
427    300 FORMAT(5G16.8)
428
429
430        STOP
431        END
432
433
434    C   ***********************************************************
435
436        SUBROUTINE POST_PROCESS(ND, E, D, SIGMA, ERRB0, ERRB1)
437        IMPLICIT NONE
438        INCLUDE 'MEM_inc.f'
439        INTEGER NBIN
440        PARAMETER(NBIN = 9)
441        INTEGER ND
442        DOUBLE PRECISION D(ND), E(ND), SIGMA(ND), DV, EOFFSET, EF,
443       $     ERRB0, ERRB1, SIGMABAR
444        DOUBLE PRECISION Q(NBIN, 3), QD(NBIN), QTQ(3, 3), QTD(3)
445        DOUBLE PRECISION DNRM2
446        INTEGER I, J, K, IL
447        INTEGER IPIV(3), INFO
448
449
450        DO I = 1, ND
451           E(I) =  - E(I)
452        END DO
453
454        IF(ERRB0 .LE. 0D0)THEN
455           DO I = 1, ND
456              IL = I - NBIN/2
457              IF(IL .LE. 0) IL = 1
458              IF(IL + NBIN .GT. ND) IL = ND - NBIN + 1
459
460              DO J = 1, NBIN
461                 QD(J) = D(IL + J - 1)
```

```
462             END DO
463
464             DO K = 1, 3
465                DO J = 1, NBIN
466                   Q(J, K) = E(IL + J - 1) ** (K-1)
467                END DO
468             END DO
469
470             CALL DGEMM('T', 'N', 3, 3, NBIN, 1.0D0, Q, NBIN,
471      $           Q, NBIN, 0.0D0, QTQ, 3)
472             CALL DGEMV('T', NBIN, 3, 1.0D0, Q,  NBIN, QD, 1,
473      $           0.0D0, QTD, 1 )
474
475             CALL DGESV(3, 1, QTQ, 3, IPIV, QTD, 3, INFO)
476
477
478             CALL DGEMV('N', NBIN, 3, 1.0D0, Q, NBIN, QTD, 1,
479      $           -1.0D0, QD, 1)
480
481             SIGMA(I) = DNRM2(NBIN, QD, 1) / SQRT(DBLE(NBIN-3))
482          END DO
483
484          SIGMABAR = 0.0D0
485          DO I = 1, ND
486             SIGMABAR = SIGMABAR + SIGMA(I)**2
487          END DO
488          SIGMABAR = SQRT(SIGMABAR / DBLE(ND))
489
490          IF(ERRB0 .EQ. 0.0)THEN
491             DO I = 1, ND
492                SIGMA(I) = SIGMABAR
493             END DO
494          END IF
495
496          WRITE(10, *) 'SIGMABAR           = ', SIGMABAR
497          WRITE(* , *) 'SIGMABAR           = ', SIGMABAR
498       ELSE
499          DO I = 1, ND
500             SIGMA(I) = ERRB0 + ERRB1 * E(I)
501          END DO
502       END IF
```

```
503
504         RETURN
505         END
506
507
508         SUBROUTINE SETUP_KERN(ND, NA, Y, Y1, DY1, KERN)
509         IMPLICIT NONE
510         INCLUDE 'MEM_inc.f'
511         INTEGER ND, NA
512         DOUBLE PRECISION Y(ND), Y1(NA), DY1, KERN(ND, NA)
513         DOUBLE PRECISION GN, G
514         INTEGER I, J, N
515
516         DO J = 1, NA
517            DO I = 1, ND
518
519               G = 0.0D0
520               GN = 1.0D0
521               N = 0
522               DO WHILE (ABS(GN) .GT. 1D-6 * ABS(G))
523                  GN = 8 * PI2 * DBLE(2*N+1) * Y(I) * Y1(J) /
524        $              ((Y(I)-Y1(J))**2+DBLE(2*N+1)**2*PI2) /
525        $              ((Y(I)+Y1(J))**2+DBLE(2*N+1)**2*PI2)
526                  G = G + GN
527                  N = N + 1
528               END DO
529               KERN(I, J) = G * DY1
530
531            END DO
532         END DO
533
534         RETURN
535         END
536
537
538   C     ************************************************
539         SUBROUTINE WEIGHT(NA, NBIN, OMEGABIN, BETA, A, Y1, DY1, EM,
540        $     EBX, EBY, EBDX, EBDY)
541         IMPLICIT NONE
542         INCLUDE 'MEM_inc.f'
543         INTEGER NA, NBIN
```

```
544         DOUBLE PRECISION A(NA), Y1(NA), DY1, EM(NA, NA), OMEGABIN(*), BETA
545         DOUBLE PRECISION EBX(NBIN), EBY(NBIN), EBDX(NBIN), EBDY(NBIN)
546         INTEGER  I, J, K, L, L0, L1, NL
547
548         L = 1
549         DO WHILE(Y1(L) .LT. OMEGABIN(1))
550            L = L + 1
551         END DO
552
553         DO I = 1, NBIN
554
555            EBX(I)  = (OMEGABIN(I+1) + OMEGABIN(I))/2.0D0
556            EBDX(I) = (OMEGABIN(I+1) - OMEGABIN(I))/2.0D0
557
558            L0 = L
559            EBY(I) = 0.0D0
560            DO WHILE(Y1(L) .LT. OMEGABIN(I+1) .AND. L .LE. NA)
561               EBY(I) = EBY(I) + A(L) * Y1(L)**BETA
562               L = L + 1
563            END DO
564            L1 = L - 1
565
566            EBY(I) = EBY(I) * DY1
567
568            EBDY(I) = 0.0D0
569            DO J = L0, L1
570               DO K = L0, L1
571                  EBDY(I) = EBDY(I) + EM(J, K) * (Y1(J)*Y1(K))**BETA
572               END DO
573            END DO
574            EBDY(I) = SQRT(EBDY(I))* DY1
575         END DO
576
577         RETURN
578         END
579
580
581
582
583         SUBROUTINE INTAVG(NA, A, Y1, DY, EM, LAMBDA, DLAMBDA,
584        $     OMEGALOG)
```

```
585         IMPLICIT NONE
586         INCLUDE 'MEM_inc.f'
587         INTEGER NA
588         DOUBLE PRECISION A(NA), Y1(NA), DY, EM(NA, NA)
589         DOUBLE PRECISION LAMBDA, DLAMBDA, OMEGALOG
590         INTEGER I, J
591
592         LAMBDA = 0.0D0
593         DO I = 1, NA
594            LAMBDA = LAMBDA + A(I) / Y1(I)
595         END DO
596         LAMBDA = 2.0D0 * LAMBDA * DY
597
598         DLAMBDA = 0.0D0
599         DO J =1, NA
600            DO I = 1, NA
601               DLAMBDA = DLAMBDA + EM(I, J) / Y1(I) / Y1(J)
602            END DO
603         END DO
604
605         DLAMBDA = SQRT(DLAMBDA) * 2.0D0 * DY
606
607
608         OMEGALOG = 0.0D0
609         DO I = 1, NA
610            OMEGALOG = OMEGALOG + A(I) / Y1(I) * LOG(Y1(I))
611         END DO
612         OMEGALOG = EXP(2.0D0 * OMEGALOG * DY / LAMBDA)
613
614         RETURN
615         END
616
617
618   C     ************************************************
619
620
621         DOUBLE PRECISION FUNCTION IMSIGMA(NA, Y, AF, Y1, DY1)
622         IMPLICIT NONE
623         INCLUDE 'MEM_inc.f'
624         INTEGER NA
625         DOUBLE PRECISION Y, KT, AF(NA), Y1(NA), DY1
```

```
626         DOUBLE PRECISION F, NB
627         INTEGER I
628
629         IMSIGMA = 0.0D0
630
631         DO I = 1, NA
632            IMSIGMA = IMSIGMA + AF(I) *
633        $         (F(Y1(I)-Y)+F(Y1(I)+Y) + 2.0D0 * NB(Y1(I)))
634         END DO
635
636         IMSIGMA = IMSIGMA * PI * DY1
637
638         RETURN
639         END
640
641
642
643
644         DOUBLE PRECISION FUNCTION NORM_RAND(SIGMA)
645         IMPLICIT NONE
646         DOUBLE PRECISION SIGMA, RAND
647         INTEGER I, N
648
649         N = 10
650
651         NORM_RAND = 0.0D0
652         DO I = 1, N
653            NORM_RAND = NORM_RAND + SQRT(12.0D0) * (RAND() - 0.5D0) * SIGMA
654         END DO
655
656         NORM_RAND = NORM_RAND / DBLE(N)
657
658         RETURN
659         END
660
661
662         double precision function f(x)
663         double precision x
664
665         if(x.ge. 0)then
666            f = exp(-x)/(exp(-x)+1.0d0)
```

```
667         else
668            f = 1.0d0/(exp(x) + 1.0d0)
669         end if
670
671         return
672         end
673
674
675         double precision function nb(x)
676
677         double precision x
678
679         nb = exp(-x)/(-exp(-x)+1.0d0)
680
681         return
682         end
```

MEM_inc.f

```
1         INTEGER NMAX
2         PARAMETER(NMAX = 1000)
3         DOUBLE PRECISION PI, PI2, ZERO
4         PARAMETER(PI = 3.14159265358979D0, PI2 = 9.86960440108934D0)
5         PARAMETER(ZERO = 1D-20)
6         DOUBLE PRECISION EPS
7         PARAMETER(EPS = 1D-4)
```

MEM_ALG.f

```
1         SUBROUTINE MEMFIT_CLS(ND, NA, ITERNUM, KERN, D, SIGMA, M,
2        $     A, DA, ALPHA, DALPHA, EM)
3         IMPLICIT NONE
4         INCLUDE 'MEM_inc.f'
5         INTEGER ND, NA, ITERNUM
6         DOUBLE PRECISION KERN(ND, NA), D(ND), SIGMA(ND)
7         DOUBLE PRECISION M(NA), A(NA), ALPHA, DA, DALPHA, EM(NA, NA)
8         DOUBLE PRECISION KTK(NMAX, NMAX), KTD(NMAX), DDQ(NMAX, NMAX)
9         DOUBLE PRECISION ALPHA0, ALPHA1, ALPHA2, CHI1
10        DOUBLE PRECISION CHI, XCHI
11        INTEGER I
12
13        CALL SETUP_KTK(ND, NA, KERN, SIGMA, KTK)
```

```
14        CALL SETUP_KTD(ND, NA, KERN, D, SIGMA, KTD)
15
16        DO I = 1, NA
17           A(I) = (1.0D0 + 1D-6) * M(I)
18        END DO
19
20        DA = 1.0D0
21        DALPHA = 1.0D0
22        ALPHA = 1.0D0
23        I = 0
24        DO WHILE((DA .GT. 1D-8 .OR. DALPHA. GT. 1D-8)
25       $      .AND. I .LE. ITERNUM)
26           CALL SKILLING_ITR(NA, KTK, KTD, M, A, ALPHA, DA)
27           CALL ALPHA_ITR(NA, KTK, M, A, ALPHA, DALPHA)
28           I = I + 1
29        END DO
30
31        CALL ERROR_MATRIX(NA, KTK, A, ALPHA, DDQ, EM)
32
33        RETURN
34
35        END
36
37
38        SUBROUTINE MEMFIT_FIXALPHA(ND, NA, ITERNUM, KERN, D, SIGMA, M,
39       $      A, DA, ALPHA, DALPHA, EM)
40        IMPLICIT NONE
41        INCLUDE 'MEM_inc.f'
42        INTEGER ND, NA, ITERNUM
43        DOUBLE PRECISION KERN(ND, NA), D(ND), SIGMA(ND)
44        DOUBLE PRECISION M(NA), A(NA), ALPHA, DA, DALPHA, EM(NA, NA)
45        DOUBLE PRECISION KTK(NMAX, NMAX), KTD(NMAX), DDQ(NMAX, NMAX)
46        DOUBLE PRECISION ALPHA0, ALPHA1, ALPHA2, CHI1
47        DOUBLE PRECISION CHI, XCHI
48        INTEGER I
49
50        CALL SETUP_KTK(ND, NA, KERN, SIGMA, KTK)
51        CALL SETUP_KTD(ND, NA, KERN, D, SIGMA, KTD)
52
53        DO I = 1, NA
54           A(I) = (1.0D0 + 1D-6) * M(I)
```

```
55          END DO
56
57          DA = 1.0D0
58          I = 0
59          DO WHILE(DA .GT. 1D-8 .AND. I .LE. ITERNUM)
60             CALL SKILLING_ITR(NA, KTK, KTD, M, A, ALPHA, DA)
61             I = I + 1
62          END DO
63
64          CALL ERROR_MATRIX(NA, KTK, A, ALPHA, DDQ, EM)
65
66          RETURN
67
68          END
69
70
71
72          SUBROUTINE MEMFIT_HST(ND, NA, ITERNUM, KERN, D, SIGMA, M,
73         $     A, DA, ALPHA, XCHI, EM)
74          IMPLICIT NONE
75          INCLUDE 'MEM_inc.f'
76          INTEGER ND, NA, ITERNUM
77          DOUBLE PRECISION KERN(ND, NA), D(ND), SIGMA(ND)
78          DOUBLE PRECISION M(NA), A(NA), ALPHA, DA, EM(NA, NA)
79          DOUBLE PRECISION KTK(NMAX, NMAX), KTD(NMAX), DDQ(NMAX, NMAX)
80          DOUBLE PRECISION ALPHA0, ALPHA1, ALPHA2, CHI1
81          DOUBLE PRECISION CHI, XCHI
82          INTEGER I
83
84          CALL SETUP_KTK(ND, NA, KERN, SIGMA, KTK)
85          CALL SETUP_KTD(ND, NA, KERN, D, SIGMA, KTD)
86
87          DO I = 1, NA
88             A(I) = (1.0D0 + 1.0D-6) * M(I)
89          END DO
90
91
92          ALPHA0 = 0.0D0
93          ALPHA2 = ALPHA
94
95          ALPHA1 = ALPHA / 2.0D0
```

```
      CHI1 = DBLE(ND) * 2.0D0

      DO WHILE (ABS(CHI1-XCHI) .GE. 0.1D0)
         IF(ALPHA1 .LE. 1D-3)THEN
            WRITE(10, *) 'TARGET CHI^2 CAN NOT BE SATISFIED.'
            WRITE(*, *) 'TARGET CHI^2 CAN NOT BE SATISFIED.'
            STOP
         END IF
         IF(ALPHA - ALPHA1 .LE. 1D-3)THEN
            WRITE(10, *) 'TRY TO INCREASE PARAMETER ALPHA'
            WRITE(*, *) 'TRY TO INCREASE PARAMETER ALPHA'
            STOP
         END IF

         DA = 1.0D0
         I = 0
         DO WHILE(DA .GT. 1D-8 .AND. I .LE. ITERNUM)
            CALL SKILLING_ITR(NA, KTK, KTD, M, A, ALPHA1, DA)
            I = I + 1
         END DO
         CHI1 = CHI(ND, NA, KERN, D, SIGMA, A)
         IF(CHI1 .LE. XCHI)THEN
            ALPHA0 = ALPHA1
            ALPHA1 = (ALPHA1 + ALPHA2) / 2.0D0
         ELSE
            ALPHA2 = ALPHA1
            ALPHA1 = (ALPHA1 + ALPHA0) / 2.0D0
         END IF
C          PRINT*, ALPHA1, CHI1, DA
      END DO

      ALPHA = ALPHA1

      CALL ERROR_MATRIX(NA, KTK, A, ALPHA, DDQ, EM)

      RETURN

      END


      SUBROUTINE MEMFIT_BRYAN(ND, NA, ITERNUM, KERN, D, SIGMA, M,
```

```
137       $     A, DA, ALPHAMAX, DALPHA, EM)
138        IMPLICIT NONE
139        INCLUDE 'MEM_inc.f'
140        INTEGER ND, NA, ITERNUM
141        DOUBLE PRECISION KERN(ND, NA), D(ND), SIGMA(ND), A1(NMAX)
142        DOUBLE PRECISION M(NA), A(NA), ALPHAMAX, DA, DALPHA, EM(NA, NA)
143        DOUBLE PRECISION KTK(NMAX, NMAX), KTD(NMAX), DDQ(NMAX, NMAX),
144       $     EM1(NMAX, NMAX)
145        DOUBLE PRECISION ALPHA, PTOT
146        DOUBLE PRECISION CHI, P_ALPHA, P
147        INTEGER I, J
148
149        OPEN(14, FILE='P.DAT')
150
151        CALL SETUP_KTK(ND, NA, KERN, SIGMA, KTK)
152        CALL SETUP_KTD(ND, NA, KERN, D, SIGMA, KTD)
153
154
155        PTOT = 0.0D0
156
157        DO I = 1, NA
158           A(I) = 0.0D0
159        END DO
160
161        DO J = 1, NA
162           DO I = 1, NA
163              EM(I, J) = 0.0D0
164           END DO
165        END DO
166
167        DO ALPHA = ALPHAMAX, DALPHA, -DALPHA
168           DA = 1.0D0
169           DO I = 1, NA
170              A1(I) = (1.0D0 + 1D-6) * M(I)
171           END DO
172
173           I = 0
174           DO WHILE(DA .GT. 1D-3 .AND. I .LE. ITERNUM)
175              CALL SKILLING_ITR(NA, KTK, KTD, M, A1, ALPHA, DA)
176              I = I + 1
177           END DO
```

```
178
179           P = P_ALPHA(ND, NA, KERN, D, SIGMA, KTK, M, A1, ALPHA)
180           PTOT = P + PTOT
181
182           DO I = 1, NA
183              A(I) = A(I) + A1(I) * P
184           END DO
185
186           CALL ERROR_MATRIX(NA, KTK, A1, ALPHA, DDQ, EM1)
187           CALL DAXPY(NA*NA, P, EM1, 1, EM, 1)
188
189           WRITE(14, *) ALPHA, P
190        END DO
191
192        CALL DSCAL(NA, 1.0D0/PTOT, A, 1)
193        CALL DSCAL(NA*NA, 1.0D0/PTOT, EM, 1)
194
195        WRITE(10, *) 'LOG(W)              = ', LOG(PTOT * DALPHA)
196        WRITE(* , *) 'LOG(W)              = ', LOG(PTOT * DALPHA)
197
198        RETURN
199
200        END
201
202
203
204        SUBROUTINE SETUP_KTK(ND, NA, KERN, SIGMA, KTK)
205        IMPLICIT NONE
206        INCLUDE 'MEM_inc.f'
207        INTEGER ND, NA
208        DOUBLE PRECISION KERN(ND, NA), SIGMA(ND), KTK(NA, NA)
209        INTEGER I, J, K
210
211        DO J = 1, NA
212           DO I = 1, NA
213              KTK(I, J) = 0.0D0
214              DO K = 1, ND
215                 KTK(I, J) = KTK(I, J) + KERN(K, I) * KERN(K, J) /
216       $              SIGMA(K)**2
217              END DO
218           END DO
```

```
219         END DO
220
221         RETURN
222         END
223
224
225
226         SUBROUTINE SETUP_KTD(ND, NA, KERN, D, SIGMA, KTD)
227         IMPLICIT NONE
228         INCLUDE 'MEM_inc.f'
229         INTEGER ND, NA
230         DOUBLE PRECISION KERN(ND, NA), D(ND), SIGMA(ND)
231         DOUBLE PRECISION KTD(NA)
232         INTEGER I, J, K
233
234         DO I = 1, NA
235            KTD(I) = 0.0D0
236            DO K = 1, ND
237               KTD(I) = KTD(I) + KERN(K, I) * D(K) / SIGMA(K)**2
238            END DO
239         END DO
240
241         RETURN
242         END
243
244
245         SUBROUTINE SKILLING_ITR(NA, KTK, KTD, M, A, ALPHA, DA)
246         IMPLICIT NONE
247         INCLUDE 'MEM_inc.f'
248         INTEGER NA
249         DOUBLE PRECISION KTK(NA, NA), KTD(NA), M(NA), A(NA), ALPHA, DA
250         DOUBLE PRECISION E0(NMAX, 3), E(NMAX, 3), TEMP(NMAX)
251         DOUBLE PRECISION Q(3, 3), V(3)
252         DOUBLE PRECISION NRME1, NRME2, ETA, ETAMIN
253         INTEGER I, J
254         INTEGER IPIV(3), INFO
255         DOUBLE PRECISION DNRM2, DDOT
256
257   C     ***
258         DO I = 1, NA
259            E0(I, 1) = - LOG(A(I) / M(I))
```

```
260         END DO
261         NRME1 = DNRM2(NA, E0(1, 1), 1)
262
263   C     ***
264         CALL DCOPY(NA, KTD, 1, E0(1, 2), 1)
265         CALL DGEMV('N', NA, NA, 1.0D0, KTK, NA, A, 1, -1.0D0, E0(1, 2), 1)
266         NRME2 = DNRM2(NA, E0(1, 2), 1)
267
268
269         DO I = 1, NA
270            TEMP(I) = - E0(I, 2) + ALPHA * E0(I, 1)
271         END DO
272         DA =  DNRM2(NA, TEMP, 1)
273
274   C     ***
275         DO I = 1, NA
276            TEMP(I) = (E0(I, 1)/NRME1 - E0(I, 2)/NRME2) * A(I)
277         END DO
278
279         DO I = 1, NA
280            E0(I, 3) = 0.0D0
281         END DO
282         CALL DGEMV('N', NA, NA, 1.0D0, KTK, NA, TEMP,1, 0.0D0, E0(1,3),1)
283
284   C     ***
285         DO J = 1, 3
286            DO I = 1, NA
287               E(I, J) = A(I) * E0(I, J)
288            END DO
289         END DO
290
291   C     ***
292         CALL DCOPY(NA, E0(1, 2), 1, TEMP, 1)
293         CALL DAXPY(NA, -ALPHA, E0(1, 1), 1, TEMP, 1)
294
295         DO J = 1, 3
296            V(J) = -DDOT(NA, TEMP, 1, E(1, J), 1)
297         END DO
298
299   C     ***
300         DO J = 1, 3
```

```
301            DO I = 1, NA
302               TEMP(I) = EO(I, J) * ALPHA
303            END DO
304
305            CALL DGEMV('N', NA, NA, 1.0D0, KTK, NA, E(1, J), 1,
306         $         1.0D0, TEMP, 1)
307
308            DO I = J, 3
309               Q(I, J) = DDOT(NA, E(1, I), 1, TEMP, 1)
310               Q(J, I) = Q(I, J)
311            END DO
312         END DO
313
314
315         CALL DGESV(3, 1, Q, 3, IPIV, V, 3, INFO)
316
317         DO I = 1, NA
318            TEMP(I) = 0.0D0
319         END DO
320         DO I = 1, 3
321            CALL DAXPY(NA, V(I), E(1, I), 1, TEMP, 1)
322         END DO
323
324   C      DA = DNRM2(NA, TEMP, 1)
325
326         ETAMIN = 1D0
327         DO I = 1, NA
328            IF(TEMP(i) .LT. 0.0D0)THEN
329               ETA = - 0.5D0 * A(I) / TEMP(I)
330               IF(ETA .LT. ETAMIN) ETAMIN = ETA
331            END IF
332         END DO
333
334         CALL DAXPY(NA, ETAMIN, TEMP, 1, A, 1)
335   C      DA = DA * ETAMIN
336
337         RETURN
338         END
339
340
341
```

```
342
343         SUBROUTINE ALPHA_ITR(NA, KTK, M, A, ALPHA, DALPHA)
344         IMPLICIT NONE
345         INCLUDE 'MEM_inc.f'
346         INTEGER NA
347         DOUBLE PRECISION KTK(NA, NA), M(NA), A(NA), ALPHA, DALPHA
348         DOUBLE PRECISION AKTKA(NMAX, NMAX), LAMBDA(NMAX), S
349         DOUBLE PRECISION ALPHA0, F, DF, DAL
350         INTEGER LWORK, LIWORK, INFO
351         PARAMETER(LWORK = 32 * NMAX, LIWORK = 10 * NMAX)
352         DOUBLE PRECISION WORK(LWORK)
353         INTEGER IWORK(LIWORK), ISUPPZ(2*NMAX)
354         INTEGER I, J, L
355
356
357         ALPHA0 = ALPHA
358
359         DO J = 1, NA
360            DO I = 1, NA
361               AKTKA(I, J) = SQRT(A(I)) * KTK(I, J) * SQRT(A(J))
362            END DO
363         END DO
364
365         CALL DSYEVR('N', 'A', 'U', NA, AKTKA, NMAX,
366        $      0.0D0, 0.0D0, 0, 0, 0.0D0, L, LAMBDA, AKTKA, NMAX, ISUPPZ,
367        $      WORK, LWORK, IWORK, LIWORK, INFO )
368
369
370         S = 0.0D0
371
372         DO I = 1, NA
373            S = S + A(I) - M(I) - A(I) * LOG(A(I) / M(I))
374         END DO
375
376
377         DAL = ALPHA
378         DO WHILE (ABS(DAL) .GT. 1D-6 * ALPHA)
379            F = 2.0D0 * ALPHA * S
380            DF = 2.0D0 * S
381            DO I = 1, NA
382               F = F + LAMBDA(I) / (ALPHA + LAMBDA(I))
```

```
383               DF = DF - LAMBDA(I) / (ALPHA + LAMBDA(I))**2
384            END DO
385
386            DAL = - F / DF * 0.1D0
387
388            ALPHA = ALPHA + DAL
389         END DO
390
391         DALPHA = ABS(ALPHA - ALPHA0)
392
393         RETURN
394         END
395
396
397
398         DOUBLE PRECISION FUNCTION P_ALPHA(ND, NA, KERN, D, SIGMA,
399        $     KTK, M, A, ALPHA)
400         IMPLICIT NONE
401         INCLUDE 'MEM_inc.f'
402         INTEGER ND, NA
403         DOUBLE PRECISION KTK(NA, NA), M(NA), A(NA), ALPHA
404         DOUBLE PRECISION KERN(ND, NA), SIGMA(ND), D(ND)
405         DOUBLE PRECISION AKTKA(NMAX, NMAX), LAMBDA(NMAX), S
406         INTEGER LWORK, LIWORK, INFO
407         PARAMETER(LWORK = 32 * NMAX, LIWORK = 10 * NMAX)
408         DOUBLE PRECISION WORK(LWORK)
409         INTEGER IWORK(LIWORK), ISUPPZ(2*NMAX)
410         DOUBLE PRECISION CHI, Q
411         INTEGER I, J, L
412
413
414         DO J = 1, NA
415            DO I = 1, NA
416               AKTKA(I, J) = SQRT(A(I)) * KTK(I, J) * SQRT(A(J))
417            END DO
418         END DO
419
420         CALL DSYEVR('N', 'A', 'U', NA, AKTKA, NMAX,
421        $     0.0D0, 0.0D0, 0, 0, 0.0D0, L, LAMBDA, AKTKA, NMAX, ISUPPZ,
422        $     WORK, LWORK, IWORK, LIWORK, INFO )
423
```

```
424
425 C      *** ENTROPY ***
426         S = 0.0D0
427         DO I = 1, NA
428            S = S + A(I) - M(I) - A(I) * LOG(A(I) / M(I))
429         END DO
430
431         Q = ALPHA * S - CHI(ND, NA, KERN, D, SIGMA, A) / 2.0D0
432
433         P_ALPHA = EXP(Q)
434         DO I = 1, NA
435            P_ALPHA = P_ALPHA * SQRT( ALPHA / (ALPHA + LAMBDA(I)))
436         END DO
437         P_ALPHA = P_ALPHA / ALPHA
438
439
440         RETURN
441         END
442
443
444         DOUBLE PRECISION FUNCTION CHI(ND, NA, KERN, D, SIGMA, A)
445         IMPLICIT NONE
446         INCLUDE 'MEM_inc.f'
447         INTEGER ND, NA
448         DOUBLE PRECISION KERN(ND, NA), D(ND), SIGMA(ND), A(NA)
449         INTEGER I
450         DOUBLE PRECISION TEMP(NMAX)
451
452         CALL DGEMV('N', ND, NA, 1.0D0, KERN, ND, A, 1, 0.0D0, TEMP, 1)
453         CALL DAXPY(ND, -1.0D0, D, 1, TEMP, 1)
454
455         CHI = 0.0D0
456         DO I = 1, ND
457            CHI = CHI + TEMP(I)**2 / SIGMA(I)**2
458         END DO
459
460         RETURN
461         END
462
463
464
```

```
465         SUBROUTINE ERROR_MATRIX(NA, KTK, A, ALPHA, DDQ, DADA)
466         IMPLICIT NONE
467         INCLUDE 'MEM_inc.f'
468         INTEGER NA
469         DOUBLE PRECISION KTK(NA, NA), DADA(NA, NA), DDQ(NA, NA)
470         DOUBLE PRECISION A(NA), ALPHA, M(NA)
471         INTEGER I, J,  IPIV(NMAX), INFO
472
473         CALL DCOPY(NA*NA, KTK, 1, DDQ, 1)
474
475         DO I = 1, NA
476            DDQ(I, I) = DDQ(I, I) + ALPHA / A(I)
477         END DO
478
479
480         DO J = 1, NA
481            DO I = 1, NA
482               DADA(I, J) = 0.0D0
483            END DO
484         END DO
485
486         DO I = 1, NA
487            DADA(I, I) = 1.0D0
488         END DO
489
490         CALL DGESV(NA, NA, DDQ, NA, IPIV, DADA, NA, INFO)
491
492         RETURN
493         END
```

Bibliography

[1] L. D. Landau and E. M. Lifschitz. *Quantum Mechanics: Non-relativistic Theory.* 3rd ed. Vol. 3. Course of Theoretical Physics. London: Pergamon Press, 1977. ISBN: 0750635398.

[2] K. v. Klitzing, Dorda G., and Pepper M. "New Method for High-Accuracy Determination of the Fine-Structure Constant Based on Quantized Hall Resistance". In: *Phys. Rev. Lett.* 45.6 (1980), pp. 494–497.

[3] Laughlin R. B. "Quantized Hall conductivity in two dimensions". In: *Phys. Rev. B* 23.10 (1981), pp. 5632–5633.

[4] Thouless D. J. et al. "Quantized Hall Conductance in a Two-Dimensional Periodic Potential". In: *Phys. Rev. Lett.* 49.6 (1982), pp. 405–408.

[5] Mahito Kohmoto. "Topological invariant and the quantization of the Hall conductance". In: *Annals of Physics* 160.2 (1985), pp. 343–354. ISSN: 0003-4916. DOI: http://dx.doi.org/10.1016/0003-4916(85)90148-4.

[6] F. D. M. Haldane. "Model for a Quantum Hall Effect without Landau Levels: Condensed-Matter Realization of the "Parity Anomaly"". In: *Phys. Rev. Lett.* 61 (18 Oct. 1988), pp. 2015–2018. DOI: 10.1103/PhysRevLett.61.2015.

[7] Kane C. and Mele E. "Z_2 Topological Order and the Quantum Spin Hall Effect". In: *Phys. Rev. Lett.* 95.146802 (2005).

[8] Bernevig B., Hughes T., and Zhang S.-C. "Quantum Spin Hall Effect and Topological Phase Transition in HgTe Quantum Wells". In: *Science* 314 (2006), pp. 1757–1761.

[9] Markus König et al. "Quantum Spin Hall Insulator State in HgTe Quantum Wells". In: *Science* 318.5851 (2007), pp. 766–770. ISSN: 0036-8075. DOI: 10.1126/science.1148047.

[10] Fu L., Kane C., and Mele E. "Topological Insulators in Three Dimensions". In: *Phys. Rev. Lett.* 98.106803 (2007).

[11] Fu L. and Kane C. "Topological insulators with inversion symmetry". In: *Phys. Rev. B* 76.045302 (2007).

[12] Y. L. Chen et al. "Experimental Realization of a Three-Dimensional Topological Insulator, Bi2Te3". In: *Science* 325.5937 (2009), pp. 178–181. ISSN: 0036-8075. DOI: 10.1126/science.1173034.

[13] Y. Xia et al. "Observation of a large-gap topological-insulator class with a single Dirac cone on the surface". In: *Nat Phys* 5.6 (2009), pp. 398–402. URL: http://dx.doi.org/10.1038/nphys1274.

[14] D. Hsieh et al. "A tunable topological insulator in the spin helical Dirac transport regime". In: *Nature* 460.7259 (2009), pp. 1101–1105. URL: http://dx.doi.org/10.1038/nature08234.

[15] T. Hanaguri et al. "Momentum-resolved Landau-level spectroscopy of Dirac surface state in Bi_2Se_3". In: *Phys. Rev. B* 82 (8 Aug. 2010), p. 081305. DOI: 10.1103/PhysRevB.82.081305.

[16] Haim Beidenkopf et al. "Spatial fluctuations of helical Dirac fermions on the surface of topological insulators". In: *Nat Phys* 7.12 (2011), pp. 939–943. URL: http://dx.doi.org/10.1038/nphys2108.

[17] Yoshinori Okada et al. "Direct Observation of Broken Time-Reversal Symmetry on the Surface of a Magnetically Doped Topological Insulator". In: *Phys. Rev. Lett.* 106 (20 May 2011), p. 206805. DOI: 10.1103/PhysRevLett.106.206805.

[18] Peng Cheng et al. "Landau Quantization of Topological Surface States in Bi_2Se_3". In: *Phys. Rev. Lett.* 105 (7 Aug. 2010), p. 076801. DOI: 10.1103/PhysRevLett.105.076801.

[19] Zhang H. et al. "Topological insulators in Bi_2Se_3, Bi_2Te_3 and Sb_2Te_3 with a single Dirac cone on the surface". In: *Nat. Phys.* 5 (2009), pp. 438–442.

[20] D. Hsieh et al. "A topological Dirac insulator in a quantum spin Hall phase". In: *Nature* 452.7190 (2008), pp. 970–974.

[21] M. Z. Hasan and Kane C. L. "Colloquium: Topological insulators". In: *Rev. Mod. Phys.* 82.4 (2010), pp. 3045–3067.

[22] Yu R. et al. "Quantized Anomalous Hall Effect in Magnetic Topological Insulators". In: *Science* 329 (2010), pp. 61–64.

[23] Chang C.-Z. et al. "Experimental observation of the quantum anomalous Hall effect in a magnetic topological insulator". In: *Science* 340 (2013), pp. 167–170.

[24] Naoto Nagaosa et al. "Anomalous Hall effect". In: *Rev. Mod. Phys.* 82 (2 May 2010), pp. 1539–1592. DOI: 10.1103/RevModPhys.82.1539.

[25] Seongshik Oh. "The Complete Quantum Hall Trio". In: *Science* 340.6129 (2013), pp. 153–154. ISSN: 0036-8075. DOI: 10.1126/science.1237215.

[26] Jian-Min Zhang et al. "Stability, electronic, and magnetic properties of the magnetically doped topological insulators Bi_2Se_3, Bi_2Te_3, and Sb_2Te_3". In: *Phys. Rev. B* 88 (23 Dec. 2013), p. 235131. DOI: 10.1103/PhysRevB.88.235131.

[27] Y. S. Hor et al. "Development of ferromagnetism in the doped topological insulator $Bi_{2-x}Mn_xTe_3$". In: *Phys. Rev. B* 81 (19 May 2010), p. 195203. DOI: 10.1103/PhysRevB.81.195203.

[28] Yi-Jiunn Chien. "Transition Metal-Doped Sb_2Te_3 and Bi_2Te_3 Diluted Magnetic Semiconductors". PhD thesis. The University of Michigan, 2007.

[29] Cui-Zu Chang et al. "Thin Films of Magnetically Doped Topological Insulator with Carrier-Independent Long-Range Ferromagnetic Order". In: *Advanced Materials* 25.7 (2013), pp. 1065–1070. ISSN: 1521-4095. DOI: 10.1002/adma.201203493.

[30] M. Mogi et al. "Magnetic modulation doping in topological insulators toward higher-temperature quantum anomalous Hall effect". In: *Applied Physics Letters* 107.18 (2015), p. 182401. DOI: 10.1063/1.4935075.

[31] Inhee Lee et al. "Imaging Dirac-mass disorder from magnetic dopant atoms in the ferromagnetic topological insulator $Cr_x(Bi_{0.1}Sb_{0.9})_{2-x}Te_3$". In: *Proceedings of the National Academy of Sciences* 112.5 (2015), pp. 1316–1321. DOI: 10.1073/pnas.1424322112.

[32] Fang Yang et al. "Identifying Magnetic Anisotropy of the Topological Surface State of $Cr_{0.05}Sb_{1.95}Te_3$ with Spin-Polarized STM". In: *Phys. Rev. Lett.* 111 (17 Oct. 2013), p. 176802. DOI: 10.1103/PhysRevLett.111.176802.

[33] Herman M. A. and Sitter H. *Molecular Beam Epitaxy: Fundamentals and Current Status*. 1st ed. Vol. 7. Springer Series in Materials Science. Berlin Heidelberg: Springer-Verlag, 1989. ISBN: 978-3-642-97100-6.

[34] Hertz H. "Ueber die Verdunstung der Flüssigkeiten, insbesondere des Quecksilbers, im luftleeren Raume". In: *Ann. Phys.* 253.10 (1882), pp. 177–193.

[35] Knudsen M. "Die maximale Verdampfungsgeschwindigkeit des Quecksilbers". In: *Ann. Phys.* 352.13 (1915), pp. 697–708.

[36] Langmuir I. "Der Dampfdruck metallischen Wolframs". In: *Physik. Z.* 14 (1913), p. 1273.

[37] Knudsen M. "Experimentelle Bestimmung des Druckes gesättigter Quecksilberdämpfe bei 0 und höheren Temperaturen". In: *Ann. Phys.* 29 (1909), pp. 179–193.

[38] Martin Knudsen. "Das Cosinusgesetz in der kinetischen Gastheorie". In: *Annalen der Physik* 353.24 (1916), pp. 1113–1121. ISSN: 1521-3889. DOI: 10.1002/andp.19163532409.

[39] Chih-Shun Lu and Owen Lewis. "Investigation of film-thickness determination by oscillating quartz resonators with large mass load". In: *Journal of Applied Physics* 43.11 (1972), pp. 4385–4390. DOI: http://dx.doi.org/10.1063/1.1660931.

[40] *Sycon Instruments STM-100 User Manual*. English. Version Rev. G. Sycon Instruments. Sept. 1997.

[41] Venables J. A. *Introduction to Surface and Thin Film Processes*. 1st ed. New York: Cambridge University Press, 2000. ISBN: 978-0-521-78500-6.

[42] Liu W. et al. "High-quality ultra-flat $BiSbTe_3$ films grown by MBE". In: *J. Cryst. Growth* 410 (2015), pp. 23–29.

[43] Bauer E. "Phänomenologische Theorie der Kristallabscheidung an Oberflächen". In: *Zeitschrift für Kristallographie* 110.1-6 (1958), pp. 372–394.

[44] J A Venables, G D T Spiller, and M Hanbucken. "Nucleation and growth of thin films". In: *Reports on Progress in Physics* 47.4 (1984), p. 399.

[45] Bragg W. H. and Bragg W. L. “The Reflection of X-rays by Crystals”. In: *Proc. R. Soc. Lond. A* 88.605 (1913), pp. 428–438.

[46] W. Friedrich, P. Knipping, and M. Laue. “Interferenzerscheinungen bei Röntgenstrahlen”. In: *Annalen der Physik* 346.10 (1913), pp. 971–988. ISSN: 1521-3889. DOI: 10.1002/andp.19133461004.

[47] Ashcroft N. W. and Mermin N. D. *Solid State Physics*. 1st ed. Philadelphia: Saunders College, 1976. ISBN: 0030839939.

[48] T.C. Huang, R. Gilles, and G. Will. “Thin-film thickness and density determination from x-ray reflectivity data using a conventional power diffractometer”. In: *Thin Solid Films* 230.2 (1993), pp. 99–101. ISSN: 0040-6090. DOI: http://dx.doi.org/10.1016/0040-6090(93)90499-F.

[49] Joyce B. A. et al. “Analysis of reflection high-energy electron-diffraction data from reconstructed semiconductor surfaces”. In: *Phys. Rev. B* 29.2 (1984), pp. 814–819.

[50] J. Bardeen. “Tunneling from a many-particle point of view”. In: *Phys. Rev. Lett.* 6.2 (1961), pp. 57–59.

[51] J. Tersoff and D. R. Hamann. “Theory of the scanning tunneling microscope”. In: *Phys. Rev. B* 31.2 (1985), pp. 805–813.

[52] G. Doyen, D. Drakova, and M. Scheffler. “Green-function theory of scanning tunneling microscopy: Tunneling current and current density for clean metal surfaces”. In: *Phys. Rev. B* 47.15 (1993), pp. 9778–9790.

[53] R. J. Hamers, R. M. Tromp, and J.E. Demuth. “Surface Electronics Structure of Si(111)-(7x7) Resolved in Real Space”. In: *Phys. Rev. Lett.* 56.8 (1986), pp. 1972–1979.

[54] A. Mzerd et al. "Optimal crystal growth conditions of thin films of Bi_2Te_3 semiconductors". In: *Journal of Crystal Growth* 140.3–4 (1994), pp. 365–369. ISSN: 0022-0248. DOI: http://dx.doi.org/10.1016/0022-0248(94)90312-3.

[55] Yao-Yi Li et al. "Intrinsic Topological Insulator Bi_2Te_3 Thin Films on Si and Their Thickness Limit". In: *Advanced Materials* 22.36 (2010), pp. 4002–4007. ISSN: 1521-4095. DOI: 10.1002/adma.201000368.

[56] Xi Chen et al. "Molecular Beam Epitaxial Growth of Topological Insulators". In: *Advanced Materials* 23.9 (2011), pp. 1162–1165. ISSN: 1521-4095. DOI: 10.1002/adma.201003855.

[57] Guang Wang et al. "Topological Insulator Thin Films of Bi_2Te_3 with Controlled Electronic Structure". In: *Advanced Materials* 23.26 (2011), pp. 2929–2932. ISSN: 1521-4095. DOI: 10.1002/adma.201100678.

[58] Z. Aabdin et al. "Sb2Te3 and Bi2Te3 Thin Films Grownby Room-Temperature MBE". In: *Journal of Electronic Materials* 41.6 (2012), pp. 1493–1497. ISSN: 1543-186X. DOI: 10.1007/s11664-011-1870-z.

[59] S. E. Harrison et al. "Two-step growth of high quality Bi_2Te_3 thin films on Al_2O_3 (0001) by molecular beam epitaxy". In: *Applied Physics Letters* 102.17 (2013), p. 171906. DOI: 10.1063/1.4803717.

[60] Zhang J. et al. "Band Structure engineering in $(Bi_{1-x}Sb_x)_2Te_3$ ternary topological insulators". In: *Nat. Commun.* 2.574 (2011).

[61] He X. et al. "Highly tunable electron transport in epitaxial topological insulator $(Bi_{1-x}Sb_x)_2Te_3$ thin films". In: *Appl. Phys. Lett.* 101.123111 (2012).

[62] Liang He et al. "Evidence of the two surface states of $(Bi_{0.53}Sb_{0.47})_2Te_3$ films grown by van der Waals epitaxy". In: *Scientific Reports* 3 (2013), p. 3406.

[63] He X. et al. "Substitution-induced spin-splitted surface states in topological insulator $(Bi_{1-x}Sb_x)_2Te_3$". In: *Sci. Rep.* 5.8830 (2015).

[64] Iwata Y. et al. "In situ reflection high-energy electron diffraction (RHEED) observation of Bi_2Te_3/Sb_2Te_3 multilayer film growth". In: *J. Cryst. Growth* 203 (1999), pp. 125–130.

[65] Liu M. et al. "Electron interaction-driven insulating ground state in Bi_2Se_3 topological insulators in the two-dimensional limit". In: *Phys. Rev. B* 83.165440 (2011).

[66] Ahn J. and Rabalais J. W. "Composition and structure of the $Al_2O_3$0001-(1x1) surface". In: *Surf. Sci.* 388 (1997), pp. 121–131.

[67] Guénard P. et al. "Determination of the α-Al_2O_3(0001) Surface Relaxation and Termination by Measurements of Crystal Truncation Rods". In: *Surf. Rev. Lett.* 5.1 (1998), pp. 321–324.

[68] Walters C. F. et al. "The surface structure of α-Al_2O_3 determined by low-energy electron diffraction: aluminum termination and evidence for anomolously large thermal vibrations". In: *Surf. Sci.* 464 (2000), pp. 732–738.

[69] Liu Y. and Zhang J. "Effects of sapphire annealing on the structual properties of AlN thin films grown by molecular beam epitaxy". In: *Physica B* 405 (2010), pp. 1643–1646.

[70] N.N. Greenwood and A. Earnshaw. *Chemistry of the Elements*. 2nd ed. Oxford: Butterworth-Heinemann, 1997, pp. 1002–1039. ISBN: 978-0-7506-3365-9. DOI: http://dx.doi.org/10.1016/B978-0-7506-3365-9.50029-8.

[71] Kawasaki M. et al. "Atomic Control of the $SrTiO_3$ Crystal surface". In: *Science* 266 (1994), pp. 1540–1542.

[72] Biswas A. et al. “Universal Ti-rich termination of atomically flat $SrTiO_3$ (001),(110), and (111) surfaces”. In: *Appl. Phys. Lett.* 98.051904 (2011).

[73] Chang J., Park Y.-S., and Kim S.-K. “Atomically flat single-terminated $SrTiO_3$ (111) surface”. In: *Appl. Phys. Lett.* 92.152910 (2008).

[74] Connell J. G. et al. “Preparation of atomically flat $SrTiO_3$ surfaces using deionized-water leaching and thermal annealing procedure”. In: *Appl. Phys. Lett.* 101.251607 (2012).

[75] S. J. Sheather and M. C. Jones. “A reliable data-based bandwidth selection method for kernel density estimation”. In: *Journal of the Royal Statistical Society, Series B: Methodological* 53.3 (1991), pp. 683–690.

[76] Mao Ye et al. “Carrier-mediated ferromagnetism in the magnetic topological insulator Cr-doped (Sb,Bi)2Te3”. In: *Nature Communications* 6 (2015), pp. 8913–. URL: http://dx.doi.org/10.1038/ncomms9913.

[77] Joseph G. Checkelsky et al. “Dirac-fermion-mediated ferromagnetism in a topological insulator”. In: *Nat Phys* 8.10 (2012), pp. 729–733. URL: http://dx.doi.org/10.1038/nphys2388.

[78] Fu L. “Topological Crystalline Insulators”. In: *Phys. Rev. Lett.* 106.106802 (2011).

[79] Junwei Liu et al. “Spin-filtered edge states with an electrically tunable gap in a two-dimensional topological crystalline insulator”. In: *Nat Mater* 13.2 (2014), pp. 178–183. URL: http://dx.doi.org/10.1038/nmat3828.

[80] Andreas P. Schnyder et al. “Classification of topological insulators and superconductors in three spatial dimensions”. In: *Phys. Rev. B* 78 (19 Nov. 2008), p. 195125. DOI: 10.1103/PhysRevB.78.195125.

[81] Alexei Kitaev. "Periodic table for topological insulators and superconductors". In: *AIP Conference Proceedings* 1134.1 (2009), pp. 22–30. DOI: 10.1063/1.3149495.

[82] Hsieh T. H. et al. "Topological crystalline insulators in the SnTe material class". In: *Nat. Commun.* 3.982 (2012).

[83] Tanaka Y. et al. "Experimental realization of a topological crystalline insulators in SnTe". In: *Nat. Phys.* 8 (2012), pp. 800–803.

[84] Dziawa P. et al. "Topological crystalline insulator states in $Pb_{1-x}Sn_xSe$". In: *Nat. Mater.* 11 (2012), pp. 1023–1027.

[85] Xuetao Zhu et al. "Interaction of Phonons and Dirac Fermions on the Surface of Bi_2Se_3: A Strong Kohn Anomaly". In: *Phys. Rev. Lett.* 107 (18 Oct. 2011), p. 186102. DOI: 10.1103/PhysRevLett.107.186102.

[86] Shi J. et al. "Direct Extraction of the Eliashberg Function for Electron-Phonon Coupling: A Case Study of $Be(10\bar{1}0)$". In: *Phys. Rev. Lett.* 92.18 (2004), p. 186401.